Hot Nanoparticles

Jollans, T.G.W.

Citation

Jollans, T. G. W. (2020, January 30). *Hot Nanoparticles*. *Casimir PhD Series*. Retrieved from https://hdl.handle.net/1887/83484

Author: Jollans, T.G.W.
Title: Hot Nanoparticles
Issue Date: 2020-01-30

Hot Nanoparticles

Thomas Jollans

HOT NANOPARTICLES

Proefschrift

ter verkrijging van
de graad van Doctor aan de Universiteit Leiden
op gezag van Rector Magnificus prof. mr. C.J.J.M. Stolker,
volgens besluit van het College voor Promoties
te verdedigen op donderdag 30 januari 2020
klokke 10.00 uur

door

Thomas Georg William Jollans

geboren te Starnberg (Duitsland)
in 1990

Promotor:	Prof. dr. M.A.G.J. Orrit	*Universiteit Leiden*
Copromotor:	Dr. M. Caldarola	*Technische Universiteit Delft*
Promotiecommissie:	Dr. G. Baffou	*Université d'Aix–Marseille*
	Prof. dr. E.R. Eliel	*Universiteit Leiden*
	Prof. dr. M.P. van Exter	*Universiteit Leiden*
	Dr. D.J. Kraft	*Universiteit Leiden*
	Prof. dr. L. Kuipers	*Technische Universiteit Delft*

Casimir PhD Series, Leiden–Delft, 2020-01

ISBN 978-90-8593-428-8

An electronic version of this thesis is available at
`https://openaccess.leidenuniv.nl/`

Typeset by the author using LuaLaTeX, KOMA-Script and Libertinus fonts.
Cover art based on an untitled picture of sparks from a fire by fsHH (Pixabay).

Schematics of optical setups use components from *ComponentLibrary* by Alexander Franzen, which is licensed under a CC BY-NC 3.0 License. Most other figures were created using Matplotlib, the 2D graphics package for Python.

The work described in this thesis was carried out at the Leiden Institute of Physics (LION), Leiden University. It was supported by the NanoFront consortium, a program of the Netherlands Organization for Scientific Research (NWO) that is funded by the Dutch Ministry of Education, Culture and Science (OCW).

Für Oma

Contents

1 Introduction

In the mid-19th century, when the ether was still widely thought to exist, and years before James Clerk Maxwell's seminal paper on his theory of electromagnetism [1], Michael Faraday was performing experiments with very fine gold-leaf[1] in an effort to learn something about the nature of light and its interaction with objects of a size comparable to the wavelength. He discovered that, when a gold film on a glass plate is heated, it appears to vanish, and the surface of the glass acquires a reddish hue (very different from the green tint of the gold-leaf).

After establishing through chemical means that the gold, though invisible even under his microscope, was still present on the glass plate, Faraday postulated that the gold film had somehow run into separate particles so small as to be invisible, and that the distinctive red colour of the invisible gold was due to the small size of these particles. [2]

This suggestion would turn out to be remarkably prescient.

1.1 Gold nanoparticles

Today, we have no doubt of the existence of the gold nanoparticles Faraday postulated. A veritable zoo of nanoparticles of different materials and shapes can now readily be synthesized and studied either collectively or individually using optical methods (as we shall do in this thesis), and also examined using electron microscopy for detailed information about their structure. [3–6]

Nevertheless, the optical properties of nanoparticles of gold (or other metals, for that matter) are no less intriguing today than they were 162 years ago: the yellow colour of bulk gold is so distinctive and familiar that the entire field of heraldy refers to the colour yellow, when it appears on arms and flags, as 'gold', or, more properly, 'or' [7], and it is easily explained by reference to the band structure of atomic Au. The colour of gold nanoparticles (in solution,

---

[1] Today, we would presumably speak of a 'thin film'.

this is typically a shade of red, though it depends on the shape and size), on the other hand, evidences behaviour of gold at the nanoscale that is different both from the behaviour at macroscopic scales and at the atomic scale.

If ‘more is different’[2] is the unofficial motto of condensed matter physics, we might think along the same lines and use ‘smaller is different’ as a motto for nanoscale optics (and nanoscale physics more broadly). Just as (e.g.) the discrete translational symmetries in crystals and the breaking of these symmetries due to defects can produce incredibly rich physics in the macroscopic solid state, breaking material symmetries by introducing a surface at sub-wavelength scales can lead to equally rich optical properties that are not found at other scales.

This principle, that ‘very small’ objects — where, for the purposes of optics, ‘very small’ effectively means ‘sub-wavelength’ — are prone to show behaviour unknown at larger (bulk) or smaller (atomic) scales, applies not only to metal nanoparticles, but to a wide variety of structures, including molecules, nanotubes, dielectric nanoparticles, and semiconductor nanostructures (such as quantum dots). Gold nanoparticles, however, are the specific context of this thesis.

1.1.1 Optical properties of gold nanoparticles

Most of the optical properties of metal nanoparticles can be understood using a fully classical treatment, applying Maxwell’s equations to a plane wave incident on an object of the right nanoscale size and shape and the bulk (complex) permittivity $\varepsilon(\omega) = \varepsilon'(\omega) + i\varepsilon''(\omega)$ and calculating how light is scattered and absorbed by the object. In other words, most optical properties of a ~10 nm sphere would be reproduced by a ~1 m sphere investigated using shortwave radio, as long as it had the same permittivity in that frequency range (which a 1 m gold sphere certainly wouldn’t).

There are exact solutions to the problem for several simple geometries, of which the most relevant for this thesis are the sphere and the layered sphere. Collectively, these are generally (especially for spherical geometries) known as ‘Mie theory’, after Gustav Mie, who was one of a number of people, also

---

[2] The phrase ‘more is different’ refers to emergent behaviour that appears when many atoms (or molecules, birds, commuters, ...) interact, and is the title of an influential article by Philip W. Anderson [8], the later Nobel laureate who is credited with coining the term ‘condensed matter physics’ [9].

including Peter Debye and Ludvig Lorenz, who solved the problem of light scattering by a dielectric sphere around the turn of the 19th century [10–14]. To lowest order — i.e. in the electrostatic approximation, which is valid for small spheres with a radius $R \ll \lambda_0$ — the Mie result for a sphere (equivalent to Rayleigh scattering) can be written as

$$\sigma_{\text{sca}} = \frac{k^4}{6\pi}|\alpha|^2 \quad \text{and} \quad \sigma_{\text{abs}} = k\,\text{Im}(\alpha) \quad \text{where} \quad \alpha = 4\pi R^3 \frac{\varepsilon - \varepsilon_m}{\varepsilon + 2\varepsilon_m}, \qquad (1.1)$$

α being the polarizability volume, $k = 2\pi n_m/\lambda_0$ is the wavenumber in the surrounding medium, and ε_m is the permittivity of the medium surrounding the sphere. σ_{abs} and σ_{sca} are the absorption and (integrated) scattering cross sections, respectively [14].

The essential physics can already be extracted from eq. (1.1): Firstly, the sphere has a resonance at $\text{Re}(\varepsilon + 2\varepsilon_m) = 0$. This is known as the plasmon resonance, and is the main way to address gold nanoparticles optically. (It is also responsible for the red colour Faraday observed.) Secondly, we can make note of the fact that the optical properties depend on size, wavenumber and the material's permittivity $\varepsilon(\omega)$, but also on the permittivity of the medium, ε_m. Thirdly, scattering and absorption have different dependences on size ($\sigma_{\text{sca}} \propto R^6$ and $\sigma_{\text{abs}} \propto R^3$); we should expect absorption to dominate in the limit $R \longrightarrow 0$, and scattering to dominate at some larger size. What this size is will of course depend on the permittivities. Fig. 1.1a shows that for the sizes used in this thesis (viz. 50 nm to 100 nm)[3] absorption and scattering are comparable, and use of the electrostatic approximation is not justified; fig. 1.1b shows illustrative calculated spectra for an 80 nm sphere, showing the plasmon resonance in the visible.

As we work with sizes for which scattering is significant, it is important to introduce a third quantity next to scattering and absorption: the *extinction* cross section is defined as $\sigma_{\text{ext}} = \sigma_{abs} + \sigma_{sca}$; it corresponds to the amount of light that is not transmitted through a sample. When scattering is negligible, e.g. for most molecules, the distinction between extinction and absorption is often neglected since, in that case, $\sigma_{\text{ext}} \simeq \sigma_{\text{abs}}$. We cannot make that approximation.

While the wavenumber k does feature in eq. (1.1), the optical properties of a nanoparticle cannot be understood without reference to the bulk permittivity;

---

[3] Without further qualification, the 'size' of a nanoparticle refers to its diameter, not its radius.

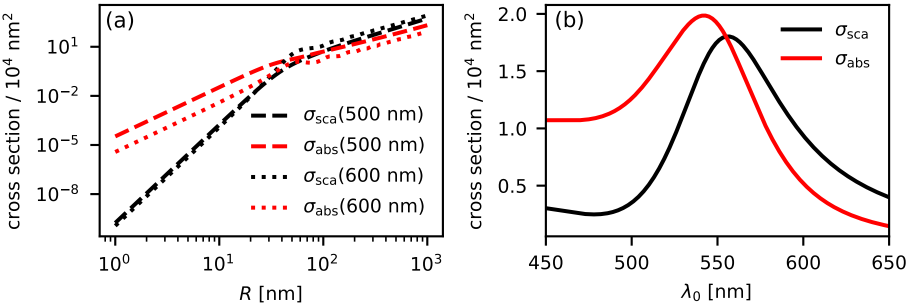

Figure 1.1: Mie theory calculations (using the implementation by Peña and Pal [15]) of the scattering and absorption cross sections of a gold sphere in a medium with $n_m = 1.33$ (e.g. water). **(a)** dependence of the cross sections on radius for two example wavelengths, which agrees with the approximation in eq. (1.1) for $R \lesssim 20\,\text{nm}$. **(b)** cross sections for $R = 40\,\text{nm}$ as a function of vacuum wavelength λ_0.

that of gold is reproduced in fig. 1.2. At low energies, it is well reproduced by a free electron (Drude–Sommerfeld) model; around and to the blue of ~500 nm, the permittivity is characterized by interband transitions in gold. These are responsible for the large absorption seen in this region in fig. 1.1b.

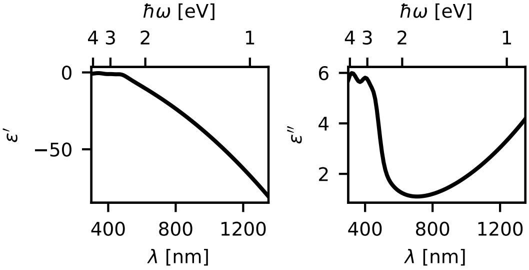

Figure 1.2: The permittivity $\varepsilon(\omega) = \varepsilon' + i\varepsilon''$ of gold as measured by Olmon et al. [16].

While the classical model can give us a good understanding of elastic scattering and absorption, it does not consider higher-order effects, some of which have proved to be extremely useful. Among the most important are near-field processes [17, 18], inelastic (Raman) scattering, and nanoparticle photoluminescence. The latter two go hand-in-hand and are introduced in some more detail in § 5.1.2.

1.1.2 Single gold nanoparticles

As discussed, the optical properties of gold nanoparticles are sensitive to the environment of the particles and, to a lesser extent, to their size. This has experimental implications: Gold nanoparticles, including the nanospheres used in the work presented in this thesis, are typically grown chemically. Whatever the method of production, there will be some random variation in the size of the particles, and thus of their optical properties. More importantly for our purposes, in a complex medium, the particles may see a variety of different environments depending on their location in space, or, in a dynamic environment, as a function of time.

Furthermore, the optical properties of gold nanoparticles are known to depend strongly on particle shape, and even the permittivity is not necessarily constant: ε depends, beyond the frequency, on the thermodynamic variables of state (temperature, density, etc.) [19, 20], on the crystal structure [21], and, for ~30 nm and smaller particles, even on the size [22].

These sources of inhomogeneous broadening, alongside the plain technical challenge, motivate the study of *single* nanoparticles and their optics: by monitoring a single nanoparticle optically, we get not only an unencumbered view of the properties of *that* particle, but also an indirect measure of the current environment of the particle — a sensor reading out properties of an attolitre volume, potentially in real time with nanosecond resolution (chapter 2), or, using pump-probe spectroscopy, with much higher time resolution (chapters 4 and 5).

This style of highly localized and very fast measurement lends itself to the study of dynamic processes at the nanoscale. A central theme of this thesis is applying this idea to heat transfer.

1.2 Hot nanoparticles

We have already established that gold nanoparticles absorb light. The absorbed energy, apart from the tiny fraction that is later reemitted as light, is dissipated as heat. For many purposes, this is a problem: a resonantly illuminated gold (or other metal) nanoparticle will heat up its surroundings, which may have unintended side-effects. Further, if the metal gets hot enough, it may melt, reshape (particularly if it was not spherical to begin with), and even fragment [23].

However, we can also make use of the fact that a gold nanoparticle becomes a nanoscale heat source which we, by varying the illumination, can control. As alluded to in the previous section, we can use it to study heat transfer at the nanoscale, or we could make use of the heat in one way or another [24].

Briefly, nanoparticles as nanoscale heat sources have found biomedical applications: biological tissue is sensitive to temperature, and localized hyper- or hypothermia has long been used for medical purposes — most crudely with contraptions like hot water bottles and ice packs. Localized hyperthermia is now being explored as a way to fight tumours, and metal nanoparticles have proven to be a promising way to introduce a highly localized heat source into the body. This idea is known as plasmonic photothermal therapy [25–28].

Beyond the temperature increase around a heated nanoparticle as such, we may also make use of secondary effects of the increased temperature: depending on the material properties of the medium, a change in temperature will lead to a change in density and, with it, to a change in refractive index. By illuminating a nanoparticle or an array of nanoparticles, then, we can exert influence on the temperature and refractive index distribution in space, and, to a certain extent, control it [29, 30]. If we control the refractive index distribution in a certain volume, we control the path light takes through that volume.

1.2.1 Photothermal microscopy[4]

If optically heating a particle changes the refractive index around it, and the optical properties of that same particle depend on the surrounding refractive index, then by illuminating an absorbing particle, we are changing its optical properties. While this nonlinear effect is naturally quite small, it has turned out to be very useful: To first approximation, the change in scattering due to optical heating $\partial\sigma_{\mathrm{sca}}/\partial P_{\mathrm{heat}}$ is proportional to the change in refractive index $\partial n/\partial P_{\mathrm{heat}}$, which, in turn, is proportional to the absorption cross section σ_{abs}, the change in refractive index with temperature $\partial n/\partial T$, and further thermal properties of the medium. [32–34]

Since the change in scattering depends only on a broadband refractive index change (typically referred to as a 'thermal lens'), we can apply a two-

---

[4] This section is partly based on the corresponding section in the publication: T. Jollans et al., 'Nonfluorescent Optical Probing of Single Molecules and Nanoparticles', J. Phys. Chem. C **123**, 14107–14117 (2019).

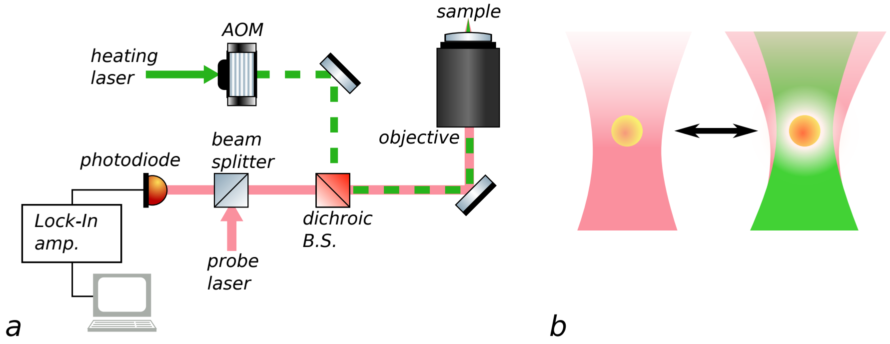

Figure 1.3: (a) simplified scheme of a photothermal microscope. (b) cartoon representation of thermal lens creation in a photothermal microscope's focus.

colour technique with a heating beam near the absorption resonance of the nanoabsorber and a probe beam of a different colour. The probe wavelength can then be judiciously chosen to lie far from the resonance in order to minimize damage and saturation due to the probe, thereby allowing for high probe intensities and accordingly low photon noise. [33]

What remains is extracting the *change* in scattering from the scattered light. To this end, the intensity of the heating beam is modulated at a certain frequency, generally in excess of 100 kHz, and the corresponding oscillating component of the scattered probe beam is extracted to recover the actual signal — generally with a lock-in amplifier. [32]

Fig. 1.3 shows a sketch of the technique, known as photothermal microscopy. For gold nanoparticles, we use a heating beam near the plasmon resonance (532 nm), and a probe beam far enough to the red that its absorption is negligible by comparison (815 nm in chapters 2 and 3, 785 nm in chapters 4 and 5). The heating beam intensity is modulated using an acousto-optic modulator (AOM).

Since the signal depends on the heating beam causing a temperature gradient, it is only sensitive to objects that absorb light of the chosen heating wavelength. The technique can therefore have extremely low background in a weakly-absorbing environment. With a suitable contrast agent, such as gold nanoparticles, it can be used in noisy biological environments [35, 36], and it can, under the right conditions, be used to detect even very weakly absorbing objects, down to single molecules [33, 37, 38].

Since the photothermal signal is dependent on the amount of energy absorbed by whatever is illuminated, we can, with a suitable calibration, use it to measure the absorption cross section of a single nano-object. Even without a calibration, we can discriminate different nano-objects based on their absorption; in particular, this technique is used in all the following chapters to identify single gold nanoparticles and distinguish them from clusters or aggregates of nanoparticles.

1.2.2 Plasmonic vapour nanobubbles

With a sufficient heating power, the liquid environment of a heated nanoparticle can reach temperatures of potentially hundreds of kelvin above the bulk boiling point while remaining in the liquid state [39]. Only as the medium is heated up so far as to cross the spinodal — the point, near the critical point, where the liquid phase ceases to be stable — does it decompose into a vapour bubble at the hot metal surface, and the remaining liquid phase further outside [40]. The vapour bubble expands rapidly outward before collapsing while the particle and its surroundings cool down.

This much, at least, theory and experiment have established for *pulsed* illumination, in which superheating of the medium is in any case confined to a short period of time, and in which a vapour nanobubble is, by the very nature of the excitation, a *transient* vapour nanobubble. Whether the spinodal picture applies under continuous-wave illumination, where transient vapour nanobubbles can form around a plasmonic nanoparticle and rapidly collapse despite the system having time to equilibrate [41], is as yet unclear.

Transient plasmonic vapour nanobubbles have been observed under both pulsed and continuous-wave illumination [41–44], and provide a fascinating test case for nanoscale heat transfer at nanosecond time scales [40, 45]. Chapter 2 explores transient and long-lived vapour nanobubbles in that context.

It has been suggested that bubble formation around heated nanoparticles is helpful in plasmonic photothermal therapy of cancer (see p. 6) [46–49]. This suggestion is primarily based on promising results published by Dmitri Lapotko, Ekaterina Lukianova-Hleb, and co-workers. However, the retraction and/or correction of several (but not all) of their papers on the subject [50–53] and the apparent subsequent departure of Lukianova-Hleb and Lapotko from academia cast considerable doubt on the idea.

1.3 Outline of this thesis

This thesis examines the processes surrounding laser-heated nanoparticles under a number of different conditions, and from a number of different angles. The following few paragraphs give a brief outline of its contents:

In **chapter 2**, we heat gold nanoparticles to the point at which vapour nanobubbles can form around them and beyond. We investigate how the dynamics vary with heating power and identify three distinct boiling régimes at the nanoscale: explosive boiling, semi-stable transition boiling, and nanoscale film boiling. We discuss how these relate to the well-known boiling régimes at macroscopic scales and draw parallels to the macroscopic boiling crisis. In the semi-stable transition régime, we observe remarkably stable nanobubble oscillations and discuss their properties in context.

Chapter 3 proposes an extension of photothermal microscopy to measure the chirality of or around single nanoparticles or nanostructures. After introducing chirality in general terms, we discuss the requirements on the symmetries of the experimental setup with reference to preliminary measurement results. We then apply the theory of tightly focussed beams to examine the consequences of different asymmetries for the experiment.

Chapter 4 uses pump-probe spectroscopy to probe the dynamics of already hot gold nanoparticles subjected to additional pulsed heating on picosecond-to-nanosecond timescales. The chapter looks in particular at heat transfer from the particle to its surroundings and discusses the idea of studying vapour nanobubble formation at a picosecond timescale.

Finally, in **chapter 5**, we turn our attention to the photoluminescence of hot gold nanoparticles. Anti-Stokes luminescence, in which photons extract energy from the thermal bath in the nanoparticle, is an indicator of the temperature within the nanoparticle. We use this to measure the electron temperature prevalent in a nanoparticle under pulsed laser illumination, which is of order 10^3 K. Using a two-colour pump-probe technique, we then measure how the temperature of a pulse-excited electron population in a single nanoparticle first grows and then decays within picoseconds.

2 Explosive, oscillatory and Leidenfrost boiling at the nanoscale

We investigate the different boiling régimes around a single continuously laser-heated 80 nm gold nanoparticle and draw parallels to the classical picture of boiling. Initially, nanoscale boiling takes the form of transient, inertia-driven, unsustainable boiling events characteristic of a nanoscale boiling crisis. At higher heating power, nanoscale boiling is continuous, with a vapour film being sustained during heating for at least up to 20 µs. Only at high heating powers does a substantial stable vapour nanobubble form. At intermediate heating powers, unstable boiling sometimes takes the form of remarkably stable nanobubble oscillations with frequencies between 40 MHz and 60 MHz; frequencies that are consistent with the relevant size scales according to the Rayleigh–Plesset model of bubble oscillation, though how applicable that model is to plasmonic vapour nanobubbles is not clear.

This chapter is based on the publication:
T. Jollans and M. Orrit, 'Explosive, oscillatory, and Leidenfrost boiling at the nanoscale', Phys. Rev. E **99**, 063110 (2019).

2.1 Introduction

The mechanisms involved in boiling of liquids in contact with a heat source are of crucial importance when it comes to understanding and optimizing heat transfer, particularly in applications requiring the removal of high heat flux. In recent years, there has been particular interest in the effect that the use of 'nanofluids' — fluids containing metal nanoparticles that may attach to device walls [55, 56] — and nanostructured surfaces have on pool-boiling heat transfer into the fluid [57]. There are many reports of both nanofluids and nanoscale surface roughness increasing the critical heat flux that a heating device can support. It is therefore imperative to gain a deeper understanding of boiling at the nanoscale, a topic we hope to shed some light on here.

In the canonical model of pool boiling, i.e. boiling of a large 'pool' of liquid through direct contact with a hot surface, boiling is thought to occur in three primary régimes: in order of increasing relative temperature ΔT — nucleate boiling, transition boiling, and film boiling (see fig. 2.1).

In nucleate boiling, boiling occurs at a myriad microscopic active vapour generating centres from which small bubbles rise upward (gravity is significant for common liquids at human size scales), and the resulting total heat flux from the heating surface to the liquid being boiled is proportional to the number of active vapour generating centres (bubble nucleation sites) at any given time. It is well-established that, apart from depending on ΔT, this number depends on the structure of the heater surface — broadly speaking, rougher surfaces support more vapour nucleation sites — but how a particular surface geometry will lead to particular boiling characteristics is not currently understood [58–60].

As the temperature and heat flux increase, an ever greater proportion of the surface will be covered by vapour bubbles. The vapour, with its much lower thermal conductivity as compared to the corresponding liquid, acts as a thermal insulator. This leads to the heat flux topping out at a *critical heat flux* and then falling as the temperature and the vapour coverage of the heater increase. This phenomenon is known as the *boiling crisis*. The boiling behaviour as the heat flux falls is characterized by large vapour bubbles forming at the heating surface and rising violently, and is referred to as *transition boiling* or *unstable film boiling* [57, 61–63].

If the temperatures are high enough to overcome the thermally insulating effect of a thin vapour film, boiling can stabilize into so-called *film boiling*. In

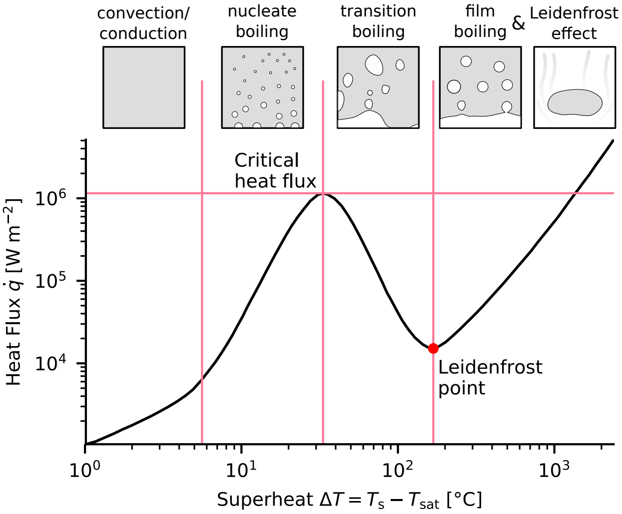

Figure 2.1: The well-known traditional boiling curve of macroscopic pools of water at atmospheric pressure with sketches of the different boiling régimes. Curve data adapted from Çengel [61].

the case of small drops of water coming into contact with a larger heating surface, this leads to drops levitating on a cushion of hot vapour. The heat flux again increases with temperature; the point of minimum heat flux is known as the *Leidenfrost point*, and the transition into film boiling is popularly known as the *Leidenfrost effect* — both named after Johann Gottlob Leidenfrost, who described the effect in 1756 [64].

While the precise thresholds and dynamics depend on various properties of the heater, from the material's thermal properties and surface microstructure up to the macroscopic shape [65], the broad outline of the behaviour as described above is widely applicable.

In this chapter, we dive down to the nanoscale using the tools provided by modern optical microscopy and study sub-microsecond boiling dynamics at a single artificial nucleation site in the form of a laser-heated gold nanoparticle (AuNP) — AuNPs are frequently used to optically generate vapour micro- and nanobubbles [40–45, 66–68]. We will find striking parallels to the progression of a macroscopic system through the boiling crisis, in which the entire heater surface dries out when a thermally insulating vapour film forms, and the heat flux plummets.

2.2 Method

This chapter follows on from our previously published results [41], in which we described an unstable, explosive nanoscale boiling régime arising under continuous heating, near the threshold heating power for boiling. Using mostly the same technique, here we investigate in detail the various dynamics arising from a much broader range of different heating powers, with an emphasis on exploring the parameter space beyond the threshold.

Gold nanospheres with a diameter of 80 nm (from NanoPartz™) are immobilized on a cover glass at very low surface coverage by spin-coating. The nanoparticles are submerged in a large reservoir of *n*-pentane and investigated optically in a photothermal–confocal microscope described in previous work [33, 41]: two continuous-wave laser beams, a heating beam and a probe beam, are carefully overlapped and tightly focused on the same nanoparticle. The heating beam is partly absorbed by the sample; the deposited energy and associated temperature increase lead to localized changes in the sample, e.g., in density. These changes affect how much the probe beam is scattered.

In photothermal microscopy, these small heating-induced changes can be used to measure a nano-object's absorption cross section [31]. In this work, we focus on the dynamics of the response, specifically in the case of boiling, instead.

n-Pentane was chosen as a medium, as in our previous work, due to its boiling point under ambient conditions (viz. ca. 36 °C) being close to room temperature; the intention of this choice was to reduce the necessary heating powers and the impact of heating-related damage to the AuNPs.

A single gold nanoparticle — identified through photothermal contrast — is heated using a focused near-resonant (532 nm, cf. fig. 2.2c) laser, the intensity of which is controlled using an acousto-optic modulator (AOM) and monitored using a fast photodiode. The nanoparticle is monitored in real time through the back-scattering of an off-resonant probe laser (815 nm), measured using another fast photodiode. Our real-time single-nanoparticle optical measurements allow us to non-invasively follow the dynamics of boiling and vapour nanobubble formation around the AuNP with a high time resolution, limited by the 80 MHz cut-off frequency (−3 dB) of our detector.

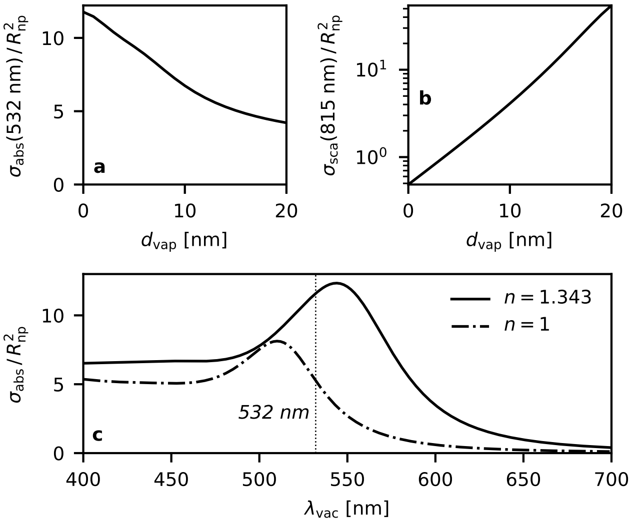

Figure 2.2: Layered-sphere Mie theory calculation [15] with an 80 nm diameter gold core and a vacuum shell (bubble, $n = 1$) of varying thickness d_{vap} in a medium with refractive index $n = 1.33$. **(a)** Absorption of $\lambda_{vac} = 532$ nm and **(b)** scattering of $\lambda_{vac} = 815$ nm, both shown as a function of bubble thickness. **(c)** Absorption spectra of 80 nm AuNPs, when in *n*-pentane as compared to vacuum. See also: appendix 2.A.

It is important to note at this point that a given heating laser intensity uniquely determines neither the absorbed heating power nor the temperature of the AuNP. Rather, the absorption cross section σ_{abs} of the AuNP, and with it the absorbed power, depends strongly on the environment: The localized surface plasmon resonance of the AuNP depends on the refractive index of the environment, i.e. on whether the AuNP is surrounded by liquid ($n \approx 1.33$) or vapour ($n \simeq 1$).

Modelling the nanoparticle surrounded by a vapour layer as a multi-layered sphere with a gold core and a shell with a refractive index of $n = 1$ and with a certain thickness d_{vap}, a layered-sphere Mie theory calculation [15] can give us an idea of how σ_{abs} changes upon nanobubble growth: figure 2.2a shows σ_{abs} dropping by 10 % with only a 3 nm thick bubble, and by half with 13 nm thickness. This leads to negative feedback as a vapour shell grows due to its optical properties. This complements the negative feedback due to the shell's thermal properties which is known from the classical Leidenfrost effect.

At the same time, the dependence of our read-out, the back-scattering at 815 nm, on the bubble size is not trivial. As fig. 2.2b shows, for sufficiently thin vapour nanobubbles, we can expect the scattering to grow steeply with the bubble thickness.

The AuNP is initially subjected to a heating laser intensity such that the system is near the boiling threshold, but below it; then, periodically, the AOM is switched to provide a pulse of some microseconds at a higher illumination intensity (duty cycle: 1 %).

The baseline intensity is chosen heuristically on a nanoparticle-by-nanoparticle basis by testing increasing baselines with a fixed additional on-pulse intensity until the measured scattering shows a significant change. The chosen baseline intensity is between 80 µW and 140 µW as measured in the back focal plane. The pulse length, pulse height, and baseline can then be changed at will between time-trace acquisitions; the length of a full time trace was 10 ms, of which the intensity is 'high' for 100 µs. Between subsequent acquisitions, a few seconds of dead time pass while data is stored and conditions are, as the case may be, changed.

2.3 Results

2.3.1 Nanoscale boiling régimes

Depending on the heating power during the heating pulse, boiling around the nanoparticles was observed to follow four distinct patterns as shown in figure 2.3, before irreversible damage sets in at higher powers:

I. — At sufficiently low power, the effect of heating the AuNP is limited to a small thermal lensing effect that cannot easily be directly identified from the time trace as shown. There is no indication of boiling.

II. — Above a certain threshold, ~ 120 µW in the back focal plane with some variation from particle to particle, as previously demonstrated [41], strong $\sim 1 \times 10^{-8}$ s spikes with similar peak values start appearing at random intervals. These can be explained by rapid inertially driven expansion of a vapour nanobubble around the AuNP; in the presence of this vapour shell, the hot AuNP experiences a boiling crisis and the nanobubble collapses immediately. While this behaviour is reminiscent of intermittent film boiling, averaged over

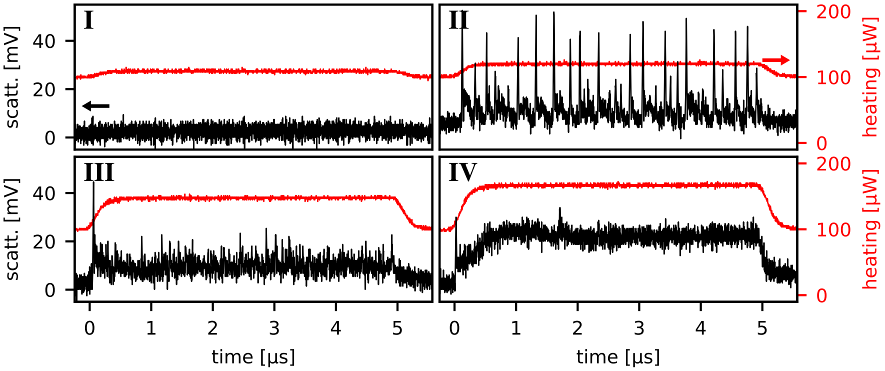

Figure 2.3: Single-shot scattering time traces of the same 80 nm Au sphere. Black: scattering in the detector's units (refer to the axis to the left); Red: heating intensity in the back focal plane (axis to the right). Four principal régimes of heated AuNP behaviour are observed: **I.** below boiling threshold; small thermal lensing effect. **II.** near boiling threshold; repeated short-lived vapour nanobubble formation. **III.** above boiling threshold; unstable vapour nanobubble for the duration of heating. **IV.** far above threshold; relatively stable nanobubble, probable damage to AuNP. See also: figure 2.4

many disperse vapour generating centres it should appear as nucleate boiling from a distance.

III. — As the power is increased further, beyond around 150 µW, all distinct explosive spikes but the first disappear. In their place, the initial explosion is followed by still highly dynamic behaviour, notably with a much smaller amplitude. It appears that while in the previous case, the AuNP returned to the same state after the boiling events (i.e. no vapour), now, it does not; after the initial expansion, the nanobubble does not appear to fully collapse, but rather to reduce to a sustainable if not particularly stable size. We can think of this as a transition boiling régime.

IV. — At extremely high powers, the signal steadily grows (as expected for a growing vapour bubble, cf. fig. 2.2b), after the initial spike, to a stable level that is maintained until heating ends. The signal overall appears calmer than in the previous cases. In analogy with the Leidenfrost effect known macroscopically, it appears that a nanometre-scale vapour film around the heated AuNP is only stabilized at these substantial heating powers.

Note that in the explosive régime (II), all events are clearly separated from one another, and all have approximately the same maximum value. In particular, no double-peaks have been observed. This indicates that each nanoparticle hosts only a single vapour generating centre.

In sustained boiling régimes (III, IV), nanobubble behaviour qualitatively stays the same from after the initial expansion until the heating intensity is reduced, for at least up to 20 µs: long-lived vapour nanobubbles do not appear to spontaneously collapse without a change in externally imposed conditions.

However, extended or repeated irradiation at powers sufficient for boiling will cause irreversible damage to the nanoparticle: in particular, after minutes of irradiation at high power, lower powers no longer show the familiar explosive nucleate boiling events. We cannot tell in what way the particles change during such long experiments. They might be melting, which could involve changing surface structure and/or contact area with the substrate, they might be fragmenting [69], or they may be sinking into the substrate [70]. Any one of these possibilities would change the optical and thermal properties in hard-to-predict ways.

Figure 2.4 shows how the behaviour varies with heating power; in particular, the explosive régime (II) clearly only occurs in a limited temperature range. Note also that the mean response does not have an equivalent to the nucleate boiling peak in the classical curve from figure 2.1.

2.3.2 Stable vapour nanobubble oscillations

For some nanoparticles, heating powers characterized by unstable boiling were found to produce not a randomly growing and collapsing vapour nanobubble, but a stable and surprisingly pure oscillation with frequencies around (50 ± 10) MHz (see figure 2.5a–d).

To crudely model the oscillations, we shall employ the Rayleigh–Plesset model [71] for spherical gas bubble oscillations, which has been shown theoretically to be remarkably effective for describing the kinetics of the initial expansion and collapse of a plasmonic vapour nanobubble [40, 45]:

$$\varrho R\ddot{R} + \frac{3}{2}\varrho\dot{R}^2 = p_\mathrm{g}\left(\frac{R_0}{R}\right)^{3\kappa} - p_\mathrm{a} - \frac{2}{R} - \frac{3\mu}{R}\dot{R}, \tag{2.1}$$

$$\text{with} \quad p_\mathrm{g} = \frac{2\gamma}{R_0} + p_\mathrm{a}, \tag{2.2}$$

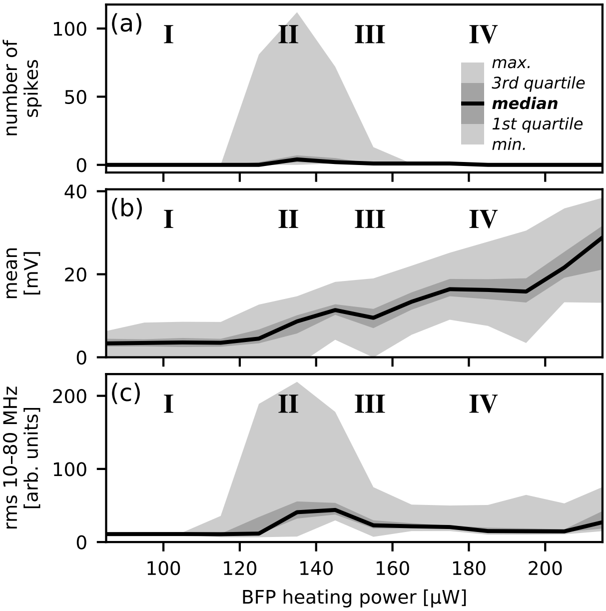

Figure 2.4: Dependence of vapour nanobubble behaviour on laser power, based on 8050 single-shot time traces measured at one nanoparticle, like those shown in figure 2.3. **(a)** number of spikes (extrema $\mathrm{d}\tilde{u}/\mathrm{d}t = 0$ where $\mathrm{d}^2\tilde{u}/\mathrm{d}t^2 < 0$ is below a heuristically chosen threshold, $\tilde{u}(t)$ being the signal smoothed with a 30 ns Hann filter) in the signal. **(b)** mean scattering signal during heating. **(c)** RMS power of the frequency components between 10 MHz and 80 MHz.

where R is the bubble radius, R_0 is the equilibrium radius, $\kappa = c_p/c_V$ is the polytropic exponent, γ is the surface tension, μ the dynamic viscosity, ϱ the liquid density, p_a the ambient (static) pressure, and p_g the gas bubble pressure at rest.

Compared to the full Rayleigh-Plesset equation as given by Lauterborn and Kurz [71], we are assuming no external ultrasound field and make no distinction between vapour and gas pressure. The latter approximation is an adiabatic approximation — it forbids mass transfer between the bubble and the liquid at the relevant timescales. If the bubble were to be understood classically as vapour, meaning vapour molecules can freely condense into the surrounding

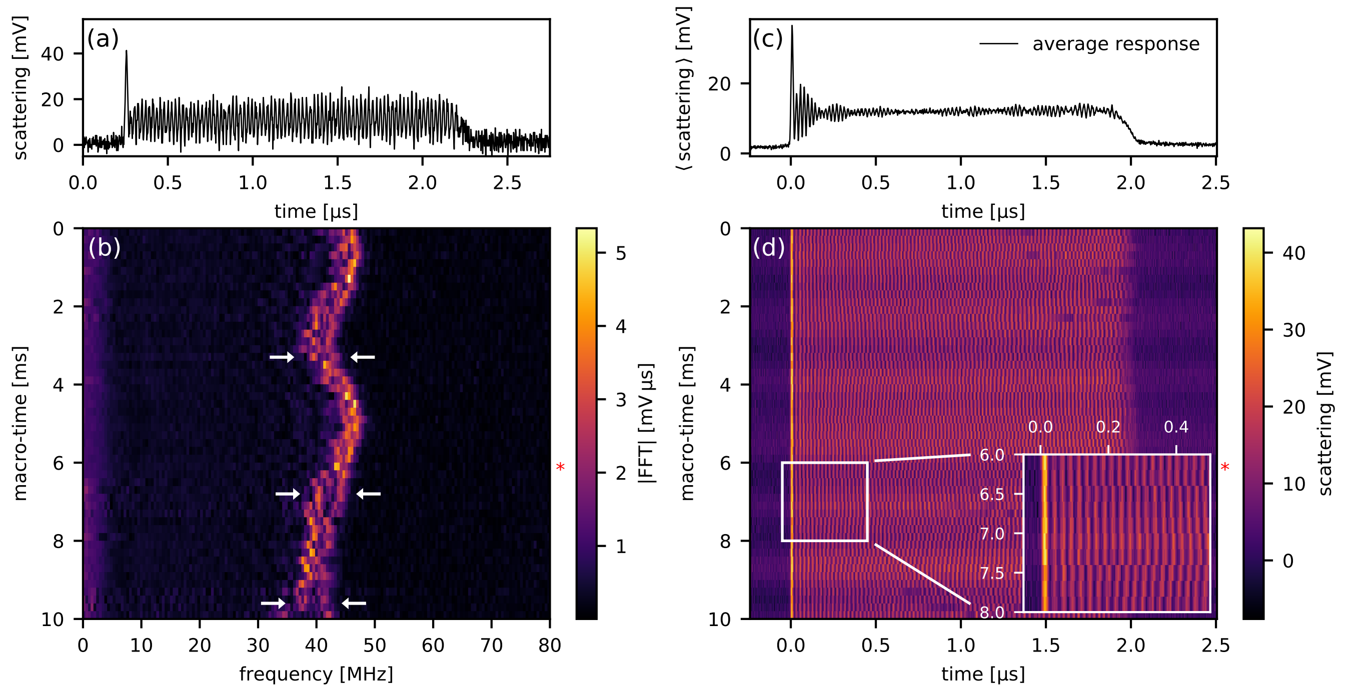

Figure 2.5: Nanobubble oscillations; **(a)** Single-shot nanobubble time trace with clearly visible oscillations. **(b)** Fourier transforms of 50 subsequent such time traces of the same AuNP subject to an unchanging heating profile. White arrows highlight some points with particularly clear frequency splitting. **(c)** Average of the time traces in (d), synchronized on the initial rising edge. **(d)** 50 time traces used in (b) *&* (c). In (b) and (d), the lines near the 6 ms mark indicated with ‘*’ correspond to (a).

liquid, then there would be no restorative force due to compression when the size of the bubble is reduced; there could be no oscillation. Oscillations are, however, clearly observed. Hence, we proceed assuming full conservation of mass for the material inside the bubble, i.e. we treat the vapour nanobubble as a classical gas bubble. (N.B., the applicability of the model is further discussed in appendix 2.B.)

Expanding eq. (2.1) for small perturbations $R = R_0(1+\varepsilon)$ from the equilibrium to first order in ε, we can reduce the Rayleigh–Plesset model to a damped harmonic oscillator,

$$\frac{\mathrm{d}^2\varepsilon}{\mathrm{d}t^2} + 2\zeta\omega_0\frac{\mathrm{d}\varepsilon}{\mathrm{d}t} + \omega_0^2\varepsilon = 0, \tag{2.3}$$

$$\text{where } \omega_0 = \frac{1}{R_0\sqrt{\varrho}}\sqrt{3\kappa p_\mathrm{a} + \frac{2\gamma}{R_0}\left(3\kappa - 1\right)} \tag{2.4}$$

$$\text{and } \zeta = \frac{3\mu}{2\varrho R_0^2\,\omega_0}. \tag{2.5}$$

This allows us to calculate the resonance frequency $f = \omega_0\sqrt{1-\zeta^2}/2\pi$, shown in fig. 2.6, using the well-known material properties of pentane [72] at the saturation point [73] at $p_\mathrm{a} = 1\,\mathrm{atm}$: $f = 40\,\mathrm{MHz}$ corresponds to $R_0 = 142\,\mathrm{nm}$. The influence of viscous damping has a negligible impact on the resonance frequency as $\zeta \sim 0.1$ is small; in the real system, damping seems to be counteracted by the driving force from heating, leading to stable self-oscillation.

We can take into account the temperature- and pressure-dependence of the density $\varrho(T, p_\mathrm{g})$ and surface tension $\gamma(T, p_\mathrm{g})$ by using the values for saturated liquid at $p_\mathrm{g} = p_\mathrm{a} + 2\gamma/R_0$ and the saturation temperature $T = T_\mathrm{sat}(p_\mathrm{g})$. If we do this, the results are only slightly changed: then, $f = 40\,\mathrm{MHz}$ corresponds to $R_0 = 136\,\mathrm{nm}$.

It's interesting to note that the two terms under the square root in eq. (2.4), $3\kappa p_\mathrm{a} = 0.33\,\mathrm{MPa}$ and $2\gamma(3\kappa-1)/136\,\mathrm{nm} = 0.36\,\mathrm{MPa}$, are of the same order of magnitude. The resulting frequencies, then, are not dramatically different from those predicted by the much simpler Minnaert model. In 1933, Marcel Minnaert proposed a simple model to explain the 'musical', i.e. audible, oscillations of spherical air bubbles in a stream of water (e.g. from a tap) [74], which does not consider surface tension or viscous drag, only the compressibility of the

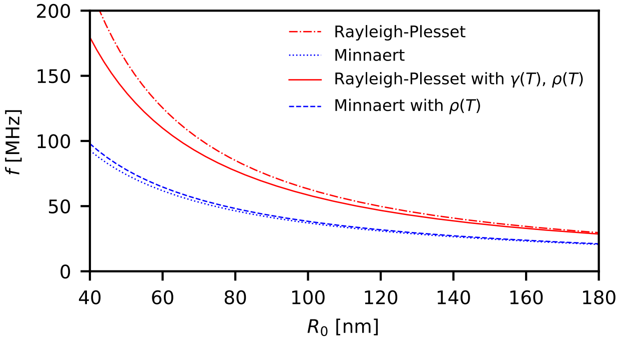

Figure 2.6: Resonance frequencies for vapour nanobubbles in pentane, according to the Rayleigh–Plesset and Minnaert models, with and without considering the temperature dependence of the surface tension γ and the density ϱ.

gas:

$$\omega_{\mathrm{Minnaert}} = \frac{1}{R_0}\sqrt{\frac{3\kappa p_{\mathrm{a}}}{\varrho}} \tag{2.6}$$

In any case, all oscillation frequencies observed correspond to radii larger than the radius of the AuNP (viz. $R_{\mathrm{np}} = 40\,\mathrm{nm}$), up to approximately the size of the near diffraction-limited focus of the heating laser (viz. FWHM $w_\perp = 0.2\,\mu\mathrm{m}$, $w_\parallel = 0.6\,\mu\mathrm{m}$). Direct measurement of bubble size is not possible with the present technique, but these estimates are in agreement with previous measurements of vapour nanobubble sizes [1].

The factors contributing to the oscillations are evidently not random: as fig. 2.5b–d show, the frequencies are strongly correlated from one event to the next; the resonance frequency appears to drift back and forth over time at audio frequencies, perhaps as a response to acoustic noise or small vibrations in the microscope. As the other examples in fig. 2.7 demonstrate, both the rate and periodicity of the frequency drift vary from measurement to measurement.

Additionally, as shown in figure 2.8, oscillation frequencies vary from particle to particle, as well as from moment to moment under constant experi-

---

[1] The curious reader is referred to section 11 of the Supplementary Information of Hou et al. [41].

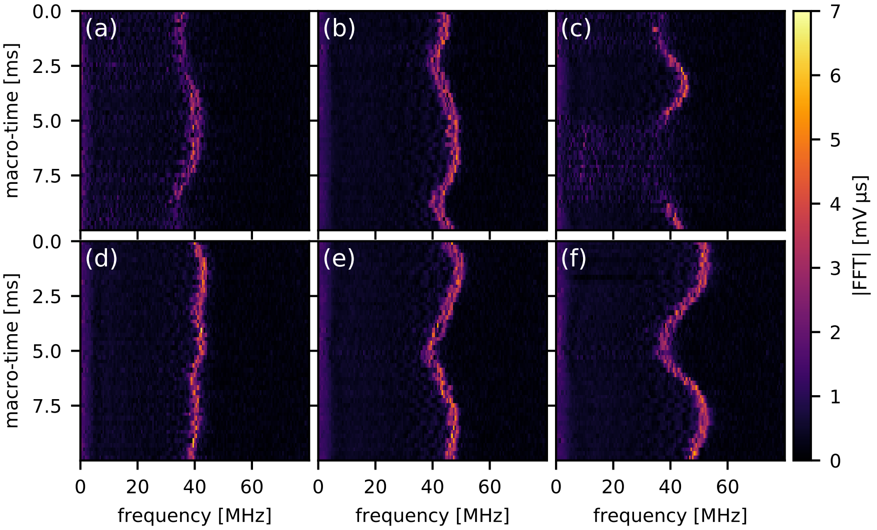

Figure 2.7: Example series of oscillating-bubble event Fourier transforms, all for the same nanoparticle, in the same form as fig. 2.5b.

mental conditions. For some, but not all, nanoparticles, the mean oscillation frequency appears to increase with heating power. However, as all the measurements were taken sequentially from low to high heating power, the changes in frequency may be due to ageing of the nanoparticle rather than due to any heating-dependent effect.

The Fourier transforms (fig. 2.5b) of many events show two frequencies split by a few MHz. In real space, this corresponds to a beat note which is visible faintly in a single time trace (e.g. fig. 2.5a) and visibly very clearly in the mean of a series of events, shown in fig. 2.5c. Note that the time traces in fig. 2.5c–d are synchronized on the initial rising edge of the response, not the heating pulse, in order to eliminate the possible effect of jitter in initial explosion. The fact that the mean in fig. 2.5c clearly shows the first few periods of the oscillation demonstrates that the oscillations are very consistently in phase from one event to the next.

The oscillations appear to only be stable between roughly 40 MHz and 60 MHz. From time to time (e.g. in fig. 2.7c), it looks like the resonance frequency drifts below 40 MHz and the oscillation collapses, before resuming later.

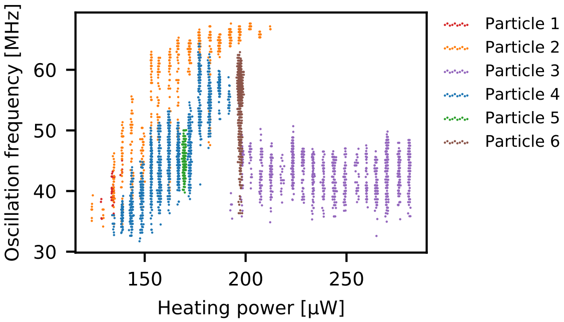

Figure 2.8: Change of the apparent oscillation frequency with heating power for different AuNPs. This figure shows the location of peaks in the Fast Fourier Transforms of individual time traces such as those shown in fig. 2.5b. Only measurements showing good oscillations are shown: those with $Q > 10$, where the quality factor $Q = f_{\text{max}}/\text{FWHM}$ is calculated from the FFT. 'Particle 4' refers to the set of measurements used in figures 2.5, 2.7 and 2.10.

Oscillations manifested themselves only around some of the AuNPs tested, but were remarkably robust against changes in power — leaving aside aforementioned heating-induced damage to the AuNP. In contemplating why these oscillations might only appear some of the time, we find ourselves confronted with the question of how the oscillations are possible at all: Existing models and reports of bubble oscillation [71], including at very small scales [68, 75], describe the oscillation of gas, rather than pure vapour bubbles.

Here, however, any sign of the bubble, or indeed its oscillation, disappear as soon as the heating ceases. This makes the notion of a permanent gas core in the oscillating bubbles seem unlikely. As a AuNP that supports oscillating vapour nanobubbles does so consistently — brief interruptions as seen in fig. 2.7c notwithstanding — we suspect that whether any particular AuNP supports these oscillations is linked to unknown structural or geometric properties, e.g. their exact volume, the size and structure of the facets on their surfaces, or the contact area with the glass slide.

2.4 Conclusion

By scaling down a heating element to the nanoscale, we have, simultaneously, scaled down the classical boiling régimes, from nucleate boiling to partial and full film boiling.

The nucleate boiling régime is stunted; rapid inertially driven expansion of insulating vapour bubbles leads the system into a boiling crisis, where the absorbed power is insufficient to drive continued boiling in the presence of the newly-formed vapour layer.

At higher incident powers, a boiling régime reminiscent of unstable film boiling can be sustained. Nanobubble oscillations *can* then be driven by the nanoheater, but for the most part, unstable boiling at the nanoscale is characterized by random fluctuations. When the laser intensity is sufficient for the AuNP to absorb and transduce a critical heat flux, even while surrounded by a thin vapour shell, vapour bubble formation stabilizes itself, leading to a nanoscale Leidenfrost effect.

Vapour nanobubble oscillations, when they occur, are remarkably consistent with the canonical model, the Rayleigh–Plesset equation, for oscillating gas bubbles of a similar size in the same environment. It would appear that, under certain conditions, vapour bubble dynamics are faster than vapour–liquid equilibration.

The transition from a highly unstable or explosive boiling régime to a stable one may have ramifications for potential applications of highly-heated nanoparticles. Mechanical stresses caused by bubble formation around gold nanoparticles, thought to be relevant in the context of plasmonic photothermal therapy [47–49], may well be greater in an unstable boiling scenario compared to a stable one. The intuitive maxim that more laser power leads to more damage may, under these circumstances, not apply — just as the relation between heat flux and temperature in macroscopic systems has long been known to be non-trivial.

Appendices

2.A Approximations: optics

The Mie–theoretical treatment of the optical properties of a multi-layered sphere is exact for perfect sphere in an isotropic environment, for an incident plane-wave field.

On the first point: The nanoparticle is very nearly spherical. A transient vapour nanobubble is *presumably* quite spherical in order to minimize surface area. However, the environment is not isotropic in our case; the AuNP is located on a glass surface (and illuminated from below, through the glass).

On the second point: the approximately Gaussian beams are tightly focused to near the Abbe diffraction limit. For the nanoparticle itself, the finite size of the beam is negligible. When a vapour bubble approaches the size of the focus, however, the finite size of the beam will have a greater impact, further complicating the optical problem.

The straightforward treatment of the cross sections σ_{abs}, σ_{sca} does not take into account possible (de)focusing of the beams by a nanobubble.

2.B Approximations: Rayleigh–Plesset model

The Rayleigh–Plesset equation assumes the spherical bubble is composed of an ideal gas and that there is no exchange of material between the bubble and the liquid (no evaporation, condensation, dissolution, mixing, etc.). Evaporation and condensation can be included by including a vapour pressure term in the static pressure.

By not including a vapour pressure term, we are requiring full conservation of mass in the bubble. Some degree of conservation of mass is required to give rise to a restorative force and hence oscillations, as indicated above.

Lauterborn and Kurz [71] include partial exchange of mass in their Rayleigh–Plesset equation by introducing a vapour pressure p_{v} that does not contribute to the pressure on the bubble wall. This is accomplished by replacing all occurrences of p_{a} in our equations (1) and (2) with $p_{\mathrm{a}} - p_{\mathrm{v}}$. This would, all said and done, reduce the effective ambient pressure, thereby lowering the resonance frequency for any given radius. In this light, the radii derived above might be understood as rough upper bounds.

Besides the possibility of a vapour bubble with partial conservation of (vapour) mass, one might consider a mixed vapour/gas bubble. In this case, the non-vapour gas would provide the restorative force generating the mechanical resonance. However, as we point out above, we do not believe this explanation is compatible with the fact that all signs of the bubble, including the oscillations, disappear when heating ends.

It further does not take into account damping through sound radiation, any temperature dependence, or deviation from spherical symmetry. No solid gold object in the centre is accounted for in the model, either. However, for a nanoparticle with $R_{\mathrm{np}} = 40\,\mathrm{nm}$ and a bubble with $R_{\mathrm{b}} \approx 120\,\mathrm{nm}$, the volume of the nanoparticle is less than 4 % of the bubble volume. The presence of the AuNP can therefore be neglected.

With regard to the question of why the vapour in the bubble is compressible *at all*, i.e. why vapour molecules do not appear to simply condense into the liquid when the bubble contracts, we can estimate the mean free path of a pentane molecule:

$$\ell = \frac{k_{\mathrm{B}} T}{\sqrt{2}\pi d^2 p},$$

where d is the molecular diameter and p is the pressure. Taking $d = 0.43\,\mathrm{nm}$ [76], $T = T_{\mathrm{sat}}$ and $p = p_{\mathrm{sat}} = 1\,\mathrm{atm} + 2\gamma/R$ (γ being the surface tension at saturation [73] and $R = 120\,\mathrm{nm}$ being the nanobubble radius), we get a mean free path of $\ell = 18.4\,\mathrm{nm}$.

This is smaller than the bubble thickness, meaning that the dynamics of the molecules deep in the vapour layer are not affected by the presence of the vapour–liquid interface and it is plausible that these molecules may contribute to a restorative pressure just as foreign gas molecules would. This reasoning is not valid, of course, for the outer quarter or so of the bubble.

More broadly, this mean free path gives us a Knudsen number of order $\mathrm{Kn} \sim 10^{-1}$, confirming that a continuum hydrodynamic model like the Rayleigh-Plesset model can be applied to the bubble. For further confirmation that the continuum approximation applies, we can estimate that in an $R = 100\,\mathrm{nm}$ sphere of a gas with $22.4\,\mathrm{L\,mol^{-1}}$, we expect some $\sim 10^5$ molecules.

More complex models can include more accurate equations of state (such as a van der Waals gas law), sound radiation, and other terms [71]. Lombard et al. [40] have described a detailed model of the heat transfer problem, but even that cannot account for the optical feedback expected in the case of

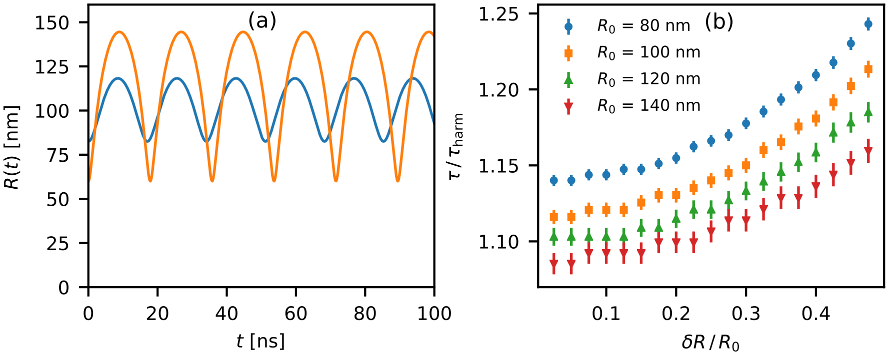

Figure 2.9: Anharmonicity of the Rayleigh–Plesset equation for a freely oscillating bubble, with the viscosity set to zero. Calculated by direct numerical (Runge–Kutta) integration with $\Delta t = 10\,\mathrm{ps}$ using the parameters for saturated pentane. **(a)** Example time traces of a bubble with $R_0 = 120\,\mathrm{nm}$ oscillating at two different amplitudes. The bottom of the curve, especially at larger amplitude, is noticeably more ‘pointed’, and the oscillation period is clearly different. **(b)** Calculated oscillation periods τ with different equilibrium radii R_0 and oscillation amplitudes δR, relative to the corresponding period τ_{harm} in the harmonic approximation.

continuous-wave heating, touched upon in § 2.2.

Further, our harmonic approximation drops all higher-order terms. The full equation predicts some anharmonicity at larger deviations, as shown in fig. 2.9. The error in the oscillation frequency predicted using the harmonic approximation at larger amplitudes is presumably small compared to the unclear effect of the driving force (due to heating) and of condensation and evaporation.

A slight anharmonicity is visible in the measured oscillations: in the series of Fourier transforms shown in fig. 2.10, for example, the second harmonic of the oscillation is just discernible when the Fourier transform is smoothed, or in the mean of all acquisitions. This measurement is also affected by the nonlinearity inherent in the measurement itself, as shown in fig. 2.2b.

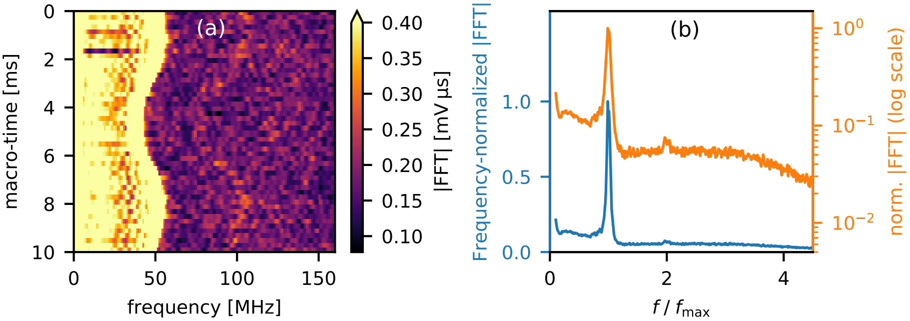

Figure 2.10: **(a)** Series of oscillating-bubble event Fourier transforms (same data as fig. 2.7f, smoothed with a 6 MHz Hann filter) showing, faintly, the second harmonic. **(b)** Mean of the Fourier transforms shown, calculated after rescaling the frequency axis of each to put the maximum at unity, showing clearly the second harmonic.
Note that the upper cut-off frequency of our detector is 80 MHz, which reduces the apparent prominence of the second harmonic, and completely obscures higher harmonics.

3 Photothermal detection of (quasi-)chirality

We propose using photothermal microscopy to measure the differential absorption of left- and right-handed circularly polarized light by a single nanoparticle or nanostructure, and with it, chirality of the nano-object and its environment. Care must be taken to distinguish true chirality from quasi-chirality of low symmetry but achiral structures which has similar effects. For the measurement to be reliable, the symmetry of the experimental apparatus must be carefully considered; we discuss the rôle of symmetry in the measurement in general, and specifically in the context of a tightly focussed beam. We find that slight asymmetries due to shifted laser beams or elliptical polarisation states can quickly lead to crippling aberrations and show how and why wide-field illumination is a viable remedy.

Foreword

This chapter focusses on the development of an experimental technique which came with numerous unforeseen challenges. While this is true of most techniques in their early stages of development, the surprises in this work are fairly interesting in their own right and deserve to be examined (though they, to the chagrin of everyone involved, shall not be conclusively explained). The focus on the development process and its follies demands an unconventional structure, which I beg the reader to indulge.

3.1 Background

Chirality[1] is a geometric quality of many molecules and other objects, including hands of primates, by which the mirror image of the body cannot be transformed back into the original body by rotation and translation alone. A chiral object and its mirror image are known as *enantiomers*[2] of each other.

In the realm of (Bio-)Chemistry, chirality is a particularly fascinating topic: Most naturally occurring chiral molecules occur almost exclusively in one of the two possible forms. While in isolation or in a mirror-symmetric environment, two enantiomers would behave identically, as soon as e.g. some other molecule breaks that symmetry, one handedness will react differently from the other. As all sugars and all amino acids save glycine — and thus most target receptors on proteins — are chiral, there is often a strong preference for a molecule to have one handedness rather than the other. A few molecules, such as carvone, do occur naturally in both left- and right-handed forms. Many drugs are synthesized with two enantiomers, only one of which is safe and effective. [77]

The chirality of molecules is generally measured through its optical effect on polarized light; either by measuring the optical rotation — the degree by which the axis of linear polarization of incident light is rotated — or by measuring circular dichroism (CD) — the differential absorption of the two handednesses of *circularly* polarized light [77]. CD in particular has been shown to be an effective tool for analysing secondary structure of proteins, including information about the conformational behaviour of the molecules. [77–79]

---

[1] handedness, from Greek χείρ (*hand*)

[2] from Greek ἐναντίος (*opposite*) — cf. English *anti-*

While these techniques are well-established and widely used, they require relatively large quantities of a relatively enantiopure substance to be useful. Consequently, new techniques for detecting and discriminating minute quantities of chiral molecules may prove very useful.

In recent years there has been much interest in emulating and enhancing this optical activity using chiral plasmonic nanostructures [80–82]. Some researchers have attempted to use chiral plasmonics to discriminate molecular enantiomers from one another [82]: it is a well-established fact that chiral molecules are selected for by other chiral molecules — can chiral plasmonic nanostructures do the same? Govorov has suggested [83] that achiral plasmonic nanoparticles can couple to chiral molecules and enhance the CD of the system. Maoz *et al.* [84] have reported promising measurements of the CD of riboflavin coupling to achiral nanometer-sized gold islands, in good agreement with Govorov's theoretical model, albeit without demonstrating an ability to distinguish enantiomers from one another. The effectiveness of this technique as a sensor of molecular handedness is therefore still in doubt.

In the following, we will present progress towards detecting chirality at the single nano-absorber level using a modified phothermal microscopy technique. We hope this technique will eventually mature to the point of detecting chiral molecules through their coupling to achiral plasmonic nanoparticles.

3.2 Chirality in optics experiments

Both optical phenomena which are used to detect chirality of molecules, circular birefringence (CB) — which gives rise to optical rotation — and circular dichroism (CD), rely on a difference in which left- and right-handed circularly polarized light interacts with a sample. Circular birefringence takes the form of a difference in the real part of the (complex) refractive index, while circular dichroism is a difference in the imaginary part of the same for the two circular polarizations.[3] For now, let's think of both as examples of left–right circular dissymmetry.

For left–right circular dissymmetry, in the most general sense, to occur in a optical measurement, i.e. for left- and right-handed circularly polarized light

---

[3] Just like the real and imaginary parts of n, CB + iCD are best understood together, and are related through Kramers-Kronig relations. To paraphrase singer Frank Sinatra, they go together like a horse and carriage: 'you can't have one without the other!'

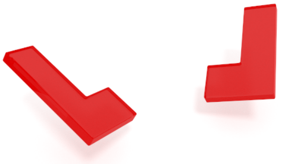

Figure 3.1: A ‘2D chiral’ structure and its mirror image in 3D space. In the plane, the shape lacked mirror symmetry, in 3D space it does not.

to give different results in any given experiment, something in the experiment must break mirror symmetry: If the experiment using left-polarized light can be transformed into the experiment using right-polarized light using symmetry transformations which must include an odd number of inversions or reflections (to move from right- to left-handed polarization), then there cannot be any left–right circular dissymmetry since the two experiments would be indistinguishable.

For this test we must in principle consider the *entire* experiment, from the point at which the polarisation states are prepared, through the sample, to the point where the polarization ceases to differ, which may be a photodetector, or which may be a polariser. If the experiment as a whole has mirror symmetry, left–right circular dissymmetry cannot occur; if the experiment as a whole lacks mirror symmetry, i.e. if it is chiral, then left–right circular dissymmetry is possible (but not necessarily present).

The most straightforward scheme for detecting circular dichroism operates, in broad strokes, as follows: a (tunable) light source, a switchable circular polariser (typically a photo-elastic modulator), a cuvette containing the sample and a photodiode are arranged in a straight line, the optical axis. The sample is typically in liquid form, and the molecules in it sample all orientations (we’ll come back to this later). The walls of the cuvette are generally flat and parallel. In this scenario, if the molecules in the sample are achiral, then entire experiment is, and vice versa.

3.2.1 Quasi-chirality

At this point, we should consider what a ‘chiral sample’ looks like. To the chemist, chirality is primarily a characteristic of asymmetric carbon centres in molecules, which do away with mirror symmetry. The mathematician knows that chirality depends on the dimensionality of the space: while it can be defined in any space in which reflections are defined, in Euclidean space, an object that is chiral in nD (e.g. 2D) will no longer be chiral when it is brought into $(n + 1)$D (e.g. 3D) space, as illustrated in fig. 3.1.

This creates a class of structures we can call ‘2D Chiral’: they include all structures which, in the plane, are chiral, but when lifted out of the plane, gain a mirror symmetry plane in 3D space — the plane they lie on. These structures are not chiral in 3D space, and do not exhibit any CD or CB. However, in many experiments, they appear to do so:

Firstly, in practise, a 2D chiral structure at the scale of optical wavelengths will be printed or etched onto or into one side of some kind of substrate. The presence of the substrate itself already breaks mirror symmetry; while the structure on its own may be achiral, a 2D chiral structure becomes truly chiral, in 3D, as soon as it is put on a substrate, or, more broadly, as soon as it acquires a sense of ‘up’ and ‘down’, perpendicular to its plane. For typical nanofabrication methods, this sense of ‘up’ and ‘down’ is reinforced by rounded corners and slanted edges away from the substrate [85].

Secondly, the way the experiment is performed is crucial. If we consider our straightforward CD measurement approach from above, and instead of the cuvette containing some chemical, we insert a 2D chiral sample. This might be an array of gammadia[4], prepared in such a way as to prevent any significant substrate effects or other dissymmetries: a truly achiral (in 3D) sample. Let the array be mounted perpendicularly to the optical axis. You can convince yourself that this combination of the achiral experimental setup with an achiral (albeit ‘2D chiral’) sample, is in fact chiral when regarded as a whole [86].

This quasi-chiral behaviour arising from the experimental setup rather than from chirality of the sample itself depends on the experimental setup breaking the mirror symmetry of the sample, and the sample breaking the mirror symmetry of the setup. This is particularly easy for 2D chiral structures as they only have one mirror plane; we might therefore refer to all 3D structures which have exactly one mirror symmetry plane as ‘2D chiral’, even if they are not, in fact, two-dimensional. The behaviour is fundamentally different from CD/CB, and can be distinguished from them by complete analysis of the transmitted polarisation state [85, 87]; most strikingly, a 2D chiral structure, when inserted into the experiment the other way around, has the opposite quasi-chiral effect [86]. This is very much unlike the behaviour of truly chiral samples, whose behaviour is maintained when you flip them upside down:

---

[4] The Greek term for the cross gammadion (卍) appears to be preferred, in the Physics literature, to the more well-known Sanskrit term for the symbol.

chirality is independent of rotation.

Quasi-chirality like this cannot occur if the 2D chiral structures are free to rotate and sample all possible orientations (as molecules in liquid do). It is therefore a problem lodged firmly in the domain of nanostructures, and does not affect chemistry. Similar left–right circular dissymmetry can arise in a number of different ways, even with samples that are achiral in all dimensions. As we shall see, the way this can occur when using tightly focussed laser beams, rather than an approximate plane wave, can be rather subtle.

3.3 Photothermal detection of circular dichroism

3.3.1 Premise

Traditional photothermal micro-spectroscopy relies on the change in scattering of a nano-object in its surroundings due to a thermal lens around it, that is to say due to photothermal effects that arise when the nano-object is optically heated (see § 1.2.1).

As this thermal lensing effect is small for a single nano-object, a lock-in technique is used, in which heating is modulated at a particular frequency of choice. In this way the thermal lens, and the scattering change it creates, are rapidly switched on and off at the same frequency; using e.g. a lock-in amplifier, it is then straightforward to quantify the size of the photothermal effects from an optical scattering measurement.

With a suitable calibration, this photothermal measurement can give us the absolute absorption cross section of the nano-object.

If we want to measure CD, we are not interested in the absolute absorption cross section of the object. Rather, we are interested in the difference between the amount one circular polarization is absorbed relative to the amount the orthogonal circular polarization is absorbed. With just a small change in the measurement approach, this can be accessible using photothermal microscopy, too:

The traditional scheme, as a lock-in measurement, is, fundamentally, already a differential measurement. It measures the difference in the amount of heat emitted from the absorber into its surroundings, and thus the difference in the amount of energy absorbed, between two cases: the case of low (or zero) light intensity, and the case of high intensity. If, now, instead of preparing low-intensity and high-intensity optical fields around the nanoparticle, we prepare a left-handed circularly polarized state on the one hand, and a right-handed circularly polarized state on the other, the same differential measurement will yield the circular dichroism of the absorber: the difference in the amount of energy absorbed depending on the circular polarization.

Perform this measurement on a non-chiral object, i.e. one that has no CD, and the signal should vanish. A non-chiral object cannot distinguish between left- and right-handed circular polarization, and therefore, if placed alternately in left- and right-handed optical fields, cannot behave any differently.

3.3.2 Possible pitfalls

As outlined in § 3.2, we must consider the symmetry of the experiment as a whole in order for the measurement to work as intended. If something, anything, breaks mirror symmetry, then the signal in the left- and right-handed cases can be different. If the sample is chiral and breaks mirror symmetry, then this difference signal is exactly the CD signal we want. If something other than the sample breaks mirror symmetry, this would lead to a systematic error: any chirality in the measurement apparatus can and will contribute to the measurement. It is therefore essential to consider carefully any possible unwanted sources of chirality.

Furthermore, circular dichroism is generally a weak effect. It is much weaker than the absorption as a whole, but it is also often weaker than linear dichroism. Linear dichroism is a difference in absorption between two linear polarizations of light, and is present in most anisotropic structures, provided they do not, through time or space averaging, sample all possible orientations during the measurement.

While the measurement appears simplest if the left- and right-handed fields used for probing CD are circularly polarized *perfectly*, this is not essential and there is no reason it shouldn’t work with elliptically polarized light, too. What *is* essential is that the change in handedness from left to right and vice versa is the *only* difference between the two. If the field strength (intensity) changes as well, the measurement will also be sensitive to absolute absorption. If the field is elliptically polarized and the major axis of polarization shifts in addition to the handedness, the measurement is also sensitive to linear dichroism.

The goal must be that the left- and right-handed test fields are equal and opposite (in terms of circular polarization) to the greatest extent possible. This is the core challenge of the experiment, seeing as any deviation, be it in intensity or orientation, will limit the sensitivity of the measurement.

3.4 Establishing a circularly polarized field

3.4.1 Principle

In order to modulate a circularly polarized laser beam from left-handed to right-handed, we chose to use an electro-optic modulator (EOM). An EOM uses the Pockels effect to introduce a phase shift $\varphi(u)$ along one of its characteristic axes in response to a voltage u. In a Jones matrix formalism, if the EOM is rotated by an angle of ξ, this can be represented as

$$\Phi_{\text{eom}} = \mathrm{R}_\xi{}^\dagger \begin{pmatrix} 1 & 0 \\ 0 & e^{i\varphi(u)} \end{pmatrix} \mathrm{R}_\xi, \tag{3.1}$$

where R_ξ is a rotation matrix of the usual form,

$$\mathrm{R}_\xi = \begin{pmatrix} \cos\xi & \sin\xi \\ -\sin\xi & \cos\xi \end{pmatrix}.$$

The most common use case for an EOM is to switch between two linear polarizations: If the EOM is aligned at $\xi = 45°$, and the incident polarization is horizontal,

$$\mathbf{E}_{\text{in}} = E_0 \begin{pmatrix} 1 \\ 0 \end{pmatrix} = \frac{E_0}{\sqrt{2}} \mathrm{R}_\xi{}^\dagger \begin{pmatrix} 1 \\ -1 \end{pmatrix},$$

then the polarization can be switched to vertical polarization

$$\mathbf{E}(\pi) = \frac{E_0}{\sqrt{2}} \mathrm{R}_\xi{}^\dagger \begin{pmatrix} 1 \\ 1 \end{pmatrix} = E_0 \begin{pmatrix} 0 \\ 1 \end{pmatrix}$$

by applying the half-wave voltage u_π where $\varphi(u_\pi) = \pi$. The EOM acts as a switchable half-wave plate.

Alternatively, in the same configuration, with an incident linear polarization at 45° to the EOM's characteristic axes, we can create circular polarization by switching between the quarter-wave voltages for $\varphi = \pm\pi/2$. In the Jones formalism, we would go from $\mathbf{E}_{\text{in}}$ to

$$\mathbf{E}\left(\mp\frac{\pi}{2}\right) = \frac{E_0}{\sqrt{2}} \mathrm{R}_\xi{}^\dagger \begin{pmatrix} 1 \\ \pm i \end{pmatrix} = \frac{E_0}{2} \begin{pmatrix} 1 \pm i \\ -1 \pm i \end{pmatrix} = \frac{E_0}{\sqrt{2}} e^{\pm i\pi/4} \begin{pmatrix} 1 \\ \pm i \end{pmatrix}.$$

While this would appear to be the ideal way to establish equal and opposite circularly polarized fields — by applying equal and opposite voltages to a crystal — a practical problem arises here due to the fact that the quarter-wave voltage is in excess of ±100 V, and the electronics we had access to are not capable of switching between different polarities of such high voltages.

Instead, the approach we chose was to switch the EOM between u_0 and u_π ($u_0 > 0\,\mathrm{V}$ being the bias voltage at which $\varphi(u_0) = 0$), which requires a $\lambda/4$ plate in addition to the EOM and a linear polarizer in order to establish the circular polarization states. We had a choice whether to send a linearly polarized state through the EOM and turn it into a circular one afterwards, or to prepare a circularly polarized state before the EOM and modulate that; we chose the former since this is the usual use case that the manufacturer of the EOM optimises for.

As a microscope objective is, ideally, cylindrically symmetric, we can prepare a circularly polarized state in the microscope focus by preparing a circularly polarized state directly before the objective. Placing the EOM and polarization optics directly below the objective in our commercial microscope body was, however, not feasible. Firstly, there is not enough space; secondly, in order to fill the objective and achieve a good focus we will in any case need some optics (specifically, lenses) between the EOM and the objective; and thirdly, because this would interfere with the detection. Our focus therefore soon became to minimize and, if necessary, compensate for, any opportunities the polarization state may have to change.

To minimize possible changes to polarization, we decided to keep the light path from the last polarizer, through the EOM, waveplates, other optical components and the objective to the sample, in one plane — for our inverted microscope, this was a vertical plane intersecting the optical table at a 90° angle. This polarization-sensitive part of the setup is sketched in fig. 3.2. Keeping it in one plane ensures mirror symmetry, and, as long as all optical components in the path are achiral, eliminates any possibility that chirality of the setup itself could influence the measurement. The polarization may still change due to reflections and the like, but as long as it does so in a mirror-symmetric way, the measurement is not affected.

We were particularly mindful of the fact that any deviation from the alignment plane, an imperfection in any component, or, above all, the unknown polarization behaviour of the dichroic mirrors, could change the polarization state. We therefore introduced, in addition to the $\lambda/4$ plate, a Berek variable

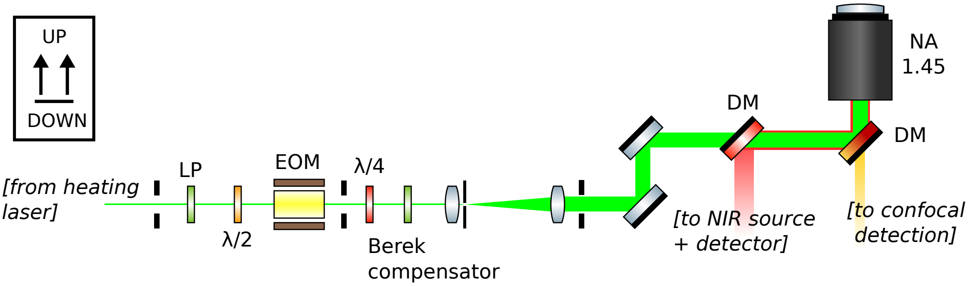

Figure 3.2: The polarization-sensitive part of the modified photothermal microscope. A linear polarization state is prepared ('LP': linear polarizer) and aligned to the correct axis (using a $\lambda/2$ plate) before the EOM, after which it passes a $\lambda/4$ plate to create circular polarization, a Berek compensator for fine-tuning, and a telescope with a spatial filter to eliminate asymmetries in the beam shape and expand the beam in order to fill the objective. 'DM': dichroic mirror.

waveplate in order to have full control over the final polarization state.

3.4.2 Verifying the polarization state

Measuring the polarization state at the microscope focus, while it may be possible, is not particularly practical. Our polarization measurements were instead performed by replacing the objective with a polarization detection apparatus in order to establish the polarization going into the objective. This is in principle equivalent to measuring the microscope focus itself if any birefringence or asymmetry in the objective is negligible, that is to say if the objective does not affect the polarization.

We used two *ad hoc* polarization detection apparatus: Firstly, a linear polarizer mounted in a motorized rotation stage, followed by a photodiode. This provides the major axis of (linear or elliptical) polarization, as well as the eccentricity. Secondly, a $\lambda/4$ plate, a polarizer and a photodiode, which provides the handedness of circular or elliptical polarization, as well as the degree of circular polarization.[5]

---

[5] Later, these apparatus were replaced by a newly acquired commercial polarization analyser from Schäfter + Kirchhoff. This may have enabled better control of the polarization, but did

Preliminary measurements of the behaviour of the EOM in isolation showed that, as expected, the phase introduced by the device (eq. (3.1)) is proportional to the voltage, and that for zero retardance, a bias voltage needs to be supplied. In other words, $\varphi(u) = \pi \cdot (u - u_0)/(u_\pi - u_0)$. They also revealed that, rather less expectedly, the values of u_0 and u_π depend somewhat on the precise alignment, on the modulation frequency, and on various other experimental parameters, some of which (such as the temperature) are rather hard to fully control.

After fixing the modulation frequency, then, there are three parameters that need to be adjusted to achieve the desired polarization states: the EOM voltages u_0 and u_π, and the retardance after the EOM, adjusted using the Berek compensator.

3.5 Preliminary results

3.5.1 Sample, setup, and expectations

Our primary test samples consisted of 80 nm gold nanospheres, spin-coated on glass at sufficiently low concentration as to ensure that only a single sphere will be in focus at a time. A single sphere on a flat substrate is obviously achiral, though individual nanoparticles may exhibit some random chirality due to their surface structure or immediate environment. The sample is mounted on a piezoelectric stage with which we locate nanoparticles and construct images pixel-by-pixel.

The samples are immersed in a liquid; either a chiral one (specifically: R- or S-carvone) or an achiral one (water, ethanol, or the racemic mixture[6] of carvone). As noted in § 3.1, the optical response of an achiral plasmonic nanoparticle should become chiral when it is surrounded by a chiral medium.

In an apples-to-apples comparison of the same, or even just a similar, nanoparticle, in dexter, sinister and racemic carvone, we would expect all three to have the same photothermal (absorption) contrast, and only the chiral samples to show any contrast when modulating polarization, as described in § 3.3.1. The signal for an achiral sample should be zero, and the signals for the two handednesses should be equal and opposite.

---

not affect the final result.

[6] A racemic mixture of a chiral molecule contains equal quantities of the left- and right-handed enantiomers. The term originates from *racemic acid*, an acid with this property found in grape juice. (lat. *racēmus*: bunch of grapes)

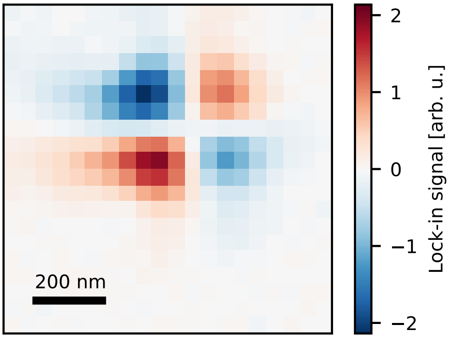

Figure 3.3: Example of a typical 'cloverleaf' image recorded using the chiral–photothermal approach with a tight focus. Single 80 nm gold nanosphere in a racemic mixture of R- and S-carvone. The peak magnitude of the pattern is approximately 10 % of the 'traditional' photothermal signal for the same particle.

We heat with a 532 nm beam, of which either the intensity — using an acousto-optic modulator — or the polarization — using an electro-optic modulator, as discussed above — is modulated at a frequency ~100 kHz. The beam is tightly focussed (NA = 1.4). We measure the back-scattering of an 815 nm laser beam using a fast photodiode which is connected to a lock-in amplifier (Stanford Research Systems model SR844). This beam is also tightly focussed using the same objective and carefully overlapped with the heating beam in order to maximize photothermal (absorption, not CD) contrast.

3.5.2 Cloverleaf

Figure 3.3 shows an example of the characteristic appearance of a gold nanosphere, in any medium, even an achiral one, using the tightly focussed polarization-switching measurement proposed in the previous sections. These cloverleaf patterns only appeared after extremely careful optimization of the laser foci of the heating and probe beams, the traditional photothermal signal (i.e. the overlap of the foci), and the polarization states before the objective.

The cloverleaf patterns have the same intensity to within margin of error for the different handednesses of carvone; the intensity varies for different media (e.g. ethanol instead of the carvone racemic). The orientation is the same for all nanoparticles surveyed, even in different samples on different days (rebuilding much of the setup would eventually change the orientation of the pattern).

This presented a bit of a puzzle. The pattern is not circularly symmetric, meaning something in the system was breaking the symmetry and introducing a distinction between different directions in the plane. As all particles show the same pattern with the same orientation, the origin of the asymmetry must be the setup, not the particles. The particles are randomly oriented on the surface. So where might the source of the asymmetry be?

3.5.3 Removing unwanted asymmetries, part 1

The *sample* appeared to be an obvious candidate. While the nanoparticles themselves can't be responsible, if the sample were tilted this would certainly break the symmetry in one way or another. As the direction of the pattern remained the same across different samples and different days, this appears to be excluded. Rotating the sample and replacing the sample holder also had no discernible effect.

Next, the *overlap* of the two beams. The beams are overlapped by maximizing photothermal contrast, and it is known that it is maximal when the heating and probe beams are focussed with a small axial offset. While this in and of itself would not break cylindrical symmetry, if the beams also had a lateral offset, this would. Shifting the probe beam with respect to the heating beam and sample should then, if the overlap were responsible for the pattern, rotate the pattern.

In fact, shifting the probe beam only moved which side of the pattern had the highest intensity; the direction and size were unaffected. It appeared the pattern is independent of the probe focus, and purely a property of the focussed heating beam.

Knowing that the pattern was due to a property of the heating beam or *focus*, we turned our attention to the position and direction the beam was entering the objective. If the beam enters the objective off axis or at an angle, this would of course break the symmetry of the system. To test this hypothesis, we deliberately shifted the incident beam in different directions to create a less symmetric focus. This, too, did not change the orientation of the pattern, it merely skewed it somewhat.

Every step this far made the assumption that the *objective* had no or negligible asymmetries that might affect the experiment. Was this not the case? To test whether the directionality of the pattern was due to some preferred direction of the objective, we rotated it, which had no effect. Our objective (an Olympus PLAPON 60XOTIRFM) is not advertised specifically to be polarization-maintaining. We were able to acquire a polarization maintaining objective from Nikon (CFI Plan Fluor 60XS Oil) to test with instead. Replacing the objective had, qualitatively, no effect — the cloverleaf pattern remained, and kept the same orientation.

At this point we are able to conclude that the pattern arises due to some non-obvious asymmetry in the heating beam before it reaches the objective. To understand better what this might be, it is helpful to look at the theory of tightly focussed beams.

3.6 The focus of an asymmetric beam

3.6.1 General theory

To calculate the focal field $\mathbf{E}(\mathbf{r})$ of an objective with focal length f, resulting from an arbitrary incident field $\mathbf{E}_{\mathrm{inc}}(\mathbf{r}_\infty)$, we follow the derivation given in the literature [88, 89]:

$$\mathbf{E}(\mathbf{r}) = \frac{ife^{-ikf}}{2\pi} \iint\limits_{k_\perp < k_{\max}} \frac{\mathrm{d}k_x \mathrm{d}k_y}{k_z} \mathbf{E}_\infty(\mathbf{k}) e^{i\mathbf{k}\cdot\mathbf{r}} \tag{3.2}$$

where $\mathbf{k}$ is the wave vector of the diffracted far field $\mathbf{E}_\infty$, and $k_\perp = \sqrt{k_x^2 + k_y^2}$ is its component perpendicular to the optical axis, $\hat{\mathbf{z}}$. The far field $\mathbf{E}_\infty(\mathbf{k})$ originates at a sphere at radius f, with all wave vectors perpendicular to the sphere's surface (as the full derivation [88, 89] shows). In spherical coordinates $(\hat{\mathbf{r}}, \hat{\boldsymbol{\theta}}, \hat{\boldsymbol{\phi}})$, this means that $\mathbf{k} = k\hat{\mathbf{r}}$. Each point $(x_\infty, y_\infty, \tilde{z})$ on the surface of the far-field sphere contributes a wave vector of

$$\mathbf{k}(x_\infty, y_\infty) = \frac{2\pi}{\lambda} \left(\frac{x_\infty}{f}\hat{\mathbf{x}} + \frac{y_\infty}{f}\hat{\mathbf{y}} + \frac{\tilde{z}}{f}\hat{\mathbf{z}} \right)$$

to the focus field, where $k = 2\pi/\lambda$ is the incident wave number, and $\tilde{z} = \sqrt{f^2 - \tilde{r}_{xy}^2}$ with $\tilde{r}_{xy}^2 = x_\infty^2 + y_\infty^2$. The maximum wave vector in the xy plane is then determined by the size of the aperture: $k_{\max} = k \sin\theta_{\max} = k\mathrm{NA}/n$, where NA is the numerical aperture of the objective.

The incident wave $\mathbf{E}_{\mathrm{inc}}(x_\infty, y_\infty)$ is projected onto the far-field sphere and refracted. *s*-Polarized field components $\mathbf{E}_{\mathrm{inc}} \cdot \mathbf{n}_\phi$ are transmitted as is, and *p*-polarized components $\mathbf{E}_{\mathrm{inc}} \cdot \mathbf{n}_\rho$ are refracted towards the origin:

$$\mathbf{E}_\infty(x_\infty, y_\infty) = \left(t^{\mathrm{s}}\left(\mathbf{E}_{\mathrm{inc}} \cdot \mathbf{n}_\phi\right)\mathbf{n}_\phi + t^{\mathrm{p}}\left(\mathbf{E}_{\mathrm{inc}} \cdot \mathbf{n}_\rho\right)\mathbf{n}_\theta\right)\sqrt{\frac{n_1}{n_2}\frac{\tilde{z}}{f}}, \tag{3.3}$$

$$\text{where } \mathbf{n}_\rho = \frac{1}{\tilde{r}_{xy}}\begin{pmatrix} x_\infty \\ y_\infty \\ 0 \end{pmatrix}, \ \mathbf{n}_\phi = \frac{1}{\tilde{r}_{xy}}\begin{pmatrix} y_\infty \\ x_\infty \\ 0 \end{pmatrix}, \text{ and } \mathbf{n}_\theta = \frac{1}{\tilde{r}_{xy} f}\begin{pmatrix} x_\infty \tilde{z} \\ y_\infty \tilde{z} \\ \tilde{r}_{xy}^2 \end{pmatrix}.$$

The coefficients t^{s} and t^{p} are the *E*-field transmission amplitudes for *s* and *p* polarization, respectively. We let both be equal to unity for the calculations. The refractive indices inside and after the lens can also be set to be equal, $n_1 = n_2$, for an oil immersion objective.

Most authors, at this point, simplify eq. (3.2) considerably using the symmetries of a typical Gaussian beam passing through the centre of the objective. As we're interested in focal asymmetries, we refrain from doing so, and instead calculate the focus field by direct numerical integration of eq. (3.2).

For the most part, the integration was performed using canonical adaptive quadrature routines [90, 91]. The calculations in § 3.6.3 instead used fast Fourier transforms in a 'fast focus field' approach [92], which relies on interpreting eq. (3.2) as a two-dimensional Fourier transform. The two approaches are equivalent, but come with different numerical stability concerns and different sources of numerical error. The latter, as the name suggests, is faster.

3.6.2 Calculations of asymmetric beams

In a straightforward proof of concept calculation, we compute the expected focus (specifically at $z = 0$) for an incident Gaussian beam with a waist of 3 mm, everywhere perfectly circularly polarized. Figure 3.4a–e shows the polarization components of the resulting focus. The in-plane linear polarization components (fig. 3.4a–b) have the expected elongated shape, consistent with the *mmm* (D_{2h}) symmetry of a linearly polarized plane wave, while the circular polarization components (fig. 3.4d–e) show a circular intensity distribution, as there is nothing in the problem to break cylindrical symmetry. Fig. 3.4f shows

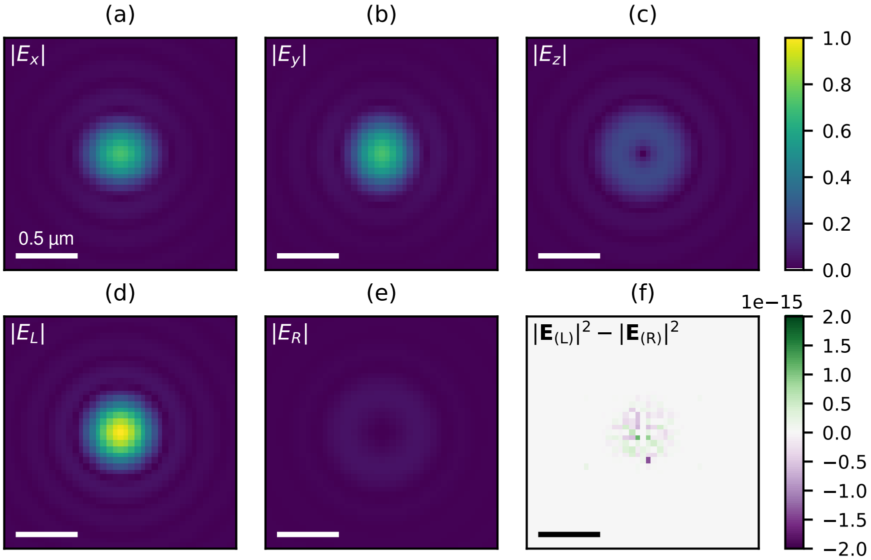

Figure 3.4: Tight focus calculation for a perfectly centred, perfectly circularly polarized Gaussian beam with a waist of 3 mm. **(a–e)** Magnitudes of the *E*-field components of different polarizations (incident: *L*), normalized such that $\max(|\mathbf{E}|^2) = 1$. Refer to upper colour bar. **(f)** Difference in intensity distribution between the foci of L- and R-polarized beams (numerical noise $\sim 10^{-15}$). Refer to lower colour bar.

the difference between the intensity distribution in the focus of a left-handed incident beam and that of a right-handed incident beam, which is equal to zero plus some numerical noise of order 10^{-15}. This is in line with the expectations as outlined in § 3.3.1.

We can now introduce changes, both chiral and achiral, to the problem compared to this ideal case in order to calculate an expected response.

One of the the simplest ways to reduce the symmetry of the system, which is initially cylindrically symmetric, is to shift the beam off-centre. This maintains a plane of mirror symmetry, so at first glance this does not appear to be chiral. And on the symmetry plane itself, it is not. However, if you consider an observer[7] located outside of the symmetry plane and measuring the electric

---

[7] In our system, the nanoparticle, heated by the heating beam and probed through scattering,

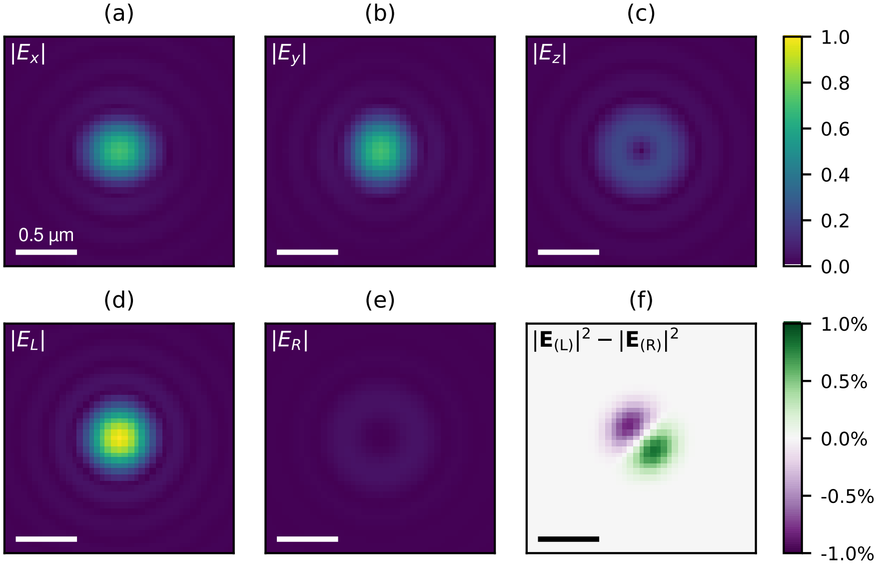

Figure 3.5: Tight-focus calculation for a perfectly circularly polarized Gaussian beam with a waist of 3 mm, centred at the point (100 µm, 100 µm), where (0, 0) is the centre of the objective. **(a–e)** Field components, cf. fig. 3.4. **(f)** Difference in intensity distribution between the foci of L- and R-polarized beams following the same path.

field there, the entire system (including the observer) breaks mirror symmetry. The calculation of the foci of left- and right-handed circular beam entering the objective off centre by (100 µm, 100 µm) predicts a characteristic two-lobe pattern to emerge in a differential measurement, shown in fig. 3.5f, with a magnitude of nearly 1 % of the peak intensity. The two-lobe pattern has a node along the one remaining symmetry plane of the system — the direction the beam is shifted in, (1, 1) — as along this plane, nothing breaks mirror symmetry.

As circular dichroism is a small effect at the best of times, it appears that even a ~100 µm misalignment could create a prohibitively large background signal.

Shifting the two incident beams relative to each other creates a similar two-lobe pattern, albeit with a different symmetry plane (see fig. 3.6). In

---

fulfils the rôle of the observer.

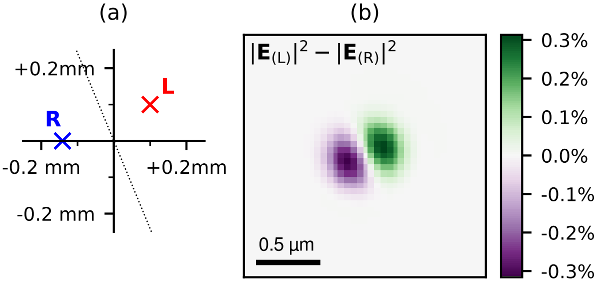

Figure 3.6: Difference in calculated foci for Gaussian beams entering the objective at two different offsets and with two different circular polarizations. **(a)** Locations of the centres of the beams in the back focal plane relative to the centre of the objective. The dotted line is the mirror plane through the origin which transforms one point to the other. NB the beam waist is 3 mm. **(b)** Difference in intensity distribution between the two.

order to create a quadrupole-like cloverleaf pattern like the one we actually measured (fig. 3.3), we need to introduce a different kind of asymmetry: one that also breaks cylindrical symmetry, but leaves intact the two mirror planes we see in the measurement. More formally, the perturbation(s) we apply must maintain a point group symmetry of $mm2$ (C_{2v}) or mmm (D_{2h}).

Linear polarization states have up to mmm symmetry: in a linear polarization basis aligned with the Cartesian coordinate axes, the vectors (x, y), $(-x, -y)$, $(x, -y)$ and $(-x, y)$ are all equivalent by symmetry. It's easy to imagine, even just from looking at the linear polarization components of a microscope focus as shown in fig. 3.4a–b, that an attempt to measure linear dichroism along the same lines as our proposed experiment would result in some kind of quadrupolar pattern, with two vertical (parallel to the optical axis) mirror planes.

It follows, then, that, if we are switching between two elliptical, rather than circular, polarization states and the major axes of these elliptical states were to differ by any amount, this would also produce a quadrupole pattern. Our measurements of the near-circular polarization states before the objective indicated eccentricities of $\varepsilon \approx 0.14$, corresponding to $\mathbf{E} \propto (1, \pm 0.99i)$, and a rotation of the major axis of polarization by almost 10°. To illustrate the effect of this, we can calculate the focal difference between two elliptical states, both

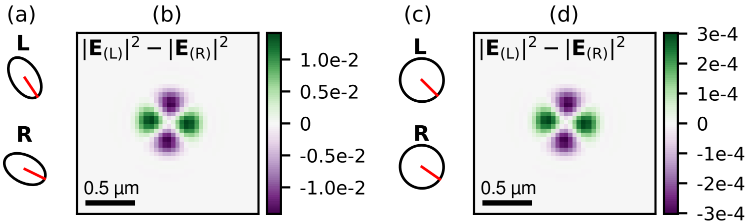

Figure 3.7: Difference in calculated foci for perfectly centred Gaussian beams with elliptical polarizations of opposite handedness. **(a)** Illustration of the polarization states used in (b); eccentricity $\varepsilon = 0.8$, rotated by ±30° relative to one another. **(b)** Difference in intensity distribution between the two. **(c, d)** Same as (a, b) with parameters closer to the measured polarisation states: $\varepsilon = 0.14$, ±10° shift.

with the same eccentricity, but with their major axis oriented differently.

Fig. 3.7 shows the resulting quadrupole pattern in this configuration. For this small eccentricity and shift in axis, it is a small change at less than 10^{-3}, but it might nonetheless be significant.

One could also imagine the incident beam's shape changing between the two states in a way that maintains *mm*2 symmetry, such as the beam being compressed along one axis in one of the circular polarization states relative to the other. It is not clear, however, how this kind of change would have arisen.

3.6.3 Wide-field

All these examples of small perturbations from the ideal perfectly symmetric system share one important property: the intensity is invariant at the origin. It's only as the nanoparticle, the observer in our system, is located sufficiently far from this central node (and thereby slightly out of focus), that the effects of such small asymmetries become visible.

When the particle is shifted off-centre slightly, it remains visible to our measurement since the focus of the probe beam is large enough to still see the signature of its thermal lens. This, however, we can change. While we cannot probe a smaller volume, we *can* increase the size of the heated area by moving towards wide-field illumination for the purposes of heating. With a less tight focus, we will move the edge effects of asymmetries further outward,

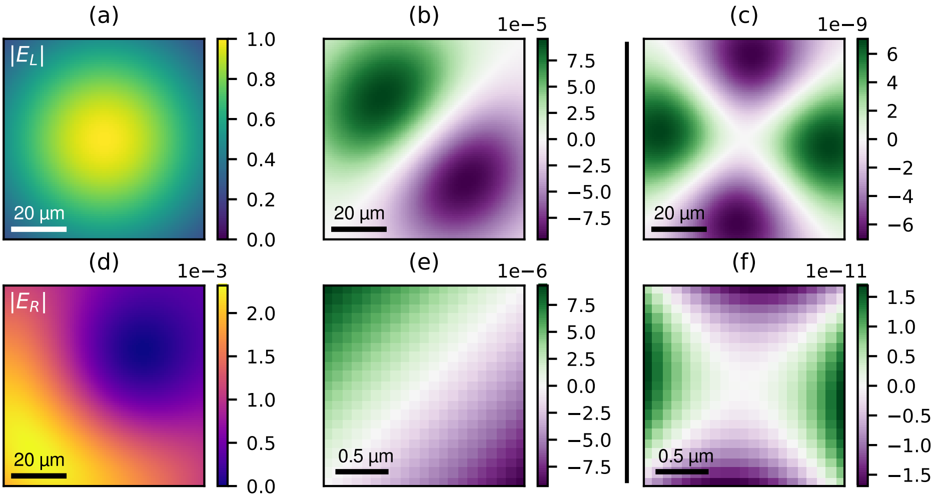

Figure 3.8: 'Wide-field' focus calculation: Gaussian beam with a waist of 10 µm focussed 2 cm before the idealized objective, resulting in a 56 µm beam in the focus. **(a, d)** Circular polarization components in the focus for a circularly L-polarized incident beam entering (100 µm, 100 µm) off centre. Note the E_R component is two orders of magnitude smaller than in the equivalent tight focus of fig. 3.5. **(b, e)** Difference in intensity for L and R-polarized incident off-axis beams (cf. fig. 3.5f). **(c, f)** Difference for elliptical beams like those in fig. 3.7. ['Fast Focus Field' calculation]

and create a larger 'clean' polarization state in the middle.

Fig. 3.8 shows calculated wide field foci in scenarios equivalent to the tight-focus scenarios presented in figs. 3.5 and 3.7. As the symmetry constraints of the system have not changed, the two- and four-lobe patterns are still present, but in the region of observation (i.e. within ~200 nm of the origin), their magnitudes have been reduced by four and almost nine orders or magnitude, respectively.

3.7 Removing unwanted asymmetries, part 2

If you recall, we had established that the heating beam had some asymmetric properties, which we would rather eliminate. In order to achieve this, the

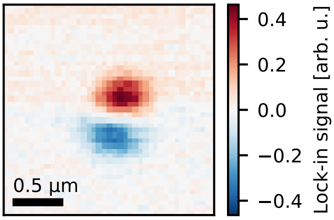

Figure 3.9: Example of a two-lobe image recorded using the chiral–photothermal approach with a tight focus. Single gold nanosphere in glycerol.

experimental setup, certainly the part illustrated in fig. 3.2, would have to be simplified, with any component that could be causing problems removed or replaced.

The dichroic mirrors were replaced with 50:50 beam splitters; perhaps less ideal for the experiment, as this entails losing 75 % of the signal even if the laser power in the sample is kept invariant, but simpler beam splitters are less likely to be the source of surprises. Qualitatively, this had no effect on the result: the cloverleaf pattern persisted.

Finally eliminating the periscope, and mounting the entire polarization-sensitive section of the experiment in one straight line, eliminated the cloverleaf pattern. By setting everything up in a straight line, we are moving close to cylindrical symmetry, rather than just the two-fold mirror symmetry needed to keep the setup as a whole achiral. However, while the obstinate cloverleaf pattern had been removed, it only departed in order to be replaced by an equally intractable two-lobe pattern (an example of which is shown in fig. 3.9).

With the setup simplified as much as possible, it emerged that the direction of travel of the beam as it left the EOM was dependent on the voltage; as we were switching polarization, we were also moving the beam (if only by a matter of microns for a beam several mm wide). This unavoidably evoked a two-lobe pattern like the one predicted in fig. 3.6. Wide-field illumination, it seems, is the only practical way to make the experiment work, at least using this (or perhaps any) EOM.

How did the periscope cause a cloverleaf pattern? We know, of course, that any reflection from a mirror will distinguish between *p*- and *s*-polarized light, and these depend on the angle between the mirror and the direction of propagation of the light. For a light ray travelling through a system of mirrors, then, the system of mirrors has a preferred (linear) polarization that depends on the angle under which the ray enters the mirror system.

Enter the system of mirror under a different angle, and the preferred polarization, and thus the final polarization state *after* the mirror system, may also be different. If, now, the left- and right-handed rays leave the EOM under different angles, their polarization state would be altered by the periscope (and all mirrors in the system) in slightly different ways. The elliptical polarisation states after the periscope would then have different characteristic directions, such as the ones in 3.7.

While this does not even come close to explaining the magnitude of the observed pattern, it is likely to play a part in the full answer (albeit perhaps a small one).

We were later successful in using the proposed photothermal technique in wide-field illumination mode to reliably measure the chirality of chiral gold nanostructures. This, however, falls outside the scope of this chapter, and of this thesis.

4 On picosecond-to-nanosecond heat transfer around a gold nanoparticle

We use pump-probe extinction spectroscopy to study the cooling dynamics of a single gold nanoparticle with picosecond time resolution. By continuously heating the nanoparticle, we can measure how nanoscale picosecond heat transfer dynamics from the particle to its environment change with temperature. We discuss the constraints laser-induced damage to the nanoparticle and its environment place on the measurement technique and contemplate picosecond control and investigation of vapour nanobubble formation.

4.1 Introduction

Heat transfer and boiling processes have been extensively studied at space and time scales most relevant to industrial processes, such as the cooling of apparatus ranging from hand-held devices to nuclear power plants. They have further been studied scientifically at all edges of that range, including at (tens of) nanometer size and (tens of) nanosecond time scales in chapter 2 of this thesis.

Measurements of heat transfer on *pico*second timescales have been reported e.g. for bulk metals [93], thin films [94, 95], and metallic nanoparticles [96, 97]. At small sizes in particular, the universally optical picosecond-time measurements involving heat transfer have, however, frequently been characterized by melting and laser ablation of the studied materials [23, 44, 98, 99], be it intentionally or not.

Many studies of heat transfer at picosecond time and nanometer size scales have focussed on heat transfer in metals, where processes are often fast and optical studies are feasible. Heat transfer involving metals, however, is a broad church and includes heat transfer from metals to their non-metal surroundings. In particular, cooling of metal nanoparticles, heated by a picosecond or femtosecond laser pulse, passing heat to their surroundings, has been studied thoroughly in the case where the nanoparticles are in equilibrium with their surroundings before the arrival of the laser pulse [97].

The extreme case of this problem — the absorption of a lot of energy in a short amount of time by a nanoparticle under pulsed illumination — can (besides ablation in one form or another) result in the formation of vapour nanobubbles, that is to say rapid boiling in the environment due to the large amount of deposited heat.

There have been some time-resolved studies of pulse-excited plasmonic vapour nanobubble dynamics based on pump-probe techniques, e.g. by Plech and co-workers using small-angle X-ray scattering (SAXS) and transient optical extinction [42, 100], and by Katayama et al. [101] using spectrally resolved transient optical extinction. The time resolution of these ensemble studies has been, however, limited to the tens of ps, all while they indicate that the dynamics of the earliest stages of nanobubble formation may well be faster. The dynamics of nanobubble formation *per se* thus appear to be obscured.

As Katayama et al. [101] point out, since their results are ensemble-averaged, the time resolution they can achieve is limited by the dynamical heterogeneity from nanoparticle to nanoparticle. To go down to the single picosecond, we must therefore (as, indeed, they point out) go to a single-particle experiment.

As we will be performing a stroboscopic pump-probe technique to achieve picosecond time resolution (see § 4.2.1), even without particle-to-particle differences, we may still be limited by dynamical heterogeneity: as the measurement requires integration over many millions of consecutive laser pulses (and thus boiling events), any variation of the behaviour from pulse to pulse will limit the experiment's resolution and fidelity.

There are several possible sources of pulse-to-pulse variation: Firstly, there may be a slow build-up of heat in the nanoparticle as the laser pulses arrive in rapid succession during the measurement. For each and every event to be equivalent to the last, the laser pulse fluences must be chosen to be low enough that the particle can dissipate all the heat it has absorbed before the next laser pulses arrive[1].

If the particle gets hot enough, it might melt, or, at least, there may be some degree of surface melting [102]. In and of itself, this may not be an issue — as long as the sample remains stable. The nanoparticle must not, however, reshape, shrink, shatter, drill into the substrate, or otherwise change [23, 103, 104] over the course of the experiment.

Further, if initial vapour nanobubble formation is limited by a process with some degree of randomness (such as diffusion), this may translate to a random 'speed' (for want of a better word) of boiling and bubble formation. After all, Hou et al. [41] found a random component in vapour nanobubble formation under continuous heating, which can also be seen in chapter 2 of this thesis, particularly fig. 2.3–II.

4.2 Method

4.2.1 Premise

We perform a transient optical extinction measurement in a pump-probe configuration. This means that we prepare two laser pulse streams, with a delay τ between the two pulse streams. Each time the first pulse, named the 'pump', reaches the sample, a single gold nanoparticle, it excites it, depositing

---

[1] There is no requirement for the particle to return to room temperature, it must merely be able to reach a stable equilibrium in which each event is indistinguishable from the last.

a certain amount of energy within. This kick-starts a process in which this additional energy escapes the particle in one way or another, primarily as heat. A delay τ later, the second pulse, dubbed 'probe', arrives and interacts with the sample as it is at the instant a delay τ after the sample was excited.

This is a well-known stroboscopic technique: because the probe laser is pulsed, we only get information about the state of the sample during the brief moments during the pulse. At each and every one of these moments, a pump pulse had arrived a time τ beforehand. The transmission of the probe beam by the sample then corresponds, in this configuration, to the transmission a time τ after excitation, and can easily be integrated over experimentally feasible time scales. If we now vary τ, we build up, point by point, a reconstructed time trace, or, a spectrum of the (mean) transmission as a function of time. The temporal resolution is limited in principle by the pulse widths of the two lasers.

So far for the 'traditional' technique — in an attempt to limit the sources of dynamical heterogeneity raised above, we introduce an additional, in this case continuous-wave, laser to the experiment. We use it to move away from what we might call 'extreme pulsed heating', and somewhat close to the experiment of chapter 2 and ref. [41]. The CW laser is used to heat the nanoparticle (and environs) to the point where it is nearly, but not quite, ready to explosively form a vapour nanobubble. In the language of § 2.3.1, we aim to hold the particle just below the boundary between régimes I and II.

With the particle so pre-heated, we hope (vainly, perhaps) to reduce any delay between the absorption of the pump pulse, the sudden kick across the threshold into boiling régime II, as it were, and the actual formation of the vapour nanobubble. This also reduces the amount of heat we need to supply in each laser pulse, as well as the maximum temperature within the particle, which may reduce the risk of damage to the sample.

4.2.2 Gold nanoparticle excited by a laser pulse

From the gold nanoparticle absorbing a laser pulse to the absorbed energy having been fully dissipated, a number of processes occur at well-separated time scales:

First of all, the laser-excited electrons thermalize with the remaining electron population on a time scale on the order of 10 fs [22]. In our case, the laser pulses have a pulse length on the order of hundreds of fs, meaning this process

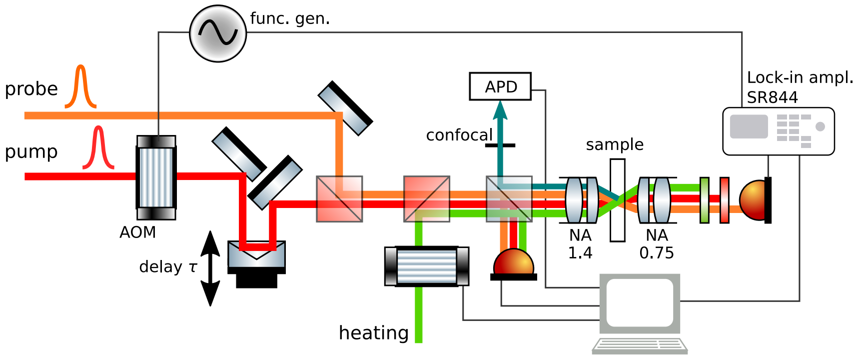

Figure 4.1: Sketch of the main components of the experimental setup. The time-resolved extinction measurement comes from a fast photodetector (right) via the lock-in amplifier.

happens while the energy is being absorbed and is too fast to detect. The electrons reach temperatures on the order of 10^3 K (see chapter 5), which shifts and broadens the plasmon resonance, and is therefore visible. Secondly, heat is transferred from the hot electrons to the metal lattice on a timescale of some picoseconds [105] .

Thirdly, heat is transferred out into the medium and diffuses outwards into the bath. This typically occurs on a timescale on the order of hundreds of picoseconds. At the same time, the sudden heating of the nanoparticle launches it into a mechanical breathing mode. The period of these oscillations depends on the size of the nanoparticle and is on the order of ~10 ps. They are among the most striking features of the time traces shown in this chapter, and have been studied extensively in the past [106, 107], but for the purposes of this chapter they are incidental to the measurement technique and will not be discussed in any detail.

4.2.3 Experimental details

Three laser beams are tightly focussed on a single 80 nm gold nanoparticle. Two of them are synchronized sub-ps pulsed lasers with a repetition rate of 75.8 MHz: a titanium sapphire in the near infrared ($\lambda = 785$ nm), which will excite the nanoparticle, pumps a frequency-doubled optical parametric oscillator (~600 nm), used to probe the system. The delay τ from one pulse to the other is varied using a mechanical delay line with a length of 1 ns, and is defined such that a positive delay $\tau > 0$ corresponds to the visible probe pulse arriving after the pump pulse.

A scheme of the experimental setup is shown in fig. 4.1; we measure the light from the probe beam that is transmitted through the sample using a fast photodetector (FEMTO Messtechnik), which is equivalent to measuring the extinction of the beam[2]. To make small changes in an already weak signal from a single nanoparticle measurable, we use a lock-in detection mode.[3] The intensity of the pump laser beam is modulated with an acousto-optic modulator (AOM) at ~1 MHz, which allows a lock-in amplifier (Stanford Research Systems SR844) to extract the effect of the pump pulse on the extinction measurement by locking in on the modulation frequency.

The integration time of the lock-in amplifier is set to 30 ms. Meanwhile, the delay line is slowly moving, covering 0.25 ps every 30 ms (corresponding to $1.25\,\mathrm{mm\,s^{-1}}$). The output of the amplifier is recorded every 60 ms, which produces an ultrafast time trace (a.k.a. a pump-probe spectrum) of the response to excitation by the pump pulse with a resolution of 0.5 ps, where every datapoint corresponds to 4.5 million laser pulses.

The third laser beam, a continuous-wave laser with a wavelength of 532 nm, is used to pre-heat the nanoparticle. Its intensity is controlled with a second AOM and is kept stable throughout the acquisition of each spectrum.

The nanoparticles are deposited on a cover slip, either borosilicate glass (Menzel) or fused silica, and the cover slip is attached to a PDMS cell holding a reservoir of water. The nanoparticles are thus attached on one side to glass, and otherwise surrounded by water. In the case of borosilicate glass, the cell is a flow cell attached to tubes whose ends are some 15 cm from the nanoparticle. In the case of the fused silica substrate, the cell is sealed. In either case, the depth of the reservoir (perpendicular to the substrate) is on the order of ~100 µm, and the extent parallel to the substrate is several millimetres (or, along one direction of the flow cell, centimetres). More succinctly, the reservoir is very large compared to the nanoparticle.

In order to move the particles into the focus of the microscope, the sample is mounted on a piezoelectric 3D nanopositioning system (Physik Instrumente).

---

[2] Nota bene, both scattering and absorption contribute significantly to the extinction.

[3] An alternative strategy would be to integrate for a very long time, which is the approach used in chapter 5.

4.2.4 Measurement protocol

The measurements presented herein were performed following the same basic protocol: After ensuring that the experimental setup is well-adjusted, a single nanoparticle with the expected behaviour (without additional heating) is selected. A series of pump-probe time traces with different CW heating intensities are then recorded:

First, we ensure the particle is in focus by scanning the focus across 1 µm along each of the Cartesian axes and optimizing the CW-excited photoluminescence at low intensity. Then, the AOM in the CW heating beam path is set to switch to a target heating power. The heating power is measured before the objective. The shutters blocking the pulsed laser beams are then opened, and a pump-probe time trace is acquired by scanning the delay line from slightly negative delay (probe arrives before pump) to positive delay (pump arrives before probe). Once the time trace has been acquired, the process is repeated.

We start at low heating and move to higher heating power step by step. In order to distinguish reproducible behaviour from irreversible changes to the nanoparticle, we alternate between acquisitions without CW heating and acquisitions with non-zero CW heating: each heated measurement is preceded and succeeded by one without heating. All measurements without CW heating should give the same result; if they do not, we know that there has been some irreversible change to the sample (e.g. damage to the nanoparticle or its surroundings).

4.3 Results

4.3.1 Preliminary measurements on borosilicate glass

Fig. 4.2a shows the measurements as they were meant to be, with the required consistency for measurements at zero heating. The time traces show the documented features: an initial spike lasting a few picoseconds at $\tau = 0$. This is due to the high initial temperature of the conduction electrons. After those first few picoseconds, we see a slow decay of the excitation into the environment, and the breathing mode oscillations of the particle. The decay constant of heat transfer from the particle into the environment appears to be slightly altered for the heated particle.

If we heat the same particle more (fig. 4.2b), however, we begin to see telltale

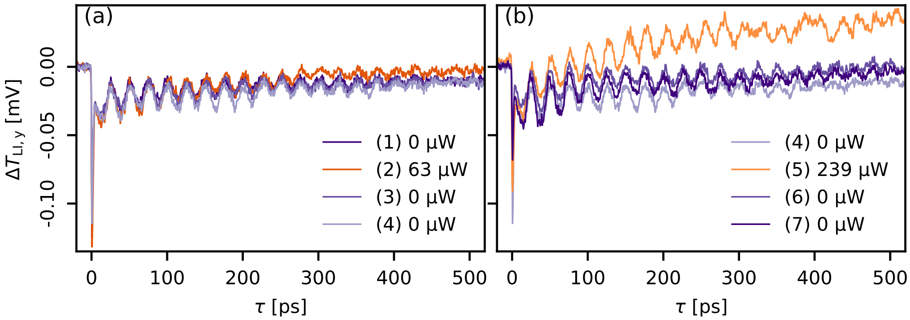

Figure 4.2: Example time traces on borosilicate glass for one nanoparticle, split across two panels for clarity. Numbers (*n*) indicate the order in which they were measured. Powers are CW heating powers in the back focal plane. **(a)** Three traces at zero heating, before and after non-zero heating, which are, as intended, identical. The trace with non-zero heating shows a slight shift. **(b)** A higher heating intensity time trace shows a markedly different result; the zero-heating time traces before and after are inconsistent with each other, indicating possible damage to the nanoparticle.

signs of damage to the particle: a measurement with zero additional heating after the fact (traces (6) and (7)) is inconsistent with a measurement ante hoc (trace (4)). Since the acquisition of a such a time trace takes a finite amount of time during which the particle may change, we cannot tell, from looking at a measurement such as trace (5) in fig. 4.2b, which parts of it are due to the change in pulse-to-pulse delay τ, and which are due to slow changes to the particle *unless* we know with some degree of certainty that the particle has not, in fact, changed.

In the example in fig. 4.2b, the irreversible change to the particle appears to be slight, and the 'hot' trace (5) in particular bears some resemblance to the measurements presented as probable nanobubble time traces in Lei Hou's thesis [108]. However, not only has the particle already changed slowly, but, in subsequent measurements (at higher heating), its pump-probe behaviour changes very dramatically, as seen in fig. 4.3a.

A major contributing factor to the contrast of these time traces is the plasmon resonance shifting, slightly, due to the excitation. It stands to reason that the sign of this change corresponds to the slope of the spectrum at our probe

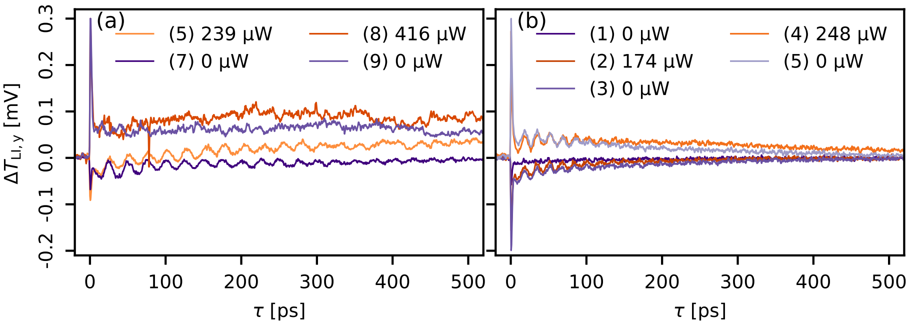

Figure 4.3: Examples of a drastic change in behaviour after heated pump-probe time traces. **(a)** Measurements of the same particle as fig. 4.2; two traces are shown both here and in fig. 4.2b for comparison. **(b)** Example of similar behaviour on a different particle.

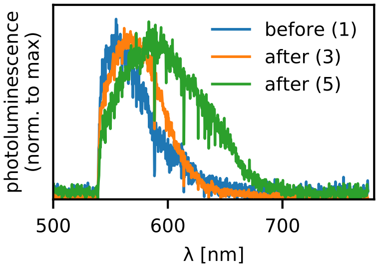

Figure 4.4: Photoluminescence spectra (excited at 532 nm) of the particle from fig. 4.3b at the start of the measurement, and after two subsequent heated time-trace acquisitions, showing a significant shift in the PL peak.

wavelength $\partial/\partial\lambda[\sigma_{\mathrm{sca}}(\lambda_{\mathrm{probe}})]$. The change in sign seen in 4.3a and for many other particles, e.g. in fig 4.3b, is therefore likely to correspond to a shift in the plasmon resonance from one side of the probe wavelength to the other.

Indeed, photoluminescence spectra, shown in fig. 4.4, evidence such a shift. After subsequent CW-heated pump-probe measurements, the resonance seen in the photoluminescence spectrum shifts to the red step by step. This may be due to an elongation of the initially spherical nanoparticle, or, more probably, due to localized ablation of the glass substrate [104].

In all our measurements on borosilicate glass, any significant change in the time traces was accompanied by such irreversible changes to the behaviour.

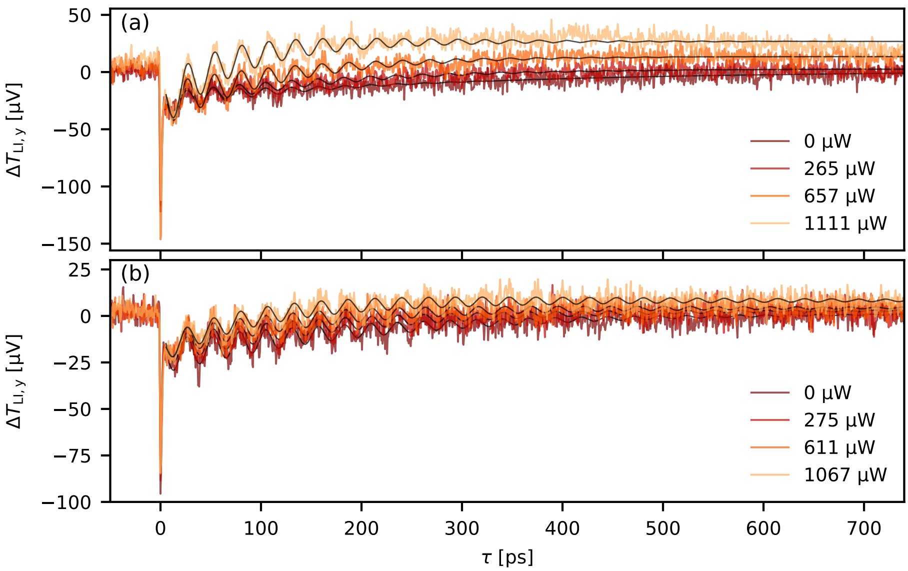

Figure 4.5: Selected time traces at different heating powers of two gold nanoparticles [**(a)** one, **(b)** the other] on a fused silica substrate. Black lines are fits to eq. (4.1).

4.3.2 Fused silica substrate

At this point we turn to fused silica as an alternative substrate with a higher melting point, making it more stable in the face of high heating, and damage to the substrate around the nanoparticle less likely.

This does not eliminate concerns about damage to the nanoparticles, of course, but it gives us a larger window of heating powers which we can use before damage sets in. At sufficiently high heating powers, damage to the particle looks much the same as it did on the borosilicate substrate, but at lower heating powers, significant changes to the time traces could be observed:

Fig. 4.5 shows illustrative time traces for two nanoparticles on the fused silica substrate for which the time traces at different heating powers were quite reproducible, and where there does not appear to have been any significant damage.

At higher heating power, the excited signal appears to decay more rapidly, but then, in several cases (e.g. fig. 4.5a), crosses the $\Delta T = 0$ line and changes sign to eventually decay to zero from the other side. Even when the signal does not change sign, what appears to be a faster decay rate is likely in fact caused by whatever effect causes traces with more pronounced effects to cross zero.

In order to parametrize the time traces without any regard for the physics of the processes at work, we use a simple function:

$$\Delta T_{\text{fit}}(\tau) \overset{!}{=} Ae^{-\alpha\tau} + Be^{-\beta\tau}\cos\left(2\pi\nu\tau + \varphi\right) + C. \tag{4.1}$$

Here, the parameters A and α describe the initial decay, C is the value the decay appears to approach, and B, β, ν and φ describe the particle's breathing mode oscillations and their decay. Note that this fit does not describe the decay back to zero from C which can be seen well in the highest-power trace of fig. 4.5a after some 500 ps.

The derived fit parameters for the measurement series the traces in fig. 4.5 are shown in fig. 4.6. We can look at the fit parameters both as a function of heating power, to determine how the behaviour of the particles depends on the heating, and also as a function of real experimental time elapsed. Doing the latter is important since we know there is a risk of the particle and substrate changing slowly over time.

Recall, at this point, that we alternate between heated and non-heated acquisitions in our measurements. Every heated time trace, and thus every point in the plots in 4.6 at $P_{\text{cw}} \neq 0$ is preceded and succeeded by ones at $P_{\text{cw}} = 0$. Furthermore, we move from low heating power to high heating power. Considering this measurement protocol allows us to interpret the plots of the fit parameters as a function of experimental macro-time:

If a parameter does not depend on heating power, and does not drift over time, it will remain constant to within the experimental noise envelope over the entire plot. This is the behaviour of φ. If a parameter does depend on heating power, but does not drift independently over time, the macro-time plot should be split into two branches: one branch, the 'heated' branch, will change over time (with the heating power); the other, the $P_{\text{cw}} = 0$ branch, will remain constant. The plots for A, α and C are examples of this behaviour. If a parameter drifts independently over time reflecting some irreversible change to the nanoparticle, the plot will reflect this drift. The plot for B in 4.6a shows this behaviour clearly; both plots for ν show it somewhat less clearly.

The three parameters that we would expect to describe heat transfer from

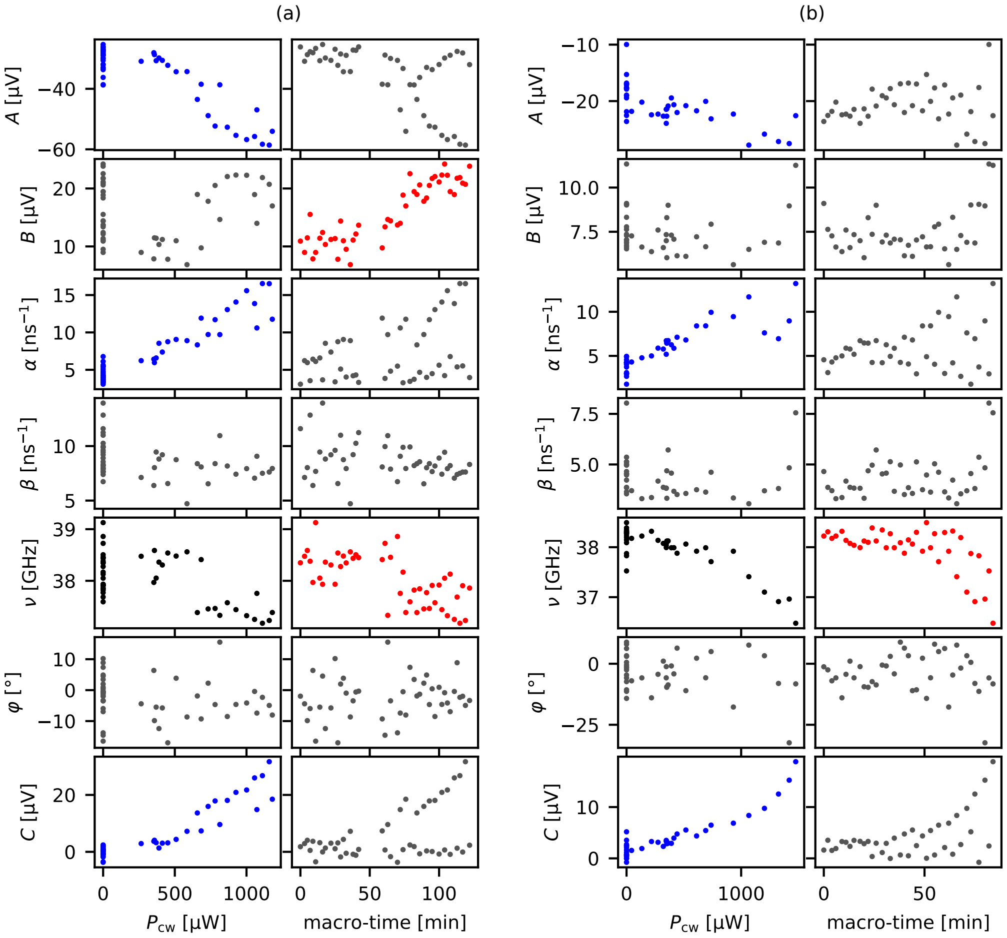

Figure 4.6: All fit parameters according to eq. (4.1) of all time traces of the particles from fig. 4.5, as a function of both CW heating power (left columns) and wall time from the first measurement of the series (right columns). Blue dots indicate parameters that appear to depend reproducibly on heating power. Red dots indicate parameters that show evidence of irreversible change over the course of the experiment. Grey dots permit no conclusion; ν (black dots) appears to show both a reproducible shift as a function of heating power and an irreversible change over time.

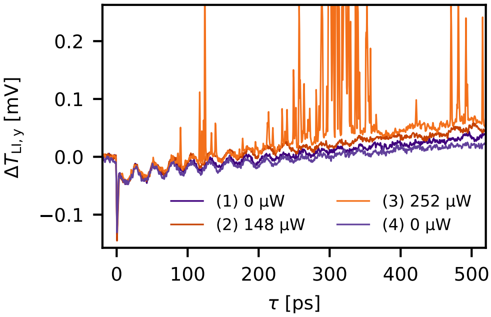

Figure 4.7: Representative example time traces in *n*-pentane, showing instability not observed in water.

the gold lattice into the environment in one way or another, A, α and C, then, do appear to depend reproducibly on the heating power. The oscillation frequency, ν, also appears to be reduced by higher heating power. This is an expected consequence of the change of the elastic moduli with temperature, and, since $\nu \propto R^{-1}$, of thermal expansion. However, ν also appears to drift over time.

These parameters appear to vary approximately linearly with heating power even as the nanoparticle is accumulating some degree of damage. There is no indication of a sharp nonlinear change in any of the parameters that may indicate the presence of a phase transition (such as bubble formation).

4.3.3 Other liquids

In order to encourage vapour nanobubble formation, we attempted the same experiment in other media with lower boiling points. In *methanol*, the time traces for practically all nanoparticles were inconsistent with each other to the point of absurdity, both on borosilicate glass and on fused silica. The inescapable and dramatic changes to the particle behaviour may be indicative of unintended (photo)chemical reactions.

In *pentane*, the time traces were generally more consistent, but any nanobubble formation that may have occurred was not synchronized with the laser pulses. Fig. 4.7 shows some example measurements in pentane; sudden spikes as seen in the highest-heating trace consistently appear at similar heating powers and are accompanied by no or little damage to the nanoparticle. They may correspond to spontaneous vapour bubble formation around the nanoparticle.

4.4 Discussion

We have measured picosecond extinction time traces of single gold nanoparticles under different CW heating conditions. At high heating, the change in extinction is observed to change sign before eventually decaying to zero.

It appears that two different contributions to the change in extinction with opposite signs are in competition with one another. At short times, one contribution dominates under all heating conditions, while at later times and high temperatures, the other contribution may become significant.

We can identify at least three subsystems whose temperature may affect the signal: the gold nanoparticle itself, the water it is surrounded by, and the fused silica substrate on which it sits. The temperatures of all three change, the refractive indices of all three depend on temperature, and the refractive indices (or: refractive index distributions) of all three will affect the signal.

At short times, before the absorbed heat has had time to diffuse into the surroundings, the signal is dominated by the change in the optical properties of gold. The 'starting point' at $\tau \approx 5\,\mathrm{ps}$ changes very little depending on the background CW heating power. Therefore, the properties of gold itself are unlikely to have much of an influence on the variation in the time traces.

At longer times, the temperature dependence of the refractive index distributions in the environment dominates the optical properties. At this point we can make note of the fact that the change of refractive index with temperature $\partial n/\partial T$ is negative for liquid water [109], but positive for fused silica [110].

We might imagine that the balance between the influence of the substrate and the influence of the medium shifts depending on the temperature. We know, in any case, that, for water,

$$\left(\frac{\partial n}{\partial T}\right)_p < 0 \qquad \text{and} \qquad \left(\frac{\partial n}{\partial T}\right)_V < 0$$

everywhere in the liquid phase so it does not appear that the measurements approaching zero from different sides can be due to the properties of the water alone.

4.5 Conclusion

We have measured dependence of picosecond time traces of the cooling dynamics of a heated single gold nanoparticle on the heating power. Surprisingly, the sign with which the optical extinction approaches equilibrium depends on heating power. This may be linked to the different thermal properties and the different signs of $\partial n / \partial T$ of the liquid medium and the adjoining substrate.

For the parameter range in which the nanoparticle is stable (i.e. its behaviour does not change irreversibly), no sign of vapour bubbles consistently triggered by the pump pulses was observed. In cases where the nanoparticle is *not* stable, it is impossible to discriminate between ultrafast dynamics which occur with every laser pulse and slow changes which occur over the duration of the measurement. The preliminary measurements by Hou [108] may have been linked to such slow changes.

When using pentane rather than water, thus lowering the temperatures needed for vapour bubble generation, measurements showed violent instability (fig. 4.7) somewhat reminiscent of explosive bubble formation as seen in real-time measurements (e.g. fig. 2.3–II). This might be a signature of random bubble formation that is not triggered consistently by the pump laser pulse, or even not linked to the laser pulse(s) at all.

If this is the case, and if the bubbles form in response to random fluctuations in temperature and pressure, this might be remedied by better control of those variables. It appears unlikely that attempting to control temperature and pressure at a macroscopic scale would result in the required nanoscale stability, but vapour nanobubble generation in a well-controlled microchannel or microchamber may be worth exploring.

If, on the other hand, random bubble formation occurs in response to thermal (Brownian) fluctuations of the sort that are fundamentally unavoidable at high temperature, then the enterprise of picosecond control of nanoscale boiling may be doomed from the outset. The attempt in this chapter of using laser pulses as an artificial small fluctuation that would ‘take precedence’ (in a manner of speaking), in any case, has not proven fruitful.

5 Time-resolved measurement of electronic temperatures in a single gold nanoparticle

Anti-Stokes nanoparticle photoluminescence, in which light extracts energy from the thermal bath in the nanoparticle, is an indicator of the temperature prevalent within a nanoparticle. We use it to measure the electron temperature in a single gold nanoparticle under pulsed illumination (~10^3 K) and its strikingly nonlinear dependence on pulse energy. Pump-probe anti-Stokes spectroscopy allows us to measure ultrafast dynamics of a pulse-excited hot electron population with sub-picosecond time resolution. We measure the heating and cooling, all within picoseconds, of the electrons and find that the highest apparent temperature state is reached 0.6 ps before the maximally excited state.

5.1 Introduction

5.1.1 Background

Plasmonic nanoparticles are remarkable in their ability to couple to light whose wavelength is significantly larger than their size. This property is primarily due to their localized surface plasmon resonance — a resonance of collective electron oscillations enabled by the spatial confinement of the electron gas.

Leaving aside the rich physics created by various nanoparticle geometries, from tunable spectroscopic properties to powerful near-field effects, absorption of light by a plasmonic nanosphere can be understood in the following simplified way:

If the dielectric permittivity of the material is known, the key parameters of scattering and absorption can be calculated using Mie theory. For far-field interactions, these are conveniently given in terms of cross sections: the scattering cross section σ_{sca}, the absorption cross section σ_{abs}, and the extinction cross section $\sigma_{\mathrm{ext}} = \sigma_{\mathrm{sca}} + \sigma_{\mathrm{abs}}$. Through σ_{abs}, we have access to the rate at which energy is absorbed by the nanoparticle, and thus to the amount of energy that must (eventually) leave the nanoparticle when it equilibrates with its environment.

The vast majority of the energy absorbed is converted to heat, which the (now hot) nanoparticle will dissipate. A vanishingly small fraction of the energy absorbed goes towards radiative emission channels referred to as photoluminescence; while this emission is measurable and useful — and indeed central to the technique used in this chapter — for the purposes of the energy balance, it can safely be neglected ($P_{\mathrm{pl}} \ll P_{\mathrm{heat}}$). This approached based on scalar cross-sections is the approach taken in the previous chapters of this thesis.

While this simple picture works well for low-electric-field near-steady-state continuous-wave excitation, it ignores the dynamics of light absorption, and the ultrafast heat transfer dynamics which occur in the metal. These come to the fore in particular when a plasmonic nanoparticle is excited with a pulsed laser with a pulse width below about a picosecond.

Ultrafast laser absorption in a metal, be it in a nanoparticle, a film, or bulk metal, is typically modelled using a two-temperature model; the electron gas and the metal lattice are treated as two distinct coupled subsystems with independent temperatures. In bulk metal, both temperatures must be treated as temperature fields varying in space. In nanoparticles that are sufficiently small compared to the wavelength and focus size of the heating laser, we can assume uniform heating. The temperatures of the electrons and of the lattice can then be taken to be constant across the entire volume of the particle, and may be treated as scalars.

In the two-temperature model, under ultrafast laser excitation, we typically assume the electrons are heated to some temperature $T_e(t = 0)$ instantaneously. This requires that the temperature be well-defined, i.e. that the electrons thermalize to a Fermi–Dirac distribution with no significant delay. The characteristic thermalization time is of order ~0.5 ps in gold [22, 111]; however, the electron distribution being instantaneously non-thermal barely has an impact on most measurements, especially if the excitation pulse width is of the same order. Assuming instantaneous thermalization, we model the evolution of the temperatures using the following coupled ordinary differential equations [105]:

$$C_e(T_e)\frac{\mathrm{d}T_e}{\mathrm{d}t} = -G(T_e - T_l) \tag{5.1}$$

$$C_l\frac{\mathrm{d}T_l}{\mathrm{d}t} = G(T_e - T_l) - Q_{\mathrm{bath}}(T_l), \tag{5.2}$$

where T_e and T_l are the temperatures of the electrons and the lattice, C_e and C_l are the corresponding heat capacities, G is an electron–phonon coupling constant, and Q_{bath} represents heat transfer from the lattice to the environment. Note that the electronic heat capacity depends on the electronic temperature. The electronic excitation generally relaxes within a few picoseconds, while the lattice cools down over a longer period of time, which is limited by the thermal properties of the environment, especially the thermal conductivity and, for small particles in particular, the interfacial thermal resistance. Under typical conditions, relaxation of the lattice takes place over a period of hundreds of picoseconds.

Because of the low heat capacity of the electrons (viz. about $2 \times 10^{-2}\,\mathrm{J\,cm^{-3}\,K^{-1}}$ [105], or 0.8 % of that of the gold lattice, at STP), the instantaneous temperature of the electrons upon pulsed excitation is very high. It has been estimated under various conditions to reach into the thousands of kelvin under modest illumination, both indirectly from extinction and/or scattering measurements [105, 112, 113], and more directly, using anti-Stokes emission (see § 5.1.2).

The two-temperature model, by allocating the electrons to a Fermi distribution with a certain elevated temperature T_e at time zero, does not take into account how the electrons got there. Considering this is important for two main reasons: Firstly, if the excitation laser pulse width is comparable to the electron–phonon coupling time, then they must, in principle, be considered together. Secondly, there is no reason to believe that optical excitation of the electron gas yields a thermal distribution of electrons, and this must be considered if the excitation laser pulse approaches the electron–electron coupling time. Indeed, several studies have considered non-thermal electron distributions and how they thermalize [22, 114–116].

5.1.2 Anti-Stokes emission as a measure of temperature

When a nanoparticle is illuminated at a suitable wavelength, it can be detected optically, either through elastic (Rayleigh) scattering, in which the detected photons have the same energy as the illumination, or through inelastic processes, in which the detected photons have either gained energy from or lost energy to the nanoparticle. If the emitted photons have a higher energy (blue-shift), this is known as an anti-Stokes process, if they have a lower energy (red-shift), a Stokes process.

The simplest such inelastic process would be a single scattering event, in which a single incoming photon interacts once with a single particle (such as an electron, a hole, or a phonon) in the material, exchanges some energy and momentum with it, and is reemitted. Such lowest-order processes are collectively known as Raman scattering. A wide variety of higher-order processes may also occur: an interaction may involve two or more photons, or two or more electrons. The photon or photons may create an excited state, and this exciton may then decay radiatively some time later after some number of interactions with electrons, holes, and phonons.

All this is vague enough to be true for any sample which interacts with light, but which types of interactions will dominate varies considerably. The main variable here is the availability of excited states: in insulators or semiconductors with a band gap greater than the photon energy, any excited states are negligible and the inelastic interactions are dominated by the lowest order process, Raman scattering. In molecules and semiconductors which happen to have long-lived excited states resonant with the incoming light, these, instead, dominate the inelastic emission. This is known as fluorescence.

In metal nanoparticles specifically, excited states (electron-hole pairs, and, collectively, localized surface plasmon polaritons) are available, but they have relatively short lifetimes on the order of tens of femtoseconds [117]. This means that they do not dominate and that the excitons only experience a limited number of interactions with the thermal bath. In other words, the excited states decay radiatively before they have fully thermalized with their environment — this is known as 'hot' luminescence.

In general, certainly in metals, Raman scattering and hot luminescence will always occur together [118], and cannot easily be distinguished from one another in practice. In any case, energy is gained and lost through interactions with the thermal bath. Thus, anti-Stokes emission, in which the emitted photons have an energy $\hbar(\omega_L + \delta\omega)$, which is larger than the energy $\hbar\omega_L$ of the laser illumination, can only occur to the extent that occupied states with an energy of $\epsilon = \hbar\delta\omega$ from which energy can be extracted are present in the metal. Both phononic and electronic states may, in principle, contribute, to these processes[1].

The emission spectrum will depend on on the energy distribution of occupied 'hot' states which might donate energy, $n(T, \epsilon)$. Broadly speaking, this will follow a Boltzmann-type distribution: If hot electrons dominate the interactions, which is likely at large $\delta\omega$ due to the higher temperature achieved by the electrons, it should obey Fermi–Dirac statistics. If, on the other hand, interactions with phonons dominate, it should follow Bose–Einstein statistics. In practice, the differences between the predictions of the three distributions are marginal for range of $\delta\omega$ which we have access to experimentally[2]. The emission can then be used to deduce an electronic temperature which matches up well with *a priori* predictions [119, 120] and, by extrapolating to zero laser heating, to measure the temperature of the environment [121].

In the following, the term 'photoluminescence' will be used for inelastic emission in a broad sense, without prejudice as to the mechanism which causes it.

---

[1] The terminology of Raman scattering is a case in point: 'traditional' Raman scattering exchanges energy with vibrational states, while electronic Raman scattering is universally couched in terms of scattering with quasi-free electrons, which dominate the behaviour of metals

[2] Nota bene, other authors have made the same observation about their measurements. [119]

5.2 Method

5.2.1 Premise

We probe the dynamics which occur in response to pulsed irradiation of a gold nanosphere using time-resolved anti-Stokes spectroscopy; to achieve ultrafast time resolution, we use a two-colour pump-probe technique:

Two ~ 350 fs laser pulses are sent to the sample with a particular delay τ between one and the other. The first, the 'pump' pulse, with a central wavelength of $\lambda = 785\,\mathrm{nm}$, is far to the red of the localized surface plasmon resonance of the nanosphere. The second, the 'probe' pulse, at $\lambda = 594\,\mathrm{nm}$, is near the resonance. We acquire emission spectra in the neighbourhood of 594 nm using spectral filters to remove the signal from the lasers and from elastic scattering.

Both colours are absorbed by the nanosphere, though the pump beam is absorbed significantly less efficiently. What's crucial is that since the pump laser is ca. 0.5 eV to the red of both our observation range and the plasmon resonance, (i) any possible emission is not enhanced by the plasmon, and (ii) whatever inelastic emission may be detectable without plasmon enhancement is spectrally separated from the probe signal. In other words, the pump is, on its own, effectively invisible.

The pump pulse creates some excited population of hot electrons $\Delta n_{\mathrm{ir}}(t,\epsilon)$. The probe pulse, arriving a delay of τ later, also creates an excited population of hot electrons, $\Delta n_{\mathrm{vis}}(t-\tau,\epsilon)$. However, its anti-Stokes emission depends on the total populations of electrons, which we may write as

$$n(t,\epsilon)\Big|_{t=\tau} = \Big[n_0(\epsilon) + \Delta n_{\mathrm{vis}}(t-\tau,\epsilon) + \Delta n_{\mathrm{ir}}(t,\epsilon)\Big]_{t=\tau} \tag{5.3}$$

if higher-order non-linear effects are small enough for the contributions of the two pulses to be additive. By varying the delay τ between the pump and probe pulses, as sketched in fig. 5.1, and examining the anti-Stokes spectra due to the probe, we can then elucidate the dynamics of $\Delta n_{\mathrm{ir}}(t,\epsilon)$ and the electron temperature with sub-picosecond time resolution.

5.2.2 Experimental details

Two correlated laser pulses are prepared using a titanium-sapphire (Ti:Sapph) laser, which produces a 75.8 MHz train of near-transform-limited pulses with

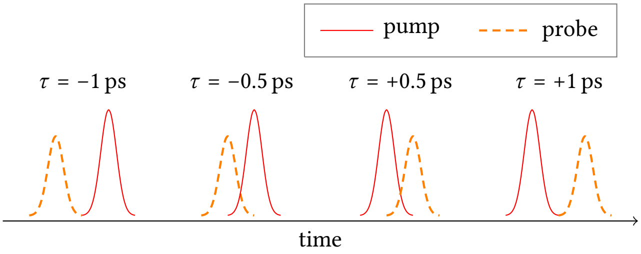

Figure 5.1: Visual representation of different pulse delays τ. Note that, typically, $\tau \geq 0$ for the pump pulse to have an effect on the measurement with the probe.

a central wavelength of 785 nm (the ‘pump’ pulses), and with a frequency-doubled optical parametric oscillator (OPO), which is pumped by the Ti:Sapph laser. The fact that one laser pumps the other means that every pulse from the OPO corresponds to a Ti:Sapph pulse — the two are locked together. The visible output of the OPO is tuned to 594 nm (the ‘probe’). Both pulses individually pass suitable dielectric band-pass filters which are well-matched to the notch filters in the detection. Additionally, we use a solid state continuous-wave 532 nm laser to identify particles, for fine adjustments, and for CW photoluminescence spectra.

The pulse width is measured to be equal to approximately 350 fs after an acousto-optic modulator in the beam path, which considerably lengthens the pulse. This component is needed only for the acquisition of transient extinction time traces (cf. chapter 4). Further optical components other than the objective should have little to no further effect on the pulse width; we can estimate the effect of the objective by approximating it as a solid block of glass with a length of ~5 cm; for BK7 glass, this would result in a negligible lengthening of the pulse by 0.06 fs (at 785 nm) to 0.14 fs (at 594 nm). The equivalent values for other glasses are similar.

The delay τ between the pulses is adjusted using an optomechanical delay line with a length of up to 1 ns in the path of the near-infrared (pump) beam. All three are then carefully overlapped and tightly focussed on the sample with an oil-immersion objective (Olympus, NA = 1.4). A second objective on the far side of the sample (Olympus, NA = 0.75) collects the transmitted light, which passes a spectral filter to remove the NIR component before

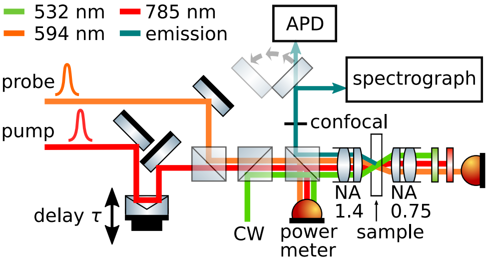

Figure 5.2: Highly simplified sketch of the experiment showing the logical beam paths.

being focussed on a fast photodiode (FEMTO Messtechnik). This arrangement allows measuring the change in extinction of the visible pulse as a function of inter-pulse delay and the acquisition of transient extinction time traces (as in chapter 4), but is further not required for the work discussed here. The pulse overlap is optimized using pump-probe extinction contrast (for the two pulses) and photothermal contrast (to overlap the pulses with the CW laser).

Meanwhile on the near side of the sample, the light (back-scattering and photoluminescence) collected by the NA = 1.4 objective is split off into the confocal detection path with a 50:50 beam splitter. After passing through a confocal pinhole (50 µm) and a series of notch filters for both colours, the emitted light is sent either to an avalanche photodiode, used for focussing, or to a liquid N_2-cooled spectrograph (Acton Research SpectraPro-500i). Fig. 5.2 shows a rough logical sketch of the beam paths from source to detection, disregarding most optical components.

Photoluminescence spectra are acquired with an integration time of 240 s, with the exception of some spectra recorded at very low or very high intensity.[3] All spectra shown here have been normalized by the integration time. Before the acquisition of each spectrum, the particle is brought into focus by maximizing photoluminescence with an automatic focussing routine. This is done to compensate for any slight drift in the system that may occur over the course of a long measurement. During the acquisition, the inter-pulse delay τ is kept constant.

Quoted pulse energies are measured as average powers in the back focal plane, before the objective, as indicated in fig. 5.2. They are not normalized by the transmission of the objective or by the absorptivity of the sample.

---

[3] The very long integration time is necessitated by the low intensity of the signal from a single nanoparticle. In chapter 4, the need for such long integration times is obviated by the use of a lock-in scheme.

The sample consists of 100 nm gold nanospheres (Nanopartz Inc.) spin-coated on a glass cover slip (Menzel). Spheres were chosen as other geometries are more liable to reshape under pulsed illumination. The nanoparticles are very dilute; in all cases the nearest neighbour of the nanoparticle being studied was more than ~2 µm away. The nanoparticles on the glass are further immersed in a reservoir of ultrapure water.

5.3 Results

5.3.1 Dependence of the electronic temperature on intensity

In order to establish clearly which parts of the resulting anti-Stokes spectra are due to heating by the probe pulse — in the language of eq. (5.3), in order to get an idea of $n_0(\epsilon) + \Delta n_{\text{vis}}(\epsilon)$ — we first measure Stokes and anti-Stokes spectra of the nanoparticle using the probe alone, at different excitation powers. The spectra are shown in fig. 5.3.

In general terms, if the anti-Stokes emission results from interactions with a Boltzmann-form thermal bath, we can say that the intensity should follow

$$I_{\text{AS}}(\delta\omega) \propto f(\hbar\omega) g(\hbar\omega) \exp\left(\frac{-\hbar\delta\omega}{k_B T}\right), \tag{5.4}$$

where $g(\hbar\omega)$ represents a density of states and $f(\hbar\omega)$ represents a probability of emission. The use of a Boltzmann factor here disguises the distinction between the electron and phonon thermal baths, and is only justifiable if $\hbar\delta\omega$ is sufficiently large, i.e. far from the laser. In our measurements, the spectral filter blocking out the laser largely obscures the energy range in which this approximation breaks down.

Carattino et al. [121] could make two simplifying assumptions: firstly, since they were using nanorods rather than nanospheres, they could identify $f(\hbar\omega)$ with a sharp plasmon resonance; this approximation is not valid for spheres as their resonance is much broader. Further, they were operating far enough from the main interband transitions of gold to assume $g(\hbar\omega)$ is constant. As the resonance of gold nanospheres is much closer to the interband transitions, this approximation is not valid, either [122]. Their use of the surface plasmon resonance as a normalizing factor can therefore not be replicated here; this is consistent with the lack of apparent sign of the plasmon in the spectra in fig. 5.3.

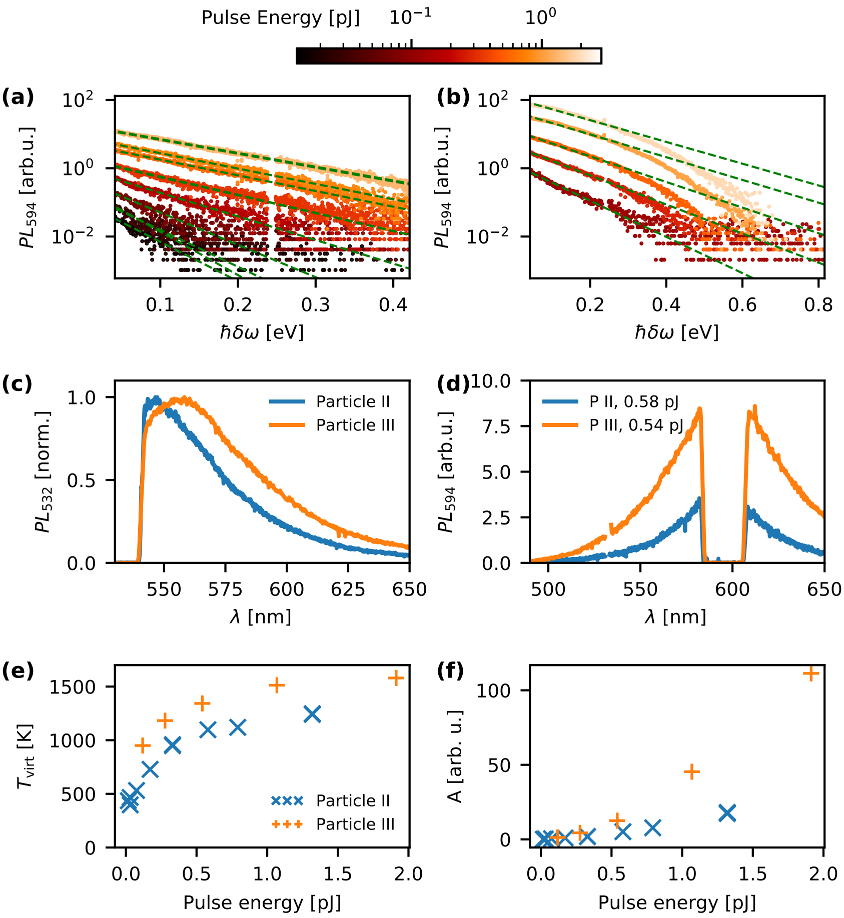

Figure 5.3: Anti-Stokes spectra of particles 'II' **(a)** and 'III' **(b)** excited by 594 nm pulses; different colours represent different pulse energies (colour bar above). Dashed lines are fits to the Boltzmann distribution, eq. (5.5). **(c)** Photoluminescence spectra of the same particles excited at 532 nm (CW). **(d)** Examples of spectra including the Stokes and anti-Stokes components, on a linear scale. **(e)** Temperatures derived from the fits. **(f)** Scaling factors A derived from the fits. The pulse energies quoted are measured in the back focal plane; note that the particles absorb only a fraction of the available energy.

We resort instead to a rather simpler approximation: we assume that the function $f(\hbar\omega)g(\hbar\omega)$ varies much more slowly than the exponential Boltzmann factor. This leaves us with

$$I_{\mathrm{AS}}(\delta\omega) = A\ \exp\left(\frac{-\hbar\delta\omega}{k_B T}\right), \tag{5.5}$$

where A is a proportionality coefficient.

Due to the lack of a *sharp* resonance, this approximation is reasonable sufficiently far from the interband transitions. The nearby interband transition at 470 nm [123] corresponds to $\hbar\delta\omega \approx 0.5\,\mathrm{eV}$ (i.e. $6 \times 10^3\,\mathrm{K} \times k_B$), at which point we do indeed clearly see the fits to eq. (5.5) break down in fig. 5.3b.

The same approximation has been used successfully by other authors in the past, such as He et al. [124] and Cai et al. [119]. Authors inclined to interpret similar measurements as electronic Raman scattering, such as Crampton et al. [120], instead assume that $f(\hbar\omega)g(\hbar\omega) \propto \omega^3$, which is practically equivalent to our approximation since ω^3 varies much more slowly than the Boltzmann factor.

This simplistic Boltzmann description fits the data well up to $\hbar\delta\omega \approx 0.4\,\mathrm{eV}$, at which point the approximations start to break down as expected. Note, however, that the extracted temperatures reflect the slope of logarithm of the data at lower values of $\delta\omega$ than that, and are thus not particularly affected by the interband transitions.

The temperatures T and amplitudes A, shown in fig. 5.3e and 5.3f respectively, broadly show the expected features:

(i) The temperatures reach >1000 K, and increase monotonically with increased heating power. The high temperatures indicate that we are indeed measuring the temperatures of the electrons, and not of the gold lattice.

(ii) The intensity of the anti-Stokes emission also increases with heating power, both due to the increased number of photons at higher powers, and due to the larger anti-Stokes to Stokes ratio at elevated temperatures. The combination of the two leads to a faster-than-linear increase.

(iii) The rate of temperature change with heating power $\partial T/\partial P$ slows with increased power. Multiple factors contribute to this surprising effect: On the one hand, the heat capacity of the electrons $C_e(T_e)$ increases as the temperature goes up, meaning the same amount of heat corresponds to a smaller temperature increase [105]. On the other hand, the permittivity, and thus the amount of absorbed heat, also depends on the temperature, which has been shown theoretically to lead to a similar slowing of the change in temperature [125, 126].

(iv) The temperature roughly approaches room temperature as $P \longrightarrow 0$. This is, however, far from exact for two main reasons. Firstly, extrapolating to zero power is not possible without greater knowledge of the nonlinear function $T(P)$, and secondly, the margins of error are substantial: on the one hand, the rather low signal-to-noise ratio at the lowest powers increases the uncertainty as the temperature decreases, and on the other, the approximations inherent in eq. (5.5) limit the reliability of exact quantitative conclusions in the first place.

Evidently, a more detailed model of the emission mechanism as well as the thermodynamic and photothermal effects in this system is needed to accurately calculate and understand the true electronic temperature, and its behaviour as a function of power.

Fig. 5.3 shows a remarkable heterogeneity between the two particles: particle III appears to be heated significantly more efficiently than is particle II, even though the particles have nearly the same size; this implicates other factors that may influence the absorption at 594 nm and elsewhere, such as the precise shape of the particles (including surface facets), interactions with the substrate, or crystal defects.

5.3.2 Hot electron dynamics

In the two-colour experiment, spectra are recorded while focussing two pulse trains on the particles, a probe pulse which causes the measured emission, and a pump pulse, whose direct effect is invisible. The delay between the pulses τ is varied from one spectrum acquisition to the next. τ is calibrated such that at positive τ the probe pulse arrives after the pump pulse, and such that $\tau = 0$ corresponds to the initial maximum of a 'traditional' pump-probe extinction time trace (such as those in chapter 4).

Fig. 5.4 shows such time-resolved spectra for three different 100 nm (nominal) gold nanospheres. The effect of the presence of the pump pulse on the spectra is limited to a period of ~1 ps; at longer delays the emission returns to its initial state. The change on the anti-Stokes side of the spectrum is significantly greater than the change on the Stokes side.

This aligns with our expectations, as the anti-Stokes emission is far more dependent on the temperature than the Stokes emission; changes in Stokes

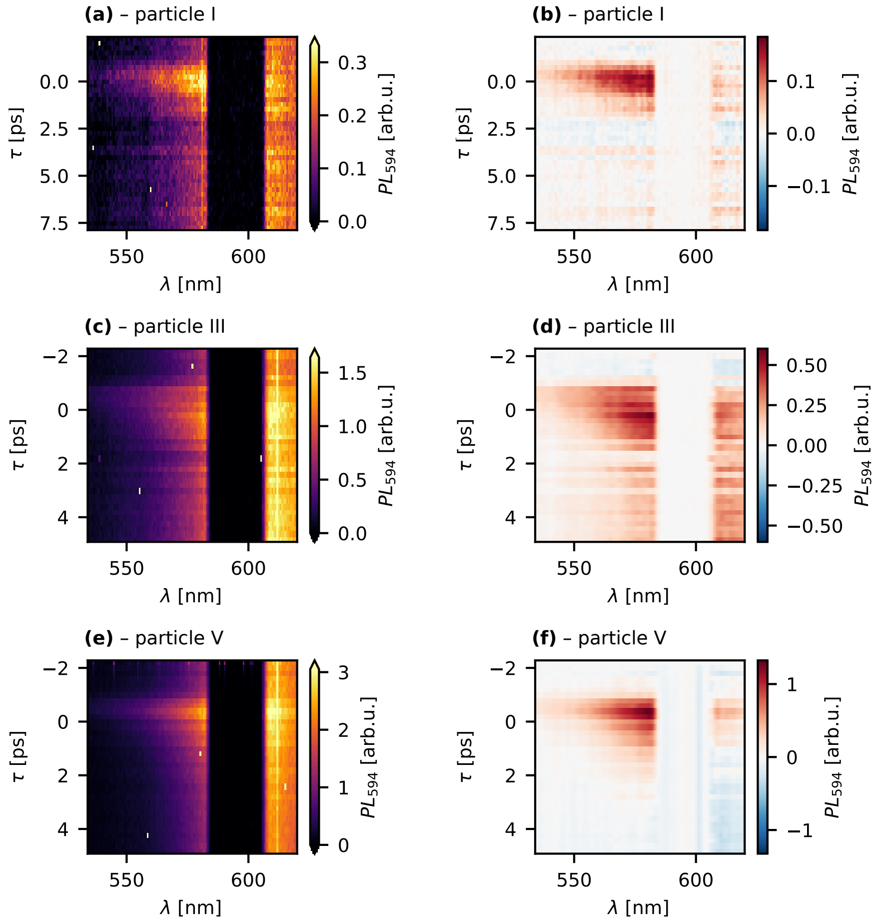

Figure 5.4: Time-resolved spectra of three different 100 nm (nominal) gold nanospheres, as a function of the wavelength λ and pump-probe interpulse delay τ. **(a,c,d)** The raw spectra on the left, **(b,d,f)** spectra with the τ-independent contribution of the probe pulse subtracted on the right, showing only the contribution of the pump pulse. Probe pulse energies were **(a,b)** (85 ± 3) fJ, **(c,d)** (119 ± 11) fJ and **(e,f)** (190 ± 11) fJ. The units on the colour scales are arbitrary but all equivalent to each other. $\tau = 0$ is defined as the peak of the pump-probe extinction spectra as shown in fig. 5.5.

emission due to elevated electron temperatures are due only to secondary effects, such as the change in the dielectric constant.

As stated in § 5.2.1, the measured anti-Stokes spectra are characteristic of the total electron distribution at the moment the probe pulse arrives, as given in eq. (5.3): they are characteristic of $n(t, T, \epsilon)|_{t=\tau}$. Here, two approaches for analysis present themselves:

For a straightforward parametrization, we can simply fit eq. (5.5) to the spectra for each time τ. The equation, now

$$I_{\mathrm{AS}}(\tau, \delta\omega) = A(\tau) \exp\left(\frac{-\hbar\delta\omega}{k_B\, T(\tau)}\right), \tag{5.6}$$

immediately gives us two time-dependent parameters that characterize the resulting emission quite well: a temperature $T(\tau)$ and a quasi-amplitude $A(\tau)$.

Alternatively, we can make use of the fact that $\left[n_0(\epsilon) + \Delta n_{\mathrm{vis}}(t - \tau, \epsilon)\right]_{t=\tau}$, i.e. the effect of the probe pulse alone, is independent of the inter-pulse delay τ to our advantage. Figs. 5.4b, 5.4d and 5.4f show the difference spectra

$$\Delta I_{\mathrm{AS}}(\tau, \delta\omega) = I_{\mathrm{AS}}(\tau, \delta\omega) - \hat{I}_{\mathrm{AS}}(\delta\omega) \tag{5.7}$$

if we subtract this τ-independent component, the baseline spectrum $\hat{I}_{\mathrm{AS}}(\delta\omega)$. For the purpose of parametrizing the entirety of the data, this approach is less practical since $\Delta I_{\mathrm{AS}}(\tau, \delta\omega)$ is overwhelmed by noise after a picosecond or two.

The parameters $A(\tau)$ and $T(\tau)$ resulting from a fit to eq. (5.6) are shown in fig. 5.5, along with the corresponding pump-probe extinction spectra from which $\tau = 0$ is calibrated. The magnitude of the change in the anti-Stokes spectra, represented by $A(\tau)$ follows the behaviour of the change in extinction well: Both have their maxima at the same inter-pulse delay, and both show the same asymmetric behaviour as a function of τ, with a steep rising edge as the pulse is absorbed, and a slower ~ ps decay as the absorbed energy is released into the metal lattice.

The highest apparent temperature state is, however, reached earlier. Across our measurements, temperature peaked around (0.66 ± 0.10) ps before the amplitude, which is almost twice our pulse width of 350 fs. The high-temperature state then rapidly decays to its initial value as the anti-Stokes intensity increases.

This early high-T, low-A state is easy to see in the spectra directly now that we know what we're looking for: Fig. 5.6 shows difference spectra from fig.

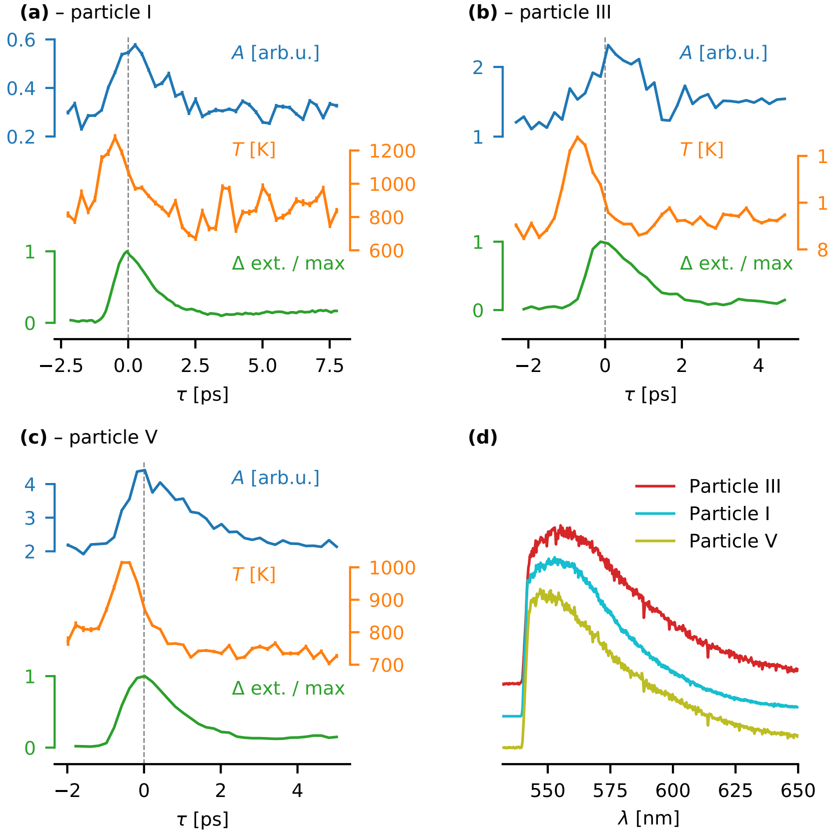

Figure 5.5: (a–c) Parametrization of the spectra in fig. 5.4 in terms of $A(\tau)$ [blue] and $T(\tau)$ [orange] according to eq. (5.6). The units for $A(\tau)$ are arbitrary but correspond to those used in fig. 5.4. Below: pump-probe extinction spectra [green] of the particles for comparison. **(d)** Photoluminescence spectra excited at 532 nm (CW) of the three particles, normalized to have the same maximum intensity and shifted for clarity.

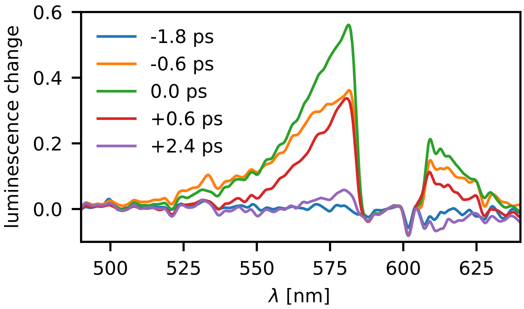

Figure 5.6: Difference spectra from fig. 5.4f: In order of increasing τ, the state before the pump pulse, the highest T state ($\tau = -0.6$ ps), the highest intensity state ($\tau = 0$), a slightly later state ($\tau = 0.6$ ps) and a late-τ state.

5.4f for selected delays τ. The highest-T spectrum, $\tau = -0.6$ ps, clearly decays much more slowly with decreasing λ than does either the tallest spectrum at $\tau = 0$ or indeed any later spectrum, such as the example from $\tau = +0.6$ ps.

The fact that the state of maximum temperature occurs so much earlier than the state of peak response in terms of both extinction and luminescence calls into question, at the very least, the implicit assumption that the peak of the pump-probe extinction spectrum, which we refer to as $\tau = 0$, corresponds to the pump and probe pulses arriving at the same moment.

The temperature changes due to the pump pulse as reported in fig. 5.5, some 300 K or so, appear quite low. This is an artefact caused by the underlying assumption of eq. (5.6): for the fit to give a good understanding of the temperatures, the entire hot electron gas would have to have a well-defined temperature, i.e., would have to be fully thermalized. In terms of eq. (5.3), it would require Δn_{ir} to have equilibrated with Δn_{vis} and n_0 before the emission of any photons.

As suggested above, we can get closer to that picture of the electron distribution by subtracting a baseline spectrum $\hat{I}_{\mathrm{AS}}(\delta\omega)$ from the full spectrum $I_{\mathrm{AS}}(\tau, \delta\omega)$ to arrive at the effect of the pump pulse alone, without the effect of the probe pulse. Just as with the full spectrum, we may then imagine it to be caused by a thermal distribution of electrons[4] and fit the spectra to a

---

[4] While we expect the initial distribution of hot electrons to be non-thermal [22, 114–116], and we see no *a priori* reason why the emission would be thermal, our data does not clearly show it to be otherwise.

	T from I_{AS}		T_Δ from ΔI_{AS}	
Particle	max	$\tau = 0$	max	$\tau = 0$
I	1278 K	1067 K	1661 K	1206 K
III	1279 K	958 K	1756 K	1004 K
V	1015 K	868 K	1306 K	936 K

Table 5.1: Apparent temperatures of the total spectra (figs. 5.4a, 5.4c, 5.4e and eq. (5.6)) and difference spectra (figs. 5.4b, 5.4d, 5.4f and eq. (5.8)) at maximum temperature and at $\tau = 0$. The values for the former correspond to those in fig. 5.5. Note the spectra for particles III and V were measured on the same day and with the same pump pulse energy, viz. ca. 2.2 pJ as measured in the back focal plane.

Boltzmann distribution:

$$\Delta I_{\mathrm{AS}}(\tau, \delta\omega) = I_{\mathrm{AS}}(\tau, \delta\omega) - \hat{I}_{\mathrm{AS}}(\delta\omega) \overset{!}{=} A_\Delta(\tau) \exp\left(\frac{-\hbar\delta\omega}{k_B\, T_\Delta(\tau)}\right). \tag{5.8}$$

The results of this fit for the high-T and high-A states are listed in table 5.1 alongside the corresponding values for the fit of the full spectra from fig. 5.5. It shows that the distributions created by the pump pulse initially have significantly higher characteristic temperatures than those present due to the probe pulse, which decays rapidly, as seen in the previous figures.

5.4 Discussion and conclusion

We have measured anti-Stokes photoluminescence of single gold nanoparticles due to pulsed illumination with characteristic temperatures of order 10^3 K. The temperatures are extracted using a simple Boltzmann approximation (eq. (5.5)) that fits well for intermediate anti-Stokes shifts that are not so small that the Boltzmann distribution would cease to apply, and that are not so large that the interband transitions of gold become significant.

The small-shift limit does not contribute to the measurement as the corresponding light is close enough to the laser to be rejected by our spectral filters. The large-shift limit barely contributes to the fit as the signal in that region is very weak in the first place. The extracted temperatures reflect the spectral region which the simple approximations are best suited to.

For a more exact and more precise extraction of the temperature from the photoluminescence spectra a more thorough model of the origin of gold nanoparticle photoluminescence is needed. Such a model may also provide more insight into the nature of the apparent temperature (i.e., is it entirely due to the electron temperature?). However, such a ‘full’ model should only amount to a modest correction to the deduced temperature.

In eq. (5.3) we assumed that the excited electron populations created by the two laser pulses are independent of one another. However, in fig. 5.3e, we see that dependence of the anti-Stokes spectra on pulse energy deviates significantly from linearity. This is not, in and of itself, terribly surprising: we know that the heat capacity of the electron gas and the dielectric permittivity both depend on temperature. The probe pulse energies used in the two-colour measurements are on the low side (~0.1 pJ, see fig. 5.4 caption), so the linear approximation inherent in eq. (5.3) may still be reasonable, but we cannot exclude interactions between the pulses that would affect the interpretation of these measurements.

It may be interesting to extend fig. 5.3e to higher pulse energies to establish whether the temperature saturates under strong illumination before melting of the particle becomes an issue.

We have shown in § 5.3.2 that the apparent temperature increase due to pulsed excitation decays on a ~ps timescale, which agrees with previous measurements of the electron-phonon coupling time. Surprisingly, the peak apparent temperature is reached early in the process (fig. 5.6), 0.6 ps before the peak amplitude. This time consistent with the thermalization times previously measured in bulk gold using time-resolved photoemission spectroscopy [111]. We note that what appears to be an early high-temperature state may in fact be a non-thermal state with a ‘hot electron’ contribution (which we measure) and a lower-temperature contribution (which is mostly obscured by the spectral filter near the laser).

This surprising observation may allow some deeper insight into the thermalization dynamics of the electron gas in a gold nanoparticle during the arrival of short laser pulses, if it were examined using a detailed model of the electron distribution and its evolution as a function of time.

All our results appear, however, to be consistent with a thermal distribution of electrons. We expect this is due to two main factors: Firstly, the probe pulse width is much longer than the electron scattering time (viz. <10 fs [22]) and of the same order of magnitude as the thermalization time. In short, there is plenty of time during the probe pulse for the electron distribution to approach a thermal one. Secondly, the spectral filter removing the laser obscures small energy shifts, which means we can't compare the distributions at low and at high energies as extensively as we might like.

Either one of these shortcomings could be improved somewhat, but there is a trade-off between the two: If one wanted to work with a shorter pulse, this pulse would inevitably have a larger bandwidth (at least 0.2 eV for ~10 fs, for instance), which would obscure more of the anti-Stokes spectrum. Vice versa, a much narrower filter would soon require the use of longer laser pulses.

Rather, to measure electron temperature dynamics using anti-Stokes emission, our measurements have to be integrated over a longer period of time (as they are here), and we must rely on theory to clear up the details.

Samenvatting

Nanodeeltjes van goud hebben werkelijk wonderlijke optische eigenschappen. Dat interacties tussen goud en licht bestaan, weet weliswaar iedereen — goud is niet transparant: goud glanst, zoals ieder metaal, en het heeft een karakteristieke gele kleur vanwege de eigenschappen van het atoom.

Maar als men deeltjes van goud produceert, bijvoorbeeld langs chemische weg, die een diameter van enkele tientallen of honderden nanometers hebben, heeft het goud een andere kleur: de oplossing van gouden nanodeeltjes is róód, niet goudgeel. Deze kleur is niet alleen afhankelijk van de eigenschappen van het atoom of van de structuur van het atoomrooster, maar ook van de grootte van het object, zélfs als het deeltje kleiner is dan de golflengte van het licht. Met name hierdoor worden gouden nanodeeltjes voor de nano-optica interessant: zij vertonen een sterke interactie met het licht, ook als ze zeer klein zijn. Deze interacties worden samengevat in de introductie in hoofdstuk 1.

Het merendeel van het licht, dat met een nanodeeltje interacteert, wordt óf verstrooid, óf geabsorbeerd. Dit laatste is voor dit proefschrift van bijzonder belang. Licht wordt door het deeltje geabsorbeerd, en door de wet van behoud van energie weten wij dat het deeltje hierdoor warmer moet worden. Dan hebben we een heel klein maar relatief heet nanodeeltje in een transparante omgeving, die niet of nauwelijks is opgewarmd. In dit proefschrift zitten de gouden nanodeeltjes altijd op een glasoppervlak, en zijn omgeven door een vloeistof. De warmte vloeit vanuit het nanodeeltje naar zijn omgeving.

Omdat de optische eigenschappen, o.a. de brekingsindex, van de meeste stoffen van de temperatuur afhangen, kunnen wij een verandering van temperatuur vaak optisch waarnemen. Dit is bijvoorbeeld het geval als de vloeistof in de buurt van een heet nanodeeltje opwarmt. De corresponderende foto-thermische effecten zijn het onderwerp van de hoofdstukken 2 en 3.

In hoofdstuk 2 wordt het nanodeeltje niet een beetje verhit, maar vrij veel. Zó veel, dat genoeg warmte vanuit het nanodeeltje de vloeistof eromheen instroomt dat deze begint te koken. Hoofdstuk 2 laat zien dat dit koken, waarbij een stoombelletje om het oppervlak van het hete gouddeeltje ontstaat, alleen vanaf een bepaald verhittingsvermogen stabiel is. Bij een kleiner vermogen is het koken om het nanodeeltje explosief en instabiel.

Dit gedrag op nanometerschaal verschilt niet zo veel van het koken in onze macroscopische wereld. Ook in een kookpan of een kerncentrale hangt het kookgedrag af van de temperatuur en het vermogen. Bij een relatief lage temperatuur ontstaan er, verdeeld over het hete oppervlak, toevallig kleine stoombellen, die af en toe het oppervlak verlaten en opstijgen. Dit is met het explosieve koken bij het nanodeeltje vergelijkbaar. Pas bij erg hoge temperaturen kan er een stabiele stoomlaag ontstaan tussen het hete oppervlak en de vloeistof, in het groot en in het klein. Desondanks zien we in de nanowereld wél verrassend gedrag, zoals soms verbazingwekkend stabiele trillingen van de nanobelletjes, die niet goed passen bij het gedrag dat we van een stoombel zouden verwachten.

Het 3de hoofdstuk gaat over iets heel anders, met name over chiraliteit. Iets is chiraal, als het niet op zijn spiegelbeeld lijkt. In de tweedimensionale ruimte (2D), en dus op dit blad, is de letter R een eenvoudig voorbeeld voor iets chiraals: hoe je hem ook draait en verschuift, je zal er nooit een Я van maken. Met dit voorbeeld kunnen wij ook meteen een belangrijke eigenschap van de chiraliteit zien: ze is afhankelijk van de dimensie! Als we de letter R in onze driedimensionale wereld meenemen kunnen we hem gemakkelijk omdraaien: wat van voren op een R lijkt, lijkt van achteren op een Я! Wat in 2D chiraal is, wordt in 3D spiegelsymmetrisch, en dus niet chiraal. En, als je er niet goed op let, kan het gebeuren dat een 2D-chiraal object er in een 3D-meting chiraal uitziet, hoewel het in 3D eigenlijk niet chiraal is.

De motivatie om chiraliteit in de nanowereld te onderzoeken is natuurlijk anders. Veel moleculen, die wij voor het leven nodig hebben, of nodig zouden kunnen hebben, zijn chiraal. Het is dus voor de geneeskunde en de farmacie zeer interessant om chiraliteit te kunnen meten. In hoofdstuk 3 wordt een manier voorgesteld, om middels het foto-thermisch effect (en daar zijn we weer bij het onderwerp van dit proefschrift) in de microscoop de chiraliteit van nano-objecten en van kleine hoeveelheden moleculen te meten. Wij bespreken de techniek en de moeilijkheden daarbij. Tot onze verbazing stellen we vast dat een niet-chiraal monster zelfs in een niet-chirale microscoop een chirale meting kan geven als het monster niet óf langs de optische as óf in een symmetrievlak zit. Uiteindelijk stellen we een aanpak voor, die het probleem weliswaar niet helemaal kan oplossen, maar het wel vele ordes van grootte kan verkleinen.

In hoofdstuk 4 en 5 worden de metingen ultrasnel: het gedrag van een enkel nanodeeltje wordt tijdsopgelost onderzocht met een nauwkeurigheid van minder dan een picoseconde middels een „pump-probe”–procedure. In hoofdstuk 4 gaat het over een nanodeeltje dat continu wordt verwarmd, en dus al heet is — er wordt gemeten hoe de bijkomende energie uit een ultrakorte laserpuls het deeltje verlaat. Het doel was om de eerste paar picoseconden van het leven van een nano-stoombel (net als in hoofdstuk 2) te bekijken, maar de vele korte laserpulsen beschadigen het deeltje bij deze temperaturen te snel.

In hoofdstuk 5 onderzoeken wij de temperatuur van de elektronen binnen het gouddeeltje gedurende het absorptie- en relaxatieproces. Hiertoe worden fotonen gemeten, die een kortere golflengte, en dus een hogere energie, hebben dan die van de laser — fotonen die energie uit de interactie met het gouddeeltje hebben gewonnen. Dit proces heet anti-Stokes-luminescentie en het geeft ons informatie over de energieën van de elektronen in het metaal, en dus over hun temperatuur. Hierbij zien we de heetste toestand ca. 0,5 ps voordat de relaxatie begint. Wij vermoeden, dat wij voor een enkel nanodeeltje de tijd meten van de excitatie totdat de elektronen een thermische verdeling van energieën volgens Fermi en Dirac hebben.

Acknowledgements

No doctoral dissertation is created in a vacuum, and neither was this one. As such, I must spare a few lines to mention some of the other people who have contributed in one way or another to my work here.

First and foremost, I would like to thank my supervisor, Michel Orrit, without whose constant support and critical eye this work would not have been what it is, and without whom this work would not have been possible in the first place. Next, my thanks go to Martín Caldarola, who kept an eye on me as a postdoc in Leiden, helping especially with the work that led to chapter 3, and continued to support me, with the work described in chapter 5 in particular, after he had left for Delft. Regarding chapter 3, I would also like to thank Benjamin Isaacoff, whose brief stay in Leiden started the chirality project, and Patrick Späth, who is keeping the project alive.

Various scientific aspects of this thesis have benefitted from conversations with colleagues from other institutions. In particular, I would like to thank Julien Lombard, Samy Merabia, and Yonatan Sivan for numerous fruitful discussions.

We might all be lost without the institutional support we rely on from day to day. On this front, I must thank Henriëtte van Leeuwen for her frequent help navigating all manner of administrative webs. I would also like to thank the electronics department, especially Peter van Veldhuizen, as well as Peter Gast, for their technical support.

The past four years would not have been the same without friendly and supportive colleagues: I would like to thank all other members of MoNOS for scientific and non-scientific conversation, cake, and a generally pleasant and cooperative working environment. In particular, I would like to mention by name Lei Hou, Biswajit Pradhan, Aquiles Carattino, Subhasis Adhikari, Siddharth Ghosh, Amin Moradi, and Martin Baaske.

Finally, and most importantly, I would like to thank my parents for their constant love and support. Thank you for being there for me through thick and thin.

Biography

I was born on 31 October 1990 in Starnberg, near Munich, and grew up in the nearby market town of Wolfratshausen. After completing my secondary education with the *Abitur* at Gymnasium Geretsried in 2010, I served at a workshop for people with a handicap, the Oberland-Werkstätten in Geretsried, for my *Zivildienst*.

In 2011, I joined Mansfield College, University of Oxford, to read Physics. Between my first and third year at Oxford, I spent several vacations working as a software developer at Mobile Software AG in Munich. My final year Master's project, entitled *'Developing a method for detecting influenza using wide-field fluorescence microscopy'*, was performed in the group of Professor Achillefs Kapanidis as a test case for the *Nanoimager*, a compact TIRF microscope — then a prototype, now produced and sold commercially by Oxford Nanoimaging Ltd — demonstrating its use for a sensing application. In July 2015, I graduated with a Master of Physics degree (MPhys, first class).

In October 2015 I joined the Single-Molecule Optics group at the Leiden Institute of Physics, Leiden University, as a PhD candidate supervised by Professor Michel Orrit, on a project financed through the NanoFront consortium, to study the behaviour of single vapour nanobubbles. Over the course of my time there, the scope of my work widened to include chirality and luminescence, and this thesis is the result. In 2016, I assisted in teaching the 'Molecular Physics' course in the 'Life Science & Technology' BSc, 2nd year, taught by Dr Martina Huber. In 2017, 2018 and 2019, I taught in the optics and electromagnetism practicals in the 1st year of the Physics BSc degree course under Professor Thomas Schmidt. From 2017 to 2019 I served as a delegate on the Institute Council.

List of Publications

- T. Jollans and M. Orrit, 'Een interferentie-experiment in je badkamer', Nederlandse Tijdschrift voor Natuurkunde **84**, 226–227 (2018).
- T. Jollans, M. D. Baaske, and M. Orrit, 'Nonfluorescent Optical Probing of Single Molecules and Nanoparticles', J. Phys. Chem. C **123**, 14107–14117 (2019).
- T. Jollans and M. Orrit, 'Explosive, oscillatory, and Leidenfrost boiling at the nanoscale', Phys. Rev. E **99**, 063110 (2019).
- P. Spaeth, S. Adhikari, L. Le, T. Jollans, S. Pud, W. Albrecht, T. Bauer, M. Caldarola, L. Kuipers, and M. Orrit, 'Circular Dichroism Measurement of Single Metal Nanoparticles Using Photothermal Imaging', Nano Lett. `10.1021/acs.nanolett.9b03853` (2019).

Bibliography

[1] J. Clerk Maxwell, ‘A dynamical theory of the electromagnetic field’, Philos. Trans. R. Soc. **155**, 459–512 (1865).

[2] M. Faraday, ‘The Bakerian Lecture.—Experimental relations of gold (and other metals) to light’, Philos. Trans. R. Soc. **147**, 145–181 (1857).

[3] P. Zijlstra, M. Orrit, and A. F. Koenderink, ‘Metal Nanoparticles for Microscopy and Spectroscopy’, in *Nanoparticles*, edited by C. de Mello Donegá (Springer Berlin Heidelberg, Berlin, Heidelberg, 2014), pp. 53–98.

[4] P. Zijlstra and M. Orrit, ‘Single metal nanoparticles: optical detection, spectroscopy and applications’, Rep. Prog. Phys. **74**, 106401 (2011).

[5] L. M. Liz-Marzán, ‘Nanometals: Formation and color’, Mater. Today **7**, 26–31 (2004).

[6] M. Grzelczak, J. Pérez-Juste, P. Mulvaney, and L. M. Liz-Marzán, ‘Shape control in gold nanoparticle synthesis’, Chem. Soc. Rev. **37**, 1783–1791 (2008).

[7] T. Woodcock and J. M. Robinson, *The Oxford Guide to Heraldy* (Oxford University Press, Oxford, 1988).

[8] P. W. Anderson, ‘More Is Different’, Science **177**, 393–396 (1972).

[9] S. H. Simon, *The Oxford Solid State Basics* (Oxford University Press, Oxford, 2013).

[10] G. Mie, ‘Beiträge zur Optik trüber Medien, speziell kolloidaler Metallösungen’, Ann. Phys. **330**, 377–445 (1908).

[11] P. Debye, ‘Der Lichtdruck auf Kugeln von beliebigem Material’, Ann. Phys. **335**, 57–136 (1909).

[12] L. Lorenz, ‘Lysbevægelsen i og uden for en af plane Lysbølger belyst Kugle’, Videnskab. Selskab. Skrifter **6**, 1–63 (1890).

[13] M. Kerker, *The Scattering of Light* (Academic Press, New York, 1969).

[14] C. F. Bohren and D. R. Huffman, *Absorption and Scattering of Light by Small Particles* (John Wiley & Sons, New York, 1983).

[15] O. Peña and U. Pal, ‘Scattering of electromagnetic radiation by a multilayered sphere’, Comput. Phys. Comm. **180**, 2348–2354 (2009).

[16] R. L. Olmon, B. Slovick, T. W. Johnson, D. Shelton, S.-H. Oh, G. D. Boreman, and M. B. Raschke, ‘Optical dielectric function of gold’, Phys. Rev. B **86**, 235147 (2012).

[17] M. Liu, P. Guyot-Sionnest, T.-W. Lee, and S. K. Gray, ‘Optical properties of rodlike and bipyramidal gold nanoparticles from three-dimensional computations’, Phys. Rev. B **76**, 235428 (2007).

[18] P. Zijlstra, P. M. R. Paulo, and M. Orrit, ‘Optical detection of single non-absorbing molecules using the surface plasmon resonance of a gold nanorod’, Nature Nanotechnol. **7**, 379–382 (2012).

[19] M. Otter, ‘Temperaturabhängigkeit der optischen Konstanten massiver Metalle’, Z. Physik **161**, 539–549 (1961).

[20] H. Reddy, U. Guler, A. V. Kildishev, A. Boltasseva, and V. M. Shalaev, ‘Temperature-dependent optical properties of gold thin films’, Opt. Mater. Express **6**, 2776–2802 (2016).

[21] K. Wôjcik, ‘The influence of point defects on selected properties of PbTio3 crystals’, Ferroelectrics **82**, 25–35 (1988).

[22] C. Voisin, N. Del Fatti, D. Christofilos, and F. Vallée, ‘Ultrafast Electron Dynamics and Optical Nonlinearities in Metal Nanoparticles’, J. Phys. Chem. B **105**, 2264–2280 (2001).

[23] D. Werner, A. Furube, T. Okamoto, and S. Hashimoto, ‘Femtosecond Laser-Induced Size Reduction of Aqueous Gold Nanoparticles: In Situ and Pump–Probe Spectroscopy Investigations Revealing Coulomb Explosion’, J. Phys. Chem. C **115**, 8503–8512 (2011).

[24] G. Baffou and R. Quidant, ‘Thermo-plasmonics: using metallic nanostructures as nano-sources of heat’, Laser Photonics Rev. **7**, 171–187 (2013).

[25] P. K. Jain, I. H. El-Sayed, and M. A. El-Sayed, ‘Au nanoparticles target cancer’, Nano Today **2**, 18–29 (2007).

[26] X. Huang, P. K. Jain, I. H. El-Sayed, and M. A. El-Sayed, 'Plasmonic photothermal therapy (PPTT) using gold nanoparticles', Lasers Med. Sci. **23**, 217 (2007).

[27] S. Lal, S. E. Clare, and N. J. Halas, 'Nanoshell-Enabled Photothermal Cancer Therapy: Impending Clinical Impact', Acc. Chem. Res. **41**, 1842–1851 (2008).

[28] P. Cherukuri, E. S. Glazer, and S. A. Curley, 'Targeted hyperthermia using metal nanoparticles', Adv. Drug Deliver. Rev. Targeted Delivery Using Inorganic Nanosystem **62**, 339–345 (2010).

[29] L. Durdevic, H. M. L. Robert, B. Wattellier, S. Monneret, and G. Baffou, 'Microscale Temperature Shaping Using Spatial Light Modulation on Gold Nanoparticles', Sci. Rep. **9**, 1–7 (2019).

[30] C. Liu, G. Tessier, S. I. Flores Esparza, M. Guillon, and P. Berto, 'Reconfigurable Temperature Control at the Microscale by Light Shaping', ACS Photonics **6**, 422–428 (2019).

[31] T. Jollans, M. D. Baaske, and M. Orrit, 'Nonfluorescent Optical Probing of Single Molecules and Nanoparticles', J. Phys. Chem. C **123**, 14107–14117 (2019).

[32] D. Boyer, P. Tamarat, A. Maali, B. Lounis, and M. Orrit, 'Photothermal Imaging of Nanometer-Sized Metal Particles Among Scatterers', Science **297**, 1160–1163 (2002).

[33] A. Gaiduk, P. V. Ruijgrok, M. Yorulmaz, and M. Orrit, 'Detection limits in photothermal microscopy', Chem. Sci. **1**, 343–350 (2010).

[34] M. Selmke, M. Braun, and F. Cichos, 'Photothermal Single-Particle Microscopy: Detection of a Nanolens', ACS Nano **6**, 2741–2749 (2012).

[35] L. Cognet, C. Tardin, D. Boyer, D. Choquet, P. Tamarat, and B. Lounis, 'Single metallic nanoparticle imaging for protein detection in cells', Proc. Natl. Acad. Sci. U. S. A. **100**, 11350–11355 (2003).

[36] D. Lasne, G. A. Blab, S. Berciaud, M. Heine, L. Groc, D. Choquet, L. Cognet, and B. Lounis, 'Single Nanoparticle Photothermal Tracking (SNaPT) of 5-nm Gold Beads in Live Cells', Biophys. J. **91**, 4598–4604 (2006).

[37] A. Gaiduk, M. Yorulmaz, P. V. Ruijgrok, and M. Orrit, 'Room-Temperature Detection of a Single Molecule's Absorption by Photothermal Contrast', Science **330**, 353–356 (2010).

[38] L. Hou, S. Adhikari, Y. Tian, I. G. Scheblykin, and M. Orrit, 'Absorption and Quantum Yield of Single Conjugated Polymer Poly[2-methoxy-5-(2-ethylhexyloxy)-1,4-phenylenevinylene] (MEH-PPV) Molecules', Nano Lett. **17**, 1575–1581 (2017).

[39] M. T. Carlson, A. J. Green, and H. H. Richardson, 'Superheating Water by CW Excitation of Gold Nanodots', Nano Lett. **12**, 1534–1537 (2012).

[40] J. Lombard, T. Biben, and S. Merabia, 'Nanobubbles around plasmonic nanoparticles: Thermodynamic analysis', Phys. Rev. E **91**, 043007 (2015).

[41] L. Hou, M. Yorulmaz, N. R. Verhart, and M. Orrit, 'Explosive formation and dynamics of vapor nanobubbles around a continuously heated gold nanosphere', New J. Phys. **17**, 013050 (2015).

[42] A. Siems, S. A. L. Weber, J. Boneberg, and A. Plech, 'Thermodynamics of nanosecond nanobubble formation at laser-excited metal nanoparticles', New J. Phys. **13**, 043018 (2011).

[43] É. Boulais, R. Lachaine, and M. Meunier, 'Plasma Mediated off-Resonance Plasmonic Enhanced Ultrafast Laser-Induced Nanocavitation', Nano Lett. **12**, 4763–4769 (2012).

[44] S. Hashimoto, D. Werner, and T. Uwada, 'Studies on the interaction of pulsed lasers with plasmonic gold nanoparticles toward light manipulation, heat management, and nanofabrication', J. Photochem. Photobiol. C **13**, 28–54 (2012).

[45] J. Lombard, T. Biben, and S. Merabia, 'Kinetics of Nanobubble Generation Around Overheated Nanoparticles', Phys. Rev. Lett. **112**, 105701 (2014).

[46] R. R. Letfullin, C. Joenathan, T. F. George, and V. P. Zharov, 'Laser-induced explosion of gold nanoparticles: potential role for nanophotothermolysis of cancer', Nanomedicine **1**, 473–480 (2006).

[47] V. P. Zharov, R. R. Letfullin, and E. N. Galitovskaya, 'Microbubbles-overlapping mode for laser killing of cancer cells with absorbing nanoparticle clusters', J. Phys. D: Appl. Phys. **38**, 2571–2581 (2005).

[48] X. Huang, P. K. Jain, I. H. El-Sayed, and M. A. El-Sayed, ‘Plasmonic photothermal therapy (PPTT) using gold nanoparticles’, Lasers Med. Sci. **23**, 217 (2008).

[49] D. Lapotko, ‘Plasmonic Nanobubbles as Tunable Cellular Probes for Cancer Theranostics’, Cancers **3**, 802–840 (2011).

[50] A. Abritis, *Caught Our Notice: 4th retraction for prominent physicist (with new funding) cites falsification*, Retraction Watch, (Nov. 6, 2017) `https://retractionwatch.com/2017/11/06/caught-notice-4th-retraction-prominent-physicist-new-funding-cites-falsification/` (visited on 09/22/2019).

[51] The PLOS ONE Editors, ‘Retraction: Improved Cellular Specificity of Plasmonic Nanobubbles versus Nanoparticles in Heterogeneous Cell Systems’, PLOS ONE **12**, e0187820 (2017).

[52] E. Y. Lukianova-Hleb, E. Sassaroli, A. Jones, and D. O. Lapotko, ‘Retraction of “Transient Photothermal Spectra of Plasmonic Nanobubbles”’, Langmuir **33**, 4090–4090 (2017).

[53] E. Y. Lukianova-Hleb and D. O. Lapotko, ‘Retraction: “Experimental techniques for imaging and measuring transient vapor nanobubbles” [Appl. Phys. Lett. 101, 264102 (2012)]’, Appl. Phys. Lett. **110**, 129901 (2017).

[54] T. Jollans and M. Orrit, ‘Explosive, oscillatory, and Leidenfrost boiling at the nanoscale’, Phys. Rev. E **99**, 063110 (2019).

[55] S. M. S. Murshed, C. A. Nieto de Castro, M. J. V. Lourenço, M. L. M. Lopes, and F. J. V. Santos, ‘A review of boiling and convective heat transfer with nanofluids’, Renew. Sust. Energ. Rev. **15**, 2342–2354 (2011).

[56] R. A. Taylor and P. E. Phelan, ‘Pool boiling of nanofluids: Comprehensive review of existing data and limited new data’, Int. J. Heat Mass Transfer **52**, 5339–5347 (2009).

[57] D. E. Kim, D. I. Yu, D. W. Jerng, M. H. Kim, and H. S. Ahn, ‘Review of boiling heat transfer enhancement on micro/nanostructured surfaces’, Exp. Therm. Fluid Sci. **66**, 173–196 (2015).

[58] I. L. Pioro, W. Rohsenow, and S. S. Doerffer, ‘Nucleate pool-boiling heat transfer. I: review of parametric effects of boiling surface’, Int. J. Heat Mass Transfer **47**, 5033–5044 (2004).

[59] I. L. Pioro, W. Rohsenow, and S. S. Doerffer, ‘Nucleate pool-boiling heat transfer. II: assessment of prediction methods’, Int. J. Heat Mass Transfer **47**, 5045–5057 (2004).

[60] L. Dong, X. Quan, and P. Cheng, ‘An experimental investigation of enhanced pool boiling heat transfer from surfaces with micro/nano-structures’, Int. J. Heat Mass Transfer **71**, 189–196 (2014).

[61] Y. A. Çengel, ‘Pool Boiling’, in *Heat Transfer: A Practical Approach* (McGraw-Hill, Boston, 2003), pp. 518–530.

[62] M. Jakob and W. Linke, ‘Der Wärmeübergang von einer waagerechten Platte an siedendes Wasser’, Forsch. Ing.-Wes. **4**, 75–81 (1933).

[63] M. Jakob and W. Linke, ‘Der Wärmeübergang beim Verdampfen von Flüssigkeiten an senkrechten und waagerechten Flächen’, Phys. Z. **36**, 267–280 (1935).

[64] J. G. Leidenfrost, ‘De Fixitate Aquæ Diversa in Igne’, in *De Aquæ Communis Nonnullis Qualitatibus Tractatus* (Duisburgum ad Rhenum, 1756), pp. 30–63; [Int. J. Heat Mass Transfer **9**, 1153–1166 (1966)].

[65] I. Sher, R. Harari, R. Reshef, and E. Sher, ‘Film boiling collapse in solid spheres immersed in a sub-cooled liquid’, Applied Thermal Engineering **36**, 219–226 (2012).

[66] G. Baffou, J. Polleux, H. Rigneault, and S. Monneret, ‘Super-Heating and Micro-Bubble Generation around Plasmonic Nanoparticles under cw Illumination’, J. Phys. Chem. C **118**, 4890–4898 (2014).

[67] K. Setoura, S. Ito, and H. Miyasaka, ‘Stationary bubble formation and Marangoni convection induced by CW laser heating of a single gold nanoparticle’, **9**, 719–730 (2017).

[68] F. Li, S. R. Gonzalez-Avila, D. M. Nguyen, and C.-D. Ohl, ‘Oscillate boiling from microheaters’, Phys. Rev. Fluids **2**, 014007 (2017).

[69] K. Setoura, Y. Okada, and S. Hashimoto, ‘CW-laser-induced morphological changes of a single gold nanoparticle on glass: observation of surface evaporation’, Phys. Chem. Chem. Phys. **16**, 26938–26945 (2014).

[70] S. Hashimoto, T. Uwada, M. Hagiri, H. Takai, and T. Ueki, ‘Gold Nanoparticle-Assisted Laser Surface Modification of Borosilicate Glass Substrates’, J. Phys. Chem. C **113**, 20640–20647 (2009).

[71] W. Lauterborn and T. Kurz, ‘Physics of bubble oscillations’, Rep. Prog. Phys. **73**, 106501 (2010).

[72] *Pentane – Thermophysical Properties*, Engineering ToolBox, (2018) `https://www.engineeringtoolbox.com/pentane-properties-d_2048.html` (visited on 01/28/2019).

[73] V. Vesovic, *PENTANE*, Thermopedia, (Feb. 4, 2011) `http://www.thermopedia.com/content/1016/` (visited on 02/13/2019).

[74] M. Minnaert, ‘On musical air-bubbles and the sounds of running water’, London Edinburgh Dublin Philos. Mag. J. Sci. **16**, 235–248 (1933).

[75] K. F. MacDonald, V. A. Fedotov, S. Pochon, B. F. Soares, N. I. Zheludev, C. Guignard, A. Mihaescu, and P. Besnard, ‘Oscillating bubbles at the tips of optical fibers in liquid nitrogen’, Phys. Rev. E **68**, 027301 (2003).

[76] H. H. Funke, A. M. Argo, J. L. Falconer, and R. D. Noble, ‘Separations of Cyclic, Branched, and Linear Hydrocarbon Mixtures through Silicalite Membranes’, Ind. Eng. Chem. Res. **36**, 137–143 (1997).

[77] G. D. Fasman, *Circular dichroism and the conformational analysis of biomolecules* (Springer, New York, London, 2011).

[78] W. C. Johnson, ‘Secondary Structure of Proteins Through Circular Dichroism Spectroscopy’, Annu. Rev. Biophys. Biophys. Chem. **17**, 145–166 (1988).

[79] N. J. Greenfield, ‘Using circular dichroism spectra to estimate protein secondary structure’, Nat. Protoc. **1**, 2876 (2006).

[80] M. Hentschel, M. Schäferling, T. Weiss, N. Liu, and H. Giessen, ‘Three-Dimensional Chiral Plasmonic Oligomers’, Nano Lett. **12**, 2542–2547 (2012).

[81] Z. Wang, F. Cheng, T. Winsor, and Y. Liu, ‘Optical chiral metamaterials: a review of the fundamentals, fabrication methods and applications’, Nanotechnology **27**, 412001 (2016).

[82] M. Hentschel, M. Schäferling, X. Duan, H. Giessen, and N. Liu, ‘Chiral plasmonics’, Sci. Adv. **3**, e1602735 (2017).

[83] A. O. Govorov, ‘Plasmon-Induced Circular Dichroism of a Chiral Molecule in the Vicinity of Metal Nanocrystals. Application to Various Geometries’, J. Phys. Chem. C **115**, 7914–7923 (2011).

[84] B. M. Maoz, Y. Chaikin, A. B. Tesler, O. Bar Elli, Z. Fan, A. O. Govorov, and G. Markovich, 'Amplification of Chiroptical Activity of Chiral Biomolecules by Surface Plasmons', Nano Lett. **13**, 1203–1209 (2013).

[85] O. Arteaga, J. Sancho-Parramon, S. Nichols, B. M. Maoz, A. Canillas, S. Bosch, G. Markovich, and B. Kahr, 'Relation between 2D/3D chirality and the appearance of chiroptical effects in real nanostructures', Opt. Express **24**, 2242–2252 (2016).

[86] A. Papakostas, A. Potts, D. M. Bagnall, S. L. Prosvirnin, H. J. Coles, and N. I. Zheludev, 'Optical Manifestations of Planar Chirality', Phys. Rev. Lett. **90**, 107404 (2003).

[87] O. Arteaga, B. M. Maoz, S. Nichols, G. Markovich, and B. Kahr, 'Complete polarimetry on the asymmetric transmission through subwavelength hole arrays', Opt. Express **22**, 13719–13732 (2014).

[88] T. Bauer, 'Probe-based Nano-interferometric Reconstruction of Tightly Focused Vectorial Light Fields', PhD thesis (Friedrich-Alexander-Universität Erlangen-Nürnberg, Erlangen, 2017).

[89] L. Novotny and B. Hecht, *Principles of Nano-Optics*, Second Edition (Cambridge University Press, Cambridge, 2012).

[90] E. Jones, T. E. Oliphant, P. Peterson, et al., *SciPy: Open source scientific tools for Python.*

[91] R. Piessens, E. De Doncker-Kapenga, and C. W. Überhuber, *QUADPACK: a subroutine package for automatic integration* (Springer, 1983).

[92] M. Leutenegger, R. Rao, R. A. Leitgeb, and T. Lasser, 'Fast focus field calculations', Opt. Express **14**, 11277–11291 (2006).

[93] R. B. Wilson, B. A. Apgar, L. W. Martin, and D. G. Cahill, 'Thermoreflectance of metal transducers for optical pump-probe studies of thermal properties', Opt. Express **20**, 28829–28838 (2012).

[94] N. Taketoshi, T. Baba, and A. Ono, 'Observation of Heat Diffusion across Submicrometer Metal Thin Films Using a Picosecond Thermoreflectance Technique', Jpn. J. Appl. Phys. **38**, L1268 (1999).

[95] N. Taketoshi, T. Baba, and A. Ono, 'Development of a thermal diffusivity measurement system for metal thin films using a picosecond thermoreflectance technique', Meas. Sci. Technol. **12**, 2064 (2001).

[96] V. Juvé, M. Scardamaglia, P. Maioli, A. Crut, S. Merabia, L. Joly, N. Del Fatti, and F. Vallée, 'Cooling dynamics and thermal interface resistance of glass-embedded metal nanoparticles', Phys. Rev. B **80**, 195406 (2009).

[97] T. Stoll, P. Maioli, A. Crut, S. Rodal-Cedeira, I. Pastoriza-Santos, F. Vallée, and N. Del Fatti, 'Time-Resolved Investigations of the Cooling Dynamics of Metal Nanoparticles: Impact of Environment', J. Phys. Chem. C **119**, 12757–12764 (2015).

[98] J. Jandeleit, G. Urbasch, H. D. Hoffmann, H.-G. Treusch, and E. W. Kreutz, 'Picosecond laser ablation of thin copper films', Appl. Phys. A **63**, 117–121 (1996).

[99] A. Plech, V. Kotaidis, S. Grésillon, C. Dahmen, and G. von Plessen, 'Laser-induced heating and melting of gold nanoparticles studied by time-resolved x-ray scattering', Phys. Rev. B **70**, 195423 (2004).

[100] V. Kotaidis and A. Plech, 'Cavitation dynamics on the nanoscale', Appl. Phys. Lett. **87**, 213102 (2005).

[101] T. Katayama, K. Setoura, D. Werner, H. Miyasaka, and S. Hashimoto, 'Picosecond-to-Nanosecond Dynamics of Plasmonic Nanobubbles from Pump–Probe Spectral Measurements of Aqueous Colloidal Gold Nanoparticles', Langmuir **30**, 9504–9513 (2014).

[102] S. Inasawa, M. Sugiyama, and Y. Yamaguchi, 'Laser-Induced Shape Transformation of Gold Nanoparticles below the Melting Point: The Effect of Surface Melting', J. Phys. Chem. B **109**, 3104–3111 (2005).

[103] G. González-Rubio, A. Guerrero-Martínez, and L. M. Liz-Marzán, 'Reshaping, Fragmentation, and Assembly of Gold Nanoparticles Assisted by Pulse Lasers', Acc. Chem. Res. **49**, 678–686 (2016).

[104] S. Hashimoto, T. Uwada, M. Hagiri, and R. Shiraishi, 'Mechanistic Aspect of Surface Modification on Glass Substrates Assisted by Single Shot Pulsed Laser-Induced Fragmentation of Gold Nanoparticles', J. Phys. Chem. C **115**, 4986–4993 (2011).

[105] J. H. Hodak, I. Martini, and G. V. Hartland, 'Spectroscopy and Dynamics of Nanometer-Sized Noble Metal Particles', J. Phys. Chem. B **102**, 6958–6967 (1998).

[106] A. L. Tchebotareva, P. V. Ruijgrok, P. Zijlstra, and M. Orrit, ‘Probing the acoustic vibrations of single metal nanoparticles by ultrashort laser pulses’, Laser Photonics Rev. **4**, 581–597 (2010).

[107] P. V. Ruijgrok, P. Zijlstra, A. L. Tchebotareva, and M. Orrit, ‘Damping of Acoustic Vibrations of Single Gold Nanoparticles Optically Trapped in Water’, Nano Lett. **12**, 1063–1069 (2012).

[108] L. Hou, ‘Photothermal Studies of Single Molecules and Gold Nanoparticles: Vapor Nanobubbles and Conjugated Polymers’, PhD thesis (Universiteit Leiden, Leiden, 2016).

[109] A. H. Harvey, J. S. Gallagher, and J. M. H. L. Sengers, ‘Revised Formulation for the Refractive Index of Water and Steam as a Function of Wavelength, Temperature and Density’, J. Phys. Chem. Ref. Data **27**, 761–774 (1998).

[110] D. B. Leviton and B. J. Frey, ‘Temperature-dependent absolute refractive index measurements of synthetic fused silica’, in , edited by E. Atad-Ettedgui, J. Antebi, and D. Lemke (June 14, 2006), 62732K.

[111] W. S. Fann, R. Storz, H. W. K. Tom, and J. Bokor, ‘Electron thermalization in gold’, Phys. Rev. B **46**, 13592–13595 (1992).

[112] R. W. Schoenlein, W. Z. Lin, J. G. Fujimoto, and G. L. Eesley, ‘Femtosecond studies of nonequilibrium electronic processes in metals’, Phys. Rev. Lett. **58**, 1680–1683 (1987).

[113] H. E. Elsayed-Ali, T. Juhasz, G. O. Smith, and W. E. Bron, ‘Femtosecond thermoreflectivity and thermotransmissivity of polycrystalline and single-crystalline gold films’, Phys. Rev. B **43**, 4488–4491 (1991).

[114] C.-K. Sun, F. Vallée, L. H. Acioli, E. P. Ippen, and J. G. Fujimoto, ‘Femtosecond-tunable measurement of electron thermalization in gold’, Phys. Rev. B **50**, 15337–15348 (1994).

[115] E. Carpene, ‘Ultrafast laser irradiation of metals: Beyond the two-temperature model’, Phys. Rev. B **74**, 024301 (2006).

[116] T. Labouret and B. Palpant, ‘Nonthermal model for ultrafast laser-induced plasma generation around a plasmonic nanorod’, Phys. Rev. B **94**, 245426 (2016).

[117] S. Link and M. A. El-Sayed, ‘Spectral Properties and Relaxation Dynamics of Surface Plasmon Electronic Oscillations in Gold and Silver Nanodots and Nanorods’, J. Phys. Chem. B **103**, 8410–8426 (1999).

[118] Y. R. Shen, ‘Distinction between resonance Raman scattering and hot luminescence’, Phys. Rev. B **9**, 622–626 (1974).

[119] Y.-Y. Cai, E. Sung, R. Zhang, L. J. Tauzin, J. G. Liu, B. Ostovar, Y. Zhang, W.-S. Chang, P. Nordlander, and S. Link, ‘Anti-Stokes Emission from Hot Carriers in Gold Nanorods’, Nano Lett. **19**, 1067–1073 (2019).

[120] K. T. Crampton, A. Fast, E. O. Potma, and V. A. Apkarian, ‘Junction Plasmon Driven Population Inversion of Molecular Vibrations: A Picosecond Surface-Enhanced Raman Spectroscopy Study’, Nano Lett. **18**, 5791–5796 (2018).

[121] A. Carattino, M. Caldarola, and M. Orrit, ‘Gold Nanoparticles as Absolute Nanothermometers’, Nano Lett. **18**, 874–880 (2018).

[122] M. Yorulmaz, S. Khatua, P. Zijlstra, A. Gaiduk, and M. Orrit, ‘Luminescence Quantum Yield of Single Gold Nanorods’, Nano Lett. **12**, 4385–4391 (2012).

[123] P. G. Etchegoin, E. C. Le Ru, and M. Meyer, ‘An analytic model for the optical properties of gold’, J. Chem. Phys. **125**, 164705 (2006).

[124] Y. He, K. Xia, G. Lu, H. Shen, Y. Cheng, Y.-c. Liu, K. Shi, Y.-F. Xiao, and Q. Gong, ‘Surface enhanced anti-Stokes one-photon luminescence from single gold nanorods’, Nanoscale **7**, 577–582 (2014).

[125] Y. Sivan and S.-W. Chu, ‘Nonlinear plasmonics at high temperatures’, Nanophotonics **6**, 317–328 (2017).

[126] I. Gurwich and Y. Sivan, ‘Metal nanospheres under intense continuous-wave illumination: A unique case of nonperturbative nonlinear nanophotonics’, Phys. Rev. E **96**, 012212 (2017).